

2015

Carbon and water cycles in mixed-forest catchments: ecohydrological modeling of the influence of climate variability and invasive insect infestation

<https://hdl.handle.net/2144/14042>

Downloaded from DSpace Repository, DSpace Institution's institutional repository

BOSTON UNIVERSITY
GRADUATE SCHOOL OF ARTS AND SCIENCES

Dissertation

**CARBON AND WATER CYCLES IN MIXED-FOREST CATCHMENTS:
ECOHYDROLOGICAL MODELING OF THE INFLUENCE OF
CLIMATE VARIABILITY AND INVASIVE INSECT INFESTATION**

by

JIHYUN KIM

B.S., Kyung Hee University, Republic of Korea, 2007
M.A., Boston University, 2010

Submitted in partial fulfillment of the
requirements for the degree of
Doctor of Philosophy

2015

Approved by

First Reader

Crystal L. Schaaf, Ph.D.
Adjunct Research Professor of Earth and Environment

Second Reader

Alan H. Strahler, Ph.D.
Professor of Earth and Environment

Third Reader

Taehee Hwang, Ph.D.
Assistant Professor of Geography
Indiana University Bloomington

DEDICATION

I would like to dedicate this work to my family and friends on the other side of the Earth

ACKNOWLEDGMENTS

I would like to express my sincere gratitude to my advisor, Dr. Crystal L. Schaaf, for her support and guidance throughout my research work. I deeply appreciate the tremendous time and sincere efforts she made discussing my projects and advising me. I would also like to thank Dr. Alan H. Strahler, who has always inspired me with his sincere attitude toward the science. Their passion and genuine ideas have invigorated me into enjoying my research. It would not have been possible to accomplish my scientific goals without their guidance.

Special thanks go to my committee members Dr. Ellen Douglas, Dr. Lucy Hutyra, and Dr. Taehee Hwang for their insightful comments, advices, and time which have stimulated and improved my work.

Last but not least, I would like to thank my family, for spending so much time and energy in supporting and encouraging me. I would not have been made to this point without them.

**CARBON AND WATER CYCLES IN MIXED-FOREST CATCHMENTS:
ECOHYDROLOGICAL MODELING OF THE INFLUENCE OF
CLIMATE VARIABILITY AND INVASIVE INSECT INFESTATION**

(Order No.)

JIHYUN KIM

Boston University Graduate School of Arts & Sciences, 2015

Major Professor: Crystal L. Schaaf, Adjunct Research Professor

ABSTRACT

Temperate mixed forests are complex ecosystems composed of multiple vegetation types with very different physiological characteristics which are distributed over the landscape. This dissertation investigates the influence of these mixed plant landscapes on eddy-covariance flux data, and in particular, uses an ecohydrological model to study the influence of climate variability and insect infestation on a mixed forest at the Harvard Forest Long Term Ecological Research site in Massachusetts.

There are significant seasonal and interannual variabilities in the extent and the orientation of the footprints of a flux tower (EMS-tower) at the Harvard Forest. The Gross Primary Productivity (GPP) flux was found to be largely dependent on the vegetation density during the green-up and senescence periods, but not during the mature period. Half of the interannual anomalies in the mature period GPP flux can be explained by the variation in the proportion of coniferous evergreen needleleaf forest (ENF) in the footprint. Every 1% decrease of ENF resulted in the increase of the GPP flux by 20 gC m^{-2} .

2.

The spatially-distributed process-based Regional Hydro-Ecological Simulation System (RHESSys) model was implemented in two headwater catchments at the Harvard Forest to simulate water and carbon cycles from 1992 to 2008. Results were evaluated using field measurements such as streamflow and the GPP and evapotranspiration (ET) fluxes at two flux towers. The simulated annual GPP flux of the deciduous forest showed strong and significant long-term increases, six times higher than the GPP flux of the coniferous forest, while the increase in ET flux of both forests was small yet significant.

The Harvard Forest was infested by Hemlock Woolly Adelgid (HWA) between 2004 and 2008, and although there has not yet been a significant increase in the total annual mortality, the small stature stands have started to die off by 5.7%. The HWA infestation has already resulted in an increased streamflow in the catchment dominated by hemlock stands (44% in area). In 2014, the increased annual streamflow was estimated as 81 mm using the RHESSys model with an embedded representation of the HWA-induced loss of water conductivity (calibrated using the Hemlock tower ET flux).

TABLE OF CONTENTS

DEDICATION	iv
ACKNOWLEDGMENTS	v
ABSTRACT	vi
TABLE OF CONTENTS.....	viii
LIST OF TABLES	xii
LIST OF FIGURES	xiii
Chapter 1. Introduction	1
1.1. Background	1
1.2. Regional Hydro-Ecological Simulation System (RHESSys) overview.....	3
1.3. Dissertation overview	5
Chapter 2. Assessing seasonal changes in spatial heterogeneity of a mixed forest and the impact of interannual variations in the footprint land cover composition on flux measurements.....	8
2.1. Introduction.....	8
2.2. Methodology	13
2.2.1. Study site.....	13
2.2.2. Data overview	13
2.2.3. Flux tower footprint delineation	16
2.2.4. Spatial representative evaluation I – Semivariogram analysis.....	20

2.2.5. Spatial representative evaluation II – Window size analysis	22
2.3. Result	24
2.3.1. Seasonal and interannual variations in flux tower footprints.....	24
2.3.2. Spatial heterogeneity in the regional ecosystem scale	28
2.3.3. Spatial variation around the flux tower.....	31
2.3.4. Correlation between EVI and tower GPP	33
2.3.5. Variations in the land cover proportions.....	35
2.3.6. Impacts of land cover composition on the flux measurement	39
2.4. Discussion and conclusion.....	42
 Chapter 3. Long-term carbon and water cycles in mixed forest catchments: ecohydrological modeling from patch-scale to catchment-scale	
3.1. Introduction.....	45
3.2. Model Overview - Summary of key processes	48
Farquhar photosynthesis model	48
Modified Penman-Monteith evapotranspiration model	49
Jarvis stomata conductance model.....	50
Vegetation dynamics.....	51
Vertical hydrologic processes	51
Lateral redistribution.....	52
3.3. Materials and Methods.....	53
3.3.1. Study site overview.....	53
3.3.2. Data overview	56

4.3.3. Catchment-level streamflow response	128
4.4. Discussion and conclusion.....	134
Chapter 5. Conclusion.....	137
5.1. Dissertation overview	138
5.2. Future Research	142
BIBLIOGRAPHY.....	144
CURRICULUM VITAE.....	166

LIST OF TABLES

Table 2.1. Linear regression results between GPP anomalies in each period (δGPP) and land cover proportion anomalies ($\delta\text{P}_{\text{LC}}$): correlation coefficients (slope, β_1) and coefficient of determination (r^2).....	40
Table 3.1. List of ground-measurements used in this study	60
Table 3.2. Parameterization of soil components.....	65
Table 3.3. Ecophysiological parameterization in the model.....	66
Table 3.4. List of parameters calibrated with GLUE method, their initial values and calibrating factor ranges.....	68
Table 3.5. Long-term trends in annual fluxes from 1992 to 2008 at patch scales and catchment scales.....	92
Table 4.1. Stand vigor index mean and standard deviation (within parenthesis) of each DBH class as well as overall class in 1999, 2009, and 2014.....	122
Table 4.2. Population (N) and average annual mortality rates of eastern hemlock and all species.....	123

LIST OF FIGURES

- Figure 2.1. The number of flux towers for each land cover type (<http://fluxnet.ornl.gov/>).
..... 9
- Figure 2.2. (a) Top-of-the-atmosphere (TOA) surface reflectance composites (Landsat TM/ETM+ Band 4-3-2) retrieved during green-up (4/25/2008), mature (8/31/2008) and senescence (10/11/2008) within 1.0 km and 1.5 km fields centered over the Harvard Forest EMS-tower. (b) EVI on the same date with (a). (c) Semivariogram estimators calculated with EVI values in each period (points), the fitted isotropic spherical variogram models (solid curves), and *ranges* (dash vertical lines). (d) Orthography was presented as a reference scene at a very-high resolution (30 cm) that was created by the USGS (MassGIS: <http://www.mass.gov/>)..... 23
- Figure 2.3. Wind rose of daytime (10:00-19:00) horizontal wind at Harvard Forest from 1992 to 2008: distribution and frequency of speed and direction (a) during growing season (April-October) for the entire study period (1992-2008 on the left side) and four examples of individual years (on the right side) (b) for each period: green-up, mature, and senescence during the study period (1992-2008 on the left side) and four examples of individual years (on the right side)..... 26
- Figure 2.4. EVI maps of the study site (1.0 km field only) centered over the EMS-tower (red cross) from 1992 to 2008 in senescence period (first column), in green-up period (second and third column), and mature period (fourth column). Dates were selected in neither ascending nor descending order because of the limited

availability of Landsat TM/ETM+ scenes. The contours represent ϕ_{80} in each period in the year, and points represent $\phi_{80,peak}$ location..... 27

Figure 2.5. Footprint areas ($A_{\phi_{80}}$) from 1992 to 2008 in each period (green-up period in open orange circle, mature period in solid red circle, senescence period in open blue square, and growing season in open black triangle) and boxplot (first quartile-the median-the third quartile) 28

Figure 2.6. (a) Semivariogram parameters, *nugget effect* and *sill*, of EVI in 1.0 km and 1.5 km fields respectively. Years are presented in different colors and sizes. (b) The *sill* values of 1.0 km field from 1992 to 2008 (c) TOA surface reflectance composites (Landsat TM/ETM+ Band 4-3-2) in 1999, 2000, 2001, and 2008 show the gradual changes in the land cover over the study site (e.g. a woody swamp on the NW side of the tower due to beaver activity and the development of the Bigelow swamp on the SE side)..... 30

Figure 2.7. Semivariogram parameter, *range*, of EVI in 1.0 km and 1.5 km fields respectively. Years are presented in different colors and sizes (same setup in Fig 1.6). Horizontal black bar is the radius of the circle having the median footprint area in the period ($A_{\phi_{80}\pi}$)..... 31

Figure 2.8. The window-averaged EVI value (EVI on the top row), and variations of the EVI relative to the EVI1km (Δ EVI on the bottom row) of all the available EVI data between 1992 and 2008 in (a) green-up, (b) mature, and (c) senescence periods. Vertical colored bar is the window widths having the footprint areas in the period ($A_{\phi_{80}}$)..... 33

Figure 2.9. Scatterplot and linear regression fit between the tower-derived daily GPP from 1992 to 2008 and (a) the averaged EVI of 1.0 km field (EVI_{1km}), (b) the averaged EVI within 80% cumulative footprint function without weighting footprint density (EVI ϕ ₈₀-unweighted), and (c) the averaged EVI within 80% cumulative footprint function with weighting footprint density for the period (EVI ϕ ₈₀-weighted) 34

Figure 2.10. Seasonal footprints (ϕ ₈₀) from 1999 to 2008 on the land cover maps centered over the EMS-tower (red cross). NLCD 2001 is assigned for the years from 1999 to 2003, and NLCD 2006 for the years from 2004 to 2008 (1.0 km field only). The contours represent ϕ ₈₀ in each period in the year, and points represent ϕ ₈₀, peak location..... 37

Figure 2.11. The land cover proportion (a) within 1.0 km and 1.5 km fields centered over the EMS tower calculated from NLCD 2001, and 2006 maps. Land cover proportion within footprints estimated by unweighting the footprint density (ϕ ₈₀*PLC bars on the left-side in each year) and by weighting footprint density (ϕ ₈₀*PLC bars on the right-side in each year) during (b) green-up period, (c) mature period, (d) senescence period, and (e) growing season. Differences between two methods ($\Delta P_{LC} = \phi$ ₈₀*PLC - ϕ ₈₀*PLC) are presented only for the four major land cover types (ENF, DBF, MF, and woody wetlands)..... 38

Figure 2.12. Scatterplots and linear regression fits between the tower-derived daily GPP anomalies (δ GPP) and the selected land cover proportion anomalies (δ P_{LC}) in each period 41

Figure 3.1. Two study catchments on the Harvard Forest Prospect Hill. (a) Catchment boundaries (red lines) and stream networks (cyan lines) for Bigelow-Brook catchment (BBC) and Nelson-Brook catchment (NBC) delineated by Bigelow lower pipe and Nelson big weir (black and white divided circles). This study mainly incorporated; meteorological data from Fisher and Shaler weather stations (diamonds), and water and carbon flux from HEM and EMS towers (triangles). Canopy-level results are from the area in black and yellow squares, for HEM-tower and for EMS-tower respectively (b) Vegetation was reclassified from 2001 National Land Cover Dataset (NLCD). (c) Soil distribution, generated by aggregating soil classes in the USDA National Resources Conservation Service (NRCS) soil survey database..... 55

Figure 3.2. Estimation of soil decomposition-rate scaling. (Top panel) Dots indicate the field-measured soil efflux (gray squares: all available soil temperature and efflux data, red diamonds: data only within the towers' footprint). The green dash line is the RHESSys default function (with coefficients $a=71.02$, $b=227.13$) and the orange solid line is the modified function using the fitted coefficients ($a=48.14$, $b=234.51$). (Bottom panel) Residual plots of the default function (green squares) and modified function (yellow triangles)..... 63

Figure 3.3. (a) Monthly precipitation. (b) Calibration and validation results with monthly streamflow discharge at BBC and NBC. Gray area indicates 95% confidence intervals estimated from GLUE method with the likelihood measure log-NSE. Black diamonds are the mean value of the confidence interval and circles are monthly-total

streamflow discharge. Dash lines are the observed streamflow at BBC (green) and NBC (orange)..... 71

Figure 3.4. Scatter plots between observed and simulated streamflow at monthly, and annual scales at BBC (green) and NBC (orange) for (a) calibration and (b) validation periods. Monthly scatter plots evaluated streamflow during growing-season (May and October) when soil moisture modulates vegetation responses to the climate.... 72

Figure 3.5. The time series of observed and simulated soil moisture values in the study sites. (a) Gray area indicates 95% confidence intervals of the soil moisture at the EMS-patch (top) and HEM-patch (bottom), respectively. Dots are the areal mean value of the observations within the footprints. Bar indicates standard deviation of the observations (b) Soil moisture of EMS-tower from 1996 to 2000 with the monthly and annual precipitation..... 74

Figure 3.6. Soil respiration. Gray areas indicate 95% confidence intervals at the EMS-patch (left-top) and HEM-patch (left-bottom). Red diamonds are the areal mean values of the observations within the footprints. Bar indicates standard deviation of the observations. Scatter plot of model versus observation at EMS-patch (right-top) and HEM-patch (right-bottom)..... 76

Figure 3.7. LAI simulation (Left-top) Gray area indicates 95% confidence intervals at the EMS-patch and HEM-patch (Left-bottom). Dots are the areal mean value of the observations within the footprints. Bar indicates standard deviation of the observations. (Right-top) Scatter plot between observed and simulated LAI at EMS-patch..... 78

Figure 3.8. Distribution of number of days of the observed GPP during spring-time, summer-time, and fall-time in 1992, 2000, and 2008..... 79

Figure 3.9. GPP simulation at EMS-patch (a) Daily scale temporal plot. Gray area indicates 95% confidence intervals. Dots are GPP at EMS-tower. Vertical lines are the prescribed phenological timings (growing-up, maturity, senescence, and dormancy) (b) Monthly scale temporal plot. Black diamond represents mean of the 95% confidence interval, and red circle indicates monthly-total GPP at EMS-tower. 81

Figure 3.10. GPP simulation scatter plots of model versus observation (a) during the entire study period at daily and monthly scales (b) during the subdivided periods with the least square regression line in solid red 82

Figure 3.11. GPP simulation at HEM-patch. (left) Daily scale temporal plot. Gray area indicates 95% confidence intervals. Dots are GPP at HEM-tower (right) scatter plot of model versus observation daily scale with the least square regression line in solid red. 83

Figure 3.12. ET simulation at EMS-patch (a) Daily scale temporal plot. Gray area indicates 95% confidence intervals. Dots are water vapor flux measured at EMS-tower. Vertical lines are the prescribed phenological timings (growing-up, maturity, senescence, and dormancy) Scatter plots of model versus observation with the least square regression line in solid red (b) during the entire study period (c) during the subdivided periods 85

Figure 3.13. Distribution of number of days of the simulated ET during spring-time, summer-time, and fall-time in 1992, 2000, and 2008..... 86

Figure 3.14. ET simulation at HEM-patch (left) Daily scale temporal plot. Gray area indicates 95% confidence intervals. Dots are water vapor flux measured at HEM-tower. (right) scatter plot of model versus observation daily scale with the least square regression line in solid red..... 86

Figure 3.15. Scatter plot and regression analysis of (a) observed annual GPP at EMS-tower versus simulated annual GPP at EMS-patch..... 89

Figure 3.16. Annual flux and long-term trends in annual GPP, ET and basal area increment at (top) EMS-patch and (bottom) HEM-patch. Black dots are the means of 95% confidence intervals (gray area) of simulated GPP, red circles are annual GPP at EMS-tower. Brown squares are basal area increments. Light-blue bars are simulated ET. Vertical lines are 95% confidence intervals of ET. Solid lines are the regression lines estimated using Spearman Rho’s test (slopes, correlation coefficients, and significances are summarized in Table 3.5) 89

Figure 3.17. Scatter plots and regression analysis of the observed precipitation in the water years versus the sum of simulated ET and streamflow in BBC (green dots and lines) and in NBC (orange dots and lines)..... 91

Figure 3.18. Long-term trends of catchment-scale GPP and ET at (a) BBC and (b) NBC. Black dots are the means of 95% confidence intervals (gray area) of simulated GPP. Light-blue bars are simulated ET, and streamflow is expressed in green bars (BBC) and orange bars (NBC). Vertical lines are 95% confidence intervals of simulated

streamflow and ET. Solid lines are the regression line estimated using Spearman Rho's test (slopes, correlation coefficients, and significances are summarized in Table 3.5)	91
Figure 3.19. Annual GPP and ET from 1992 to 2008 at EMS-patch and HEM-patch.....	95
Figure 3.20. Scatter plot and regression analysis of observed annual precipitation versus simulated annual ET at both patches and catchments. Spatial scales (patches and catchments) are distinguished by color, and fluxes by symbol.	95
Figure 3.21. Scatter plots and regression analysis of annual GPP compared to annual ET at EMS-patch (colored circle) and HEM patch (colored triangle). Each year is colored in unique color.	96
Figure A3.1. Schematic diagram of estimating phenological transitional timings. Spring and autumn phenological indices (green circle and brown diamond) using the ground-based visual observations in 2008 (hf003-03, hf003-04). The black thick line is the fitted logistic phenology model (Eq. A3.1). The solutions of the forth derivative of the fitted model (thin black line on the top) are the phenological transitional timings (Eq. A3.4) expressed as vertical dash lines (t_G, t_M, t_S, t_D).	100
Figure A3.2. Schematic diagram of estimating phenological transitional timings from 1992 to 2008. Setup is the same as Fig A2.1. Spring and autumn phenological indices (green circle and brown diamond) using the ground-based visual observations (hf003-03, hf003-04). The black line is the fitted logistic phenology model (Eq. A3.1), and the phenological transitional timings (Eq. A3.4) expressed as vertical dash lines (t_G, t_M, t_S, t_D).	101

Figure A3.3. Temporal plot of phenological timings from 1992 to 2008.....	102
Figure 4.1. Summertime-mean ET_{day} (square symbol), mean square error (MSE, colored circles) and the survival functions with the Weibull probability distribution, $fLC(t)$ in Eq. 4.2. Y-axes for MSE and ET_{day} are on left side, and Y-axes of the $fLC(t)$ in 2005 and 2008 are on the right side, having same color with the MSE circle and the $fLC(t)$ accordingly.	118
Figure 4.2. Absence/presence of HWA in 2009 and 2014. o/o indicates both branches were not infested; o/+ indicates one branch was infested and the other branch was not infested; ++ indicates two branches were infested.	121
Figure 4.3. Stand vigor index mean (square) and standard deviation (vertical bar) of each DBH class (indicated by the colors) and overall class (black-filled square)	122
Figure 4.4. Population histogram (left) and average annual mortality rates plot (right) of eastern hemlock (bottom) and all species (top). Numbers are summarized in Table 4.2.....	124
Figure 4.5. Field estimates (black squares with vertical bar of standard deviation) and model simulates (red boundary is 95% confidence interval of loss of conductivity (LC)-scenario and blue boundary is 95% confidence interval of the scenario without having LC) of (a) LAI, (b) ET (model simulates is monthly flux, field estimates is daytime hourly, and (c) simulated annual total transpiration (T, positive-direction bar), evaporation (E. negative-direction bar), and evapotranspiration (ET, square dots) with LC (red color) and without having LC (blue color).....	127

Figure 4.6. Fisher’s LSD test on the observed summertime ET_{day} from 2005 to 2013.

Vertical dotted lines are 95% confidence interval of ET_{day} in 2009 (blue bar). ET_{day} in 2012 and 2013 (red bars) was significantly different from 2009. 128

Figure 4.7. Hydrograph (a) monthly total precipitation from 2008 to 2014 (b) monthly

total observed streamflow (black solid-line) and model simulates (red boundary is 95% confidence interval of loss of conductivity (LC)-scenario and blue boundary is 95% confidence interval of the scenario without having LC) (c) residual plots of the simulated streamflow (observed streamflow minus simulated streamflow). Squares are the mean residual of the 95% confidence interval and the vertical bars are the ranges of residuals of the 95% confidence interval. Gray bars (ΔLC) are the changes in the simulated annual streamflow by HWA-induced LC ($fLC(t; t_0 = 2008)$ in Eq.4.2)..... 131

Figure 4.8. Scatter plots for the paired-catchment approach. (a) Gray-filled circles are the

monthly streamflow during calibration period (2008-2011) and LC period (2012-2014). Each year in LC period was plotted in different colored symbol: 2012 in green rectangle, 2013 in blue triangle, and 2014 in red circle (b) HWA-induced annual streamflow change in QBB (ΔQBB) in vegetation years in colored bars with the confidence interval vertical bars. Black bars are annual precipitation in the vegetation year. 133

Chapter 1. Introduction

1.1. Background

Terrestrial ecosystems exchange energy, carbon, water, and nutrients with the atmosphere through both biotic processes and indirect abiotic processes that are controlled by the biotic processes. For example, approximately 120 Gt of carbon are circulated every year between terrestrial ecosystems and the atmosphere through photosynthesis and respiration processes (Urbanski et al., 2007). Thus small variations in the balance between photosynthesis and respiration control both interannual and seasonal variabilities in atmospheric carbon dioxide concentration (CO₂, Hartmann et al., 2013), one of the major greenhouse gases. The largest terrestrial water flux is the transpiration from ecosystems, which is approximately $62,000 \pm 8,000$ km³ of water per year (Eakins & Sharman, 2010; Jasechko et al., 2013). Nitrogen in the soil returns to the atmosphere through the denitrification process that is heavily controlled by soil moisture (Kulkarni et al., 2014), which, in turn, is significantly driven by plant water uptake.

Furthermore, it is critical to fully understand how the terrestrial ecosystems have responded to the past external forces such as climate changes and invasive insect infestations in order to predict energy, carbon, water, and nutrient cycles in the future. The National Climate Assessment (Walsh et al., 2014) has recorded the significant climate changes occurring over the recent past, including an approximate 1.3°F increase in the U.S. average temperature since 1980 (the most recent decade was the nation's warmest on record), and roughly a 5% increase in precipitation (primarily in the form of

heavy rainfall events) since 1900. Atmospheric CO₂ concentrations at the Hawaii Mauna Loa Observatory have just surpassed 400 parts per million (ppm) for the first time in human history (as of July 2015). These were only 317 ppm in 1958 when Charles D. Keeling began these atmospheric CO₂ measurements (NOAA, 2015).

Over the past two decades, there have been remarkable progress in expanding our understanding of terrestrial ecosystems at a wide range of spatial and temporal scales: plot-scale discrete-time ground-based sampling and forest inventories (Bechtold, Patterson, & Editors, 2005; Field et al., 1982; Lindroth & Cienciala, 1995), canopy-scale continuous eddy covariance flux measurements (Baldocchi, 2003), and regional and global-scale semi-continuous remote sensing techniques (Kerr & Ostrovsky, 2003; Zhao & Running, 2010). Each method has its own distinct advantages and inevitable drawbacks. Using data from these methods, there have been a large number of studies reporting ecosystem responses to recent climate change, such as phenological shifts (Keenan et al., 2014; Menzel et al., 2006), changes in ecosystem production and respiration rates (Nemani et al., 2003; Richardson et al., 2007; Schimel et al., 2001), and transitions in species distribution and diversity (Kelly et al., 2008; Walther et al., 2005).

Ecosystem models provide the tools to aggregate these observations into different spatio-temporal scales, to quantitatively represent our understanding of current ecosystem processes, and to predict the plausible responses of these ecosystems to different climate projections in the future. For example, an ecosystem model that has a canopy-scale (or stand-scale) spatial modeling unit, a so called “*spatially-distributed model*”, can be applied to upscale the eddy-flux measurements from a single location to the regional

landscape scale of remote sensing data. This is especially critical in those highly heterogeneous regions that are composed of multiple different plant types (such as mixed forests that serve as the focus of this study). An ecosystem model that describes the processes based on the mathematical representations of the process responses to external environments, a so called “*process-based model*”, can explore the impact of certain external factors on the entire ecosystem functions (e.g. temperature, precipitation, and atmospheric CO₂ level).

For this research we will initialize a spatially-distributed process-based Regional Hydro-Ecological Simulation System (RHESSys) model with field-observations and remote-sensing data to produce statistically optimized estimates of fluxes from a temperate mixed forest ecosystem and improve our understanding of the system processes. We will be applying the RHESSys model to two mixed forest catchments at the Harvard Experimental Forest in Central Massachusetts, USA. This location has been systematically monitored since 1988 and a wide range of regional experiments are being conducted there to understand the processes of the biogeochemical cycles. We will incorporate both in-situ measurements and remotely sensed parameters in the model to investigate the dynamics of carbon and water cycles of these New England mixed forest sites that are experiencing both climate change and the impacts of an insect infestation.

1.2. Regional Hydro-Ecological Simulation System (RHESSys) overview

RHESSys (Band et al., 2000; Band et al., 1993; Tague & Band, 2004) is a physical process-based model, which integrates hydrologic processes, biogeochemical cycling and

microclimate variability using the algorithms modified from the several existing models: TOPMODEL (Beven & Kirkby, 1979), BIOME-BGC (Running & Hunt Jr., 1993), and MT-CLIM (Running et al., 1987). The Geographic Information System (GIS)-based model framework of RHESSys allows it to directly import remote sensing data to describe the spatial information such as land cover, soil type, leaf area index (LAI), and topography as digital elevation model (DEM).

The spatial information is partitioned into a nested series of functional objects or patches with which hydrological, microclimate, and ecological processes are associated. Dynamic coupling between hydrologic response and vegetation and land cover dynamics is implemented with this differential representation of vertical and lateral processes at different temporal scales. RHESSys can account for lateral connection between patches (smallest spatial scale of vegetation), allowing the spatial connectivity to vary with changes in drainage organization or hydrologic flow paths as a result of the construction of road drainage and storm drain networks in urbanized watersheds (Tague & Pohl-Costello, 2008). RHESSys has been developed using the object-based approach, with C programming, to facilitate the modification of model structures and process algorithm.

RHESSys has been applied to a number of ecohydrological watersheds with diverse climate parameters; including varying watershed scale transpiration and production (Band et al., 1991; Band et al., 1993; Nemani et al., 1993; Mackay et al., 2003; Zierl et al., 2007), nitrogen processes (Band et al., 2001; Creed et al., 1996; Groffman et al., 2009; Tague, 2009), spatial patterns of vegetation growth (Mackay & Band, 1997; Mackay, 2001), spatial patterns of vegetation species (Meentemeyer et al., 2001; Meentemeyer & Moody, 2002), hydrologic responses to climate change (Band et al., 1996; Baron et al., 2000; Christensen et al., 2008; Tague et al., 2009; Jefferson et al., 2008), and streamflow prediction of ungauged watersheds (Tague &

Pohl-Costello, 2008). This dissertation represents the first time RHESys has been applied to a New England mixed forest with its wide range of annual dynamics and climatic variations and one furthermore which is also experiencing an insect infestation by the Hemlock Woody Adelgid, *Adelges tsugae* Annand.

1.3. Dissertation overview

Three related studies are conducted to address the dynamics in carbon and water cycling in this New England mixed forest experiencing both long-term gradual climate changes and an invasive insect outbreak.

In chapter two, we focus on use of flux tower information to both parameterize and evaluate our model results. We investigate the spatial representativeness of single tower flux measurements and assess the ability of those data to capture the variability of the regional landscape. The Environmental Measurement Site (EMS) flux tower at Harvard Experimental Forest is located in a north-eastern mixed forest with a landscape that is primarily driven by the phenology of the deciduous stands intermixed with a heterogeneous distribution of evergreen coniferous stands. The area that contributes to the flux observed by a tower, the so-called “*footprint*”, should vary depending on the atmospheric stability, wind speed, and the wind direction. At the Harvard Forest, this can be critical considering that the tower location is surrounded by woody wetlands on the northeast and swamps on the southeast during the study period (1992-2008). We use a footprint climatology to estimate seventeen years of seasonal footprints at the flux tower. We calculate vegetation density using fine-resolution (30 m) Landsat TM/ETM+ imagery

to examine the vegetation density distribution within the tower footprint in each season. We also investigate the correlation between the flux anomalies and the vegetation type proportions within the footprints. Furthermore, we explore whether the seasonal flux tower measurements adequately represent the vegetation characteristics at the larger spatial scales (1.0 km and 1.5 km scales) of the MODerate resolution Imaging Spectroradiometer (MODIS) and Visible Infrared Imaging Radiometer Suite (VIIRS), as MODIS provides the most widely used remote sensing data for dynamic ecosystem studies that is extended by VIIRS.

In chapter three, we focus on optimizing the spatially-distributed process-based ecohydrological model RHESSys for the region. Since the model is based on a water mass balance concept, incoming water flux (precipitation) should be balanced by the outgoing water flux (streamflow and evapotranspiration). The model is implemented for two small headwater catchments in the Harvard Forest. The simulated estimates of carbon and water cycling are validated at different scales using a number of field measurements: plot-scale soil respiration and moisture as well as ground-based measurements of leaf area index (LAI), canopy-scale gross primary productivity (GPP) and evapotranspiration (ET) information using the flux data from two eddy flux towers in the forest, and catchment-scale streamflow values using local gauge data. We compare the different responses of the deciduous and coniferous plant types, both of which have been experiencing identical climate changes over the past seventeen years.

In chapter four, we analyze the impact of an invasive insect infestation, the hemlock woolly adelgid (HWA), on the streamflow of the study catchments using both

streamflow data and the RHESSys model. The HWA, which causes extensive mortality in eastern hemlock (*Tsuga canadensis*) was first reported in Virginia in 1951 and first arrived at Harvard Forest between 2005 and 2008. Eastern hemlocks heavily control the water cycle in this region where they represent a local community, yet not many studies have analyzed the impact of HWA infestation on the streamflow explicitly (Brantley et al., 2013). It is important to fully understand the hydrologic ramifications of eastern hemlock mortality as this region also serves as the reservoir for drinking water for the city of Boston and it is therefore important to be able to accurately predict future fresh water availability. We first investigate the development process of the HWA infestation state, the hemlock stands condition, and the mortality of hemlocks from 2009 to 2014. We estimate the hydraulic limitation caused by the HWA infestation using a simplified representation, incorporate it into RHESSys model, and evaluate the simulated estimates using field measurements. Based on the analysis using simulated streamflow estimates as well as the actual streamflow data, the change in the streamflow caused by the HWA infestation is assessed.

Taken as a whole, this dissertation demonstrates that our understanding of the dynamics in mixed forests can be significantly improved by integrating geospatial analysis, and field measurements, with a spatially distributed ecosystem modeling framework.

Chapter 2. Assessing seasonal changes in spatial heterogeneity of a mixed forest and the impact of interannual variations in the footprint land cover composition on flux measurements

2.1. Introduction

There has been a remarkable increase in the number of studies reporting ecosystem responses to recent climate change such as phenological shifts (Keenan et al., 2014; Menzel et al., 2006), changes in ecosystem production and respiration rates (Nemani et al., 2003; Richardson et al., 2007; Schimel et al., 2001), and transitions in species distribution and diversity (Kelly & Goulden, 2008; Walther et al., 2005). Numerous methods have been proposed and applied to define, quantify, and monitor ecosystem behaviors and changes at different temporal and spatial scales as well as to understand the underlying biophysical processes and their feedbacks: point-scale ground samplings (Field et al., 1982; Lindroth & Cienciala, 1995), canopy-scale eddy-covariance flux measurements (Baldocchi, 2003), regional and global-scale remote-sensing techniques (Zhao & Running, 2010), and multiscale computational ecosystem models (Cao & Woodward, 1998; Cramer et al., 2001). Flux towers using the eddy-covariance technique have been rapidly increasing globally, with over 650 sites (as of April 2014. <http://fluxnet.ornl.gov/>), providing a unique and important role as “quasi-truth observations”. The flux measurements have been used in a wide-range of studies such as intercomparison of multiple biomes (Keenan et al., 2013), calibration and/or validation of terrestrial ecosystem models as well as remote sensing-based estimates (Heinsch et al.,

2006; Schwalm et al., 2010), and correlations between the two or three ecosystem processes by incorporating ground-measured biophysical attributes (Davidson et al., 2006). Mixed forests and croplands are the most common land cover types on which flux towers have been established (Figure 2.1). A number of flux towers with the longest flux records are also located in mixed forests, for example Harvard Forest (US-Ha1, since 1991), Howland Forest (US-Ho1,2,3, since 1995,1999,2001), ON-Borden Mixedwood (CA-Cbo, since 1995), Takayama (JP-Tak, since 1993), Brasschaat (BE-Bra, since 1996), Changbaishan (CN-Cha, since 2002), and more.

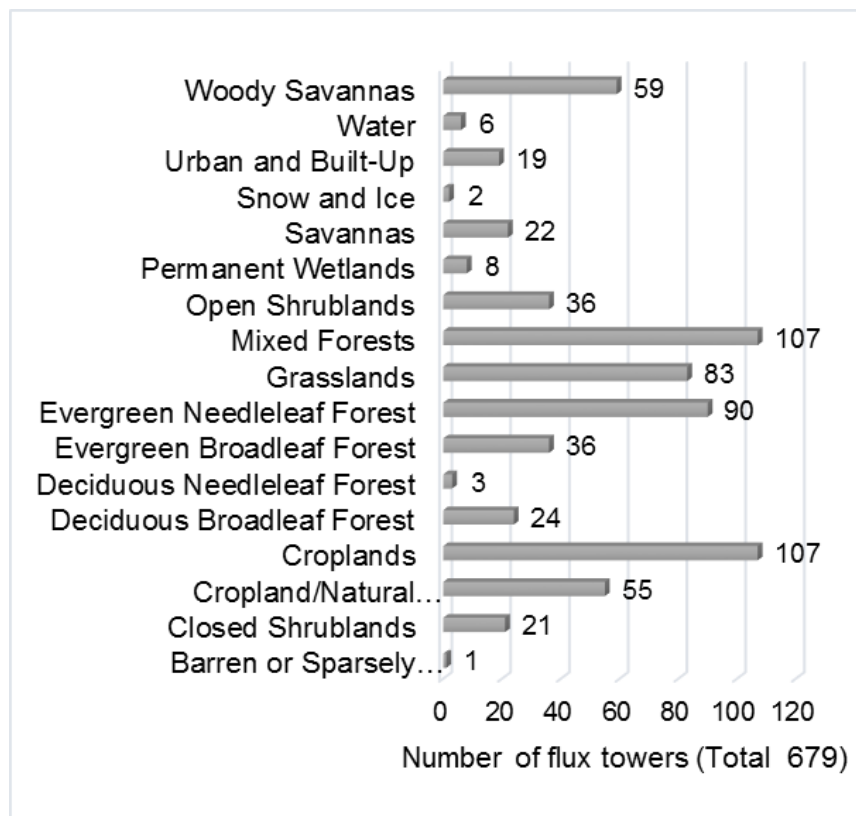


Figure 2.1. The number of flux towers for each land cover type (<http://fluxnet.ornl.gov/>).

Depending on the wind direction, topographic variation, stand species, and their distribution in the landscape surrounding a flux tower in a mixed forest, the upwind

surface contributing to the measured flux at the flux tower (so-called “*footprint*”) could either adequately represent the characteristics of the regional ecosystem, or not. This inevitable reality has long been recognized as one of the primary uncertainties in flux measurements (Baldocchi, 2003). To reduce this uncertainty, there are growing efforts to develop flux footprint models (Kljun et al., 2002; Schmid, 1994; van Ulden, 1978) and apply the footprint extents and densities in the ground-sampling scheme or in the analysis of measurements (Amiro, 1998; Chasmer et al., 2011; Stoy et al., 2006). For example, one recent study has shown that horizontal and vertical advection fluxes resulting from complex and heterogeneous topographic variations within the flux footprint are critical to appropriately analyze the energy balance closure and carbon flux measured at the tower (Novick et al., 2014). However, as of yet, most of studies have not removed flux data measured at times when the wind was not blowing from the region of interest from their datasets. Such filtering is required as this effect can sometimes leave only 25% of the total data appropriate for upwind analysis (Hadley & Schedlbauer, 2002; Stoy et al., 2006).

In reality, the spatial representativeness of a flux tower footprint for the regional ecosystem is typically assessed only once for a study. This is mostly due to the limited availability of high resolution satellite scenes, and an assumption that the representativeness at any given moment during the study period will be constant and steady throughout a year without any long-term change in the landscape (Kim et al., 2006). However, the spatial representativeness of a flux tower footprint located in a mixed forest should be expected to have significant intraannual (seasonal) as well as

interannual variations depending on the species composition of the landscape. The recursive phenological cycle of deciduous stands (leaf emergence, maturity, senescence, and dormancy) is the first and foremost factor changing the entire landscape of a mixed forest. Román et al. (2009) demonstrated that the representativeness of a tower albedometer footprint (note: an albedometer has a fixed footprint area) in a deciduous broadleaf forest or in a mixed forest at the spatial scales of the Moderate Resolution Imaging Spectroradiometer (MODIS) and Visible Infrared Imaging Radiometer Suite (VIIRS) (i.e. resolution of 1.0 km, 1.5 km, and 2.0 km) is largely dependent on the leaf development stages (leaf-on or leaf-off). The study also showed that the timing of leaf emergence on deciduous stands and the distribution of conifer stands in a mixed forest drove the spatial variation over the landscape, determining whether the tower-measured albedo was sufficiently representative to be appropriate for the validation of the MODIS derived surface albedo retrieved. The intrinsic physiological differences between species also contribute to spatial variations in the biophysical attributes of the landscape. Tian et al. (2002) described that the spatial variation in Leaf Area Index (LAI) within a 15×13 km field in a mixed forest is mostly governed by the difference across plant types, 76% of total variance. The different sensitivities of vegetation species to interannual climate anomalies (Welp et al., 2007) and the gradual changes in the stand species and distribution resulted from the climate change (Battles et al., 2007) are all present in mixed forests, driving seasonal, interannual, and long-term changes in the spatial variability of the landscape characteristics. Thus, the spatial representativeness of a flux tower in a mixed forest should be thoroughly evaluated and considered in the process of interpreting

the flux measurement as well as in the procedure of calibrating and validating biophysical parameters in regional and global scale ecosystem models and from remote sensing data with flux measurements.

In this study, we (1) estimated the seasonal footprints of a flux tower during study period, from 1992 to 2008 with a footprint climatology. The tower is located in the mixed forest so that the landscape is primarily driven by the development stages of leaves in the deciduous stands in relation to the evergreen coniferous stands which are not uniformly distributed over the forest. Furthermore we (2) examined whether vegetation density variation within the tower footprint in each season could adequately represent the vegetation density characteristics at the spatial scales of moderate resolution remote sensing data (1.0 km and 1.5 km) through semivariogram and window-size analyses using fine-resolution remote sensing datasets. Finally we (3) investigated the impact of the interannual variations in the land cover composition within the footprints on the seasonal flux measurements from 1999 to 2008.

2.2. Methodology

2.2.1. Study site

The study site is the area surrounding the Environmental Measurement Site (EMS) tower (42.537755°N, 72.171478°W; Fluxnet Site Code:US-Ha1) at Harvard Forest in Petersham, Massachusetts. The study site is composed of deciduous broadleaf forests and evergreen needleleaf forests under a cool and moist temperate climate. An annual mean temperature is 8.5 °C (20 °C in July, and 7 °C in January) and mean annual precipitation is approximately 1100mm. The forest is mainly dominated by northern red oak (*Quercus rubra*), red maple (*Acer rubrum*), eastern hemlock (*Tsuga canadensis*), white pine (*Pinus strobes*), and black birch (*Betula lenta*) (Urbanski et al., 2007). Topography is moderate with elevation ranging from 250m to 430m above sea level.

Beginning from 1993, on-ground transects have been established along the southwest (SW) and northwest (NW) directions which that are the prevailing wind directions (Urbanski et al., 2007). A number of ground-based biometric measurements (i.e. soil temperature and respiration, leaf area index, green foliage and leaf litter chemistry) have been collected on these transects (Barford et al., 2001; Munger & Wofsy, 1999; Savage & Davidson, 2001a).

2.2.2. Data overview

Meteorological data measured at the EMS-tower, such as friction velocity (u^*), wind direction (α) and air temperature, were used in this study (Harvard Forest dataset ID:

HF004-01; Munger & Wofsy, 1999b). Gap-filled hourly sensible heat flux measurement and gross ecosystem exchange (GEE) estimates were provided from the Harvard Forest LTER data archive (Harvard Forest dataset ID: HF004-02; Munger & Wofsy, 1999b). Assuming dark-respiration and the flux from the understory canopy are ignorable, GEE were converted to the gross primary productivity. Note that GEE is the estimates from the net ecosystem exchange (NEE) measurement and ecosystem respiration, adjusted from night-time NEE measurement as a function of the air and soil temperature (Falge et al., 2001). Data recorded with friction velocity (u^*) below 0.3 m s^{-1} was removed from further analysis to filter out the advection of the understory canopy, and only daytime (10:00-19:00) measurements were considered in this study.

Cloud-free Landsat Thematic Mapper (TM) and Enhanced Thematic Mapper Plus (ETM+) scenes from 1992 to 2008 were collected (<http://earthexplorer.usgs.gov/>), and surface reflectance data at the spatial resolution of 30 m was retrieved using the Landsat Ecosystem Disturbance Adaptive Processing System (LEDAPS; <http://ledapsweb.nascom.nasa.gov/>, Masek et al., 2006). Landsat TM/ETM+ does not provide as high resolution scenes as sensors such as IKONOS (1 m in pan-chromatic mode; 4 m in multi-spectral mode), and it does not provide any routine information on the vertical structure of the field vegetation as would an airborne or terrestrial Lidar (Chasmer et al., 2011). However, its long-term historical archive of observations, TM on Landsat 4 and 5 from 1982 to 2012, and ETM+ on Landsat7 since 1999, and the Operational Land Imager (OLI) on Landsat8 since 2013, allows us to perform efficient, consistent, and continuous assessments of land surface heterogeneities.

We selected the enhanced vegetation index (EVI, Eq. 2.1) as the indicator of vegetation distribution and density instead of the well-known and widely-used normalized difference vegetation index (NDVI) because NDVI becomes asymptotically saturated in the high biomass area whereas EVI still exhibits sensitivities to the variations in the vegetation structures (Huete et al., 2002).

$$EVI = G \frac{\rho_{nir} - \rho_{red}}{\rho_{nir} + C_1 \cdot \rho_{red} - C_2 \cdot \rho_{blue} + L} \quad (2.1)$$

where ρ is the top-of-atmosphere surface reflectance in near-infrared, red, and blue bands (ρ_{nir} , ρ_{red} , and ρ_{blue}), and C_1 and C_2 are the aerosol resistance coefficients, and G is gain factor, and L is the canopy background adjustment. The coefficients are set as follows: $L=1$, $C_1=6$, $C_2=7.5$, and $G=2.5$ (Huete et al., 2002).

The land cover information was based on two National Land Cover Dataset products (NLCD 2001 and NLCD 2006; available at <http://www.mrlc.gov/>). The NLCD 2001 and 2006 products have a spatial resolution of 30 meter with overall accuracies (Level II: 16 classes) of 79% and 78%, respectively (Wickham et al., 2010; Wickham et al., 2013). Since there are differences in the land cover class definitions between NLCD1992 and NLCD 2001-2006, the NLCD1992 was not used in this study. Due to the limited availability of the NLCD products, we analyzed only ten years of variations in the land cover composition within the footprint, from 1999 to 2008, and NLCD 2001 was utilized to represent land covers between 1999 and 2003, while NLCD 2006 was used for the years between 2004 and 2008.

In this study, “periods” were defined as follows: the “green-up period” indicates dates from April 1 to May 31, the “mature period” is from June 1 to August 31, and the “senescence period” is from September 1 to October 31. The term “growing season” will imply the dates from April 1 to October 31.

2.2.3. Flux tower footprint delineation

We generated crosswind-integrated (along-wind) footprint functions, $f^y(x, z_m)$ in Eq. (2.2), of all periods and growing seasons from 1992 to 2008 with the parameterized version of a simplified Lagrangian stochastic footprint model (Kljun et al., 2004; available online at <http://footprint.kljun.net/varinput.php>) under the approximated atmospheric stability conditions ($-100 < z_m/L < 1$). The sensor height parameter (z_m) was set to the instrument height (sonic anemometer is at 29 m height) minus the displacement height ($d = 2/3$ times the canopy height; Chasmer *et al.*, 2011), where canopy height was set to a constant, 21 m, in this study (Goulden et al., 1996). The Monin-Obukhov length (L) was calculated with the measured u^* , air temperature and heat flux (Gryning *et al.*, 1987).

$$f^y(x, z_m) = \frac{F_*(x, z_0)}{z_m} \cdot \left(\frac{\sigma_w}{u_*}\right)^{-\alpha_2} \cdot \left(1 - \frac{z_m}{h}\right) \quad (2.2)$$

F_* is a non-dimensional form of the crosswind-integrated footprint function and α_2 is a free parameter, parameterized in Kljun *et al.* (2004). The surface roughness length (z_0) is about 1.6 m for both deciduous and coniferous canopies (Hadley et al., 2002; Wu et al., 2015). The standard deviation of the vertical wind velocity (σ_w) and planetary boundary

layer (h) were approximated from Gryning *et al.* (1987) depending on the atmospheric stability. It should be noted that the simplified Lagrangian stochastic footprint model assumes that the upwind domain is spatially homogeneous; therefore it could neither fully consider the boundary layer turbulence between land cover types nor take into account topographic variation in ground surface. However, the parameterized model still provides practical approximates of the footprints, consuming less computational cost and time, which is important in the analysis of hourly data for seventeen years. Since the Kljun *et al.* (2004) parameterization provides only crosswind-integrated (along-wind) footprint function, $f^y(x, z_m)$, lateral crosswind dispersion was combined to the $f^y(x, z_m)$ to estimate crosswind-dispersed footprint function, $f(x, y, z_m)$, assuming along-wind and cross-wind components are independent (Detto et al., 2006).

$$f(x, y, z_m) = f^y(x, z_m) \cdot D_y(x, y) \quad (2.3)$$

where $D_y(x, y)$ is the lateral crosswind dispersion assuming a Gaussian distribution (Pasquill, 1974),

$$D_y(x, y) = \frac{1}{\sigma_y \sqrt{2\pi}} \cdot \exp\left(-\frac{y^2}{2\sigma_y^2}\right) \quad (2.4)$$

where the standard deviation of y-location (σ_y) is estimated from the standard deviation of the crosswind velocity σ_v (Eckman, 1994).

$$\sigma_y = a \cdot z_0 \left(\frac{\sigma_v}{u_*}\right) \left(\frac{x}{z_0}\right)^p \quad (2.5)$$

where a and p are the coefficients depending on the atmospheric stability that are set to 0.31 for a and 0.86 for p respectively in this study (Eckman, 1994). The standard

deviation of the crosswind velocity (σ_v) was estimated from the friction velocity (u^*) depending on the atmospheric stability (Gryning et al., 1987). Hourly $f(x, y, z_m)$ was then rotated toward the wind direction (α) as Eq. (2.6) to calculate the directional crosswind-dispersed footprint function, $f(x', y', z_m)$.

$$\begin{bmatrix} x' \\ y' \end{bmatrix} = \begin{bmatrix} \cos\theta & -\sin\theta \\ \sin\theta & \cos\theta \end{bmatrix} \begin{bmatrix} x \\ y \end{bmatrix} \quad (2.6)$$

where the rotation angle $\theta = 360 - \alpha$. The rotation angle starts at $y = 0$ and goes counter-clockwise, while wind-direction starts at $x=0$ and goes clockwise.

The footprint density (φ) at an individual point (x', y') in a study period was calculated as the cumulative sum of all hourly $f(x', y', z_m)$ in the period that are normalized by dividing the integral value of the $f(x', y', z_m)$ of the entire source domain in the period (Eq. 2.6) (B. Chen et al., 2013).

$$\varphi(x', y', z_m) = \frac{\sum_{i=1}^{N_w} f_i(x', y', z_m)}{\iint_{-\infty}^{\infty} \sum_{i=1}^{N_w} f_i(x', y', z_m) dx' dy'} \quad (2.7)$$

where N_w is the number of measurement in the period. The integral of φ over the source domain in the period is, therefore, equal to one. The boundary of the 80th percentile of the φ was delineated as the “*footprint*” (φ_{80}) because the $f^y(x, z_m)$ becomes significantly flattened at 90th percentile, reducing the performance of the parameterization as well as overextending the footprints area (Chasmer et al., 2011; Kljun et al., 2004).

The relative proportion of each land cover type contributing to the measured CO₂ flux in a period ($P_{LC,k}$, Eq. 2.8) was calculated in two ways following Chen *et al.*, (2013) (1) by superimposing the φ_{80} on the land cover maps ($\varphi_{80} * P_{LC}$), and (2) by treating all

contribution within the footprint domain equally ($\varphi_{80}=1$, hereafter $\overline{\varphi_{80}}$), that is, only considering the area ($\overline{\varphi_{80}} * P_{LC}$). In this study, land cover type (k) followed NLCD level-2 classification scheme; deciduous broadleaf forest (DBF), evergreen needleleaf forest (ENF), mixed forest (MF), woody wetland, low residential, and cultivated crop. As mentioned above, due to the absence of higher resolution land cover data available on an annual basis, the footprint functions from 1999 to 2003 were associated with the NLCD 2001, and the footprint functions from 2004 to 2008 were associated with the NLCD 2006.

$$\varphi_{80} * P_{LC,k} = \frac{\sum_{i=1}^{N_p} \chi_{k,i} \cdot \varphi_{80}}{\sum_{k=1}^{N_{LC}} \left(\sum_{i=1}^{N_p} \chi_{k,i} \cdot \varphi_{80} \right)} \quad (2.8)$$

where $\chi_{k,i}$ is the indicator function of the land cover type of the i -pixel as

$$\chi_{k,i} = \begin{cases} 1 & \text{if } i - \text{pixel land cover} = k \\ 0 & \text{if } i - \text{pixel land cover} \neq k \end{cases} \quad (2.9)$$

where N_p and N_{LC} refer the total number of pixels and the number of the land cover types within the footprint domain, respectively. The $\overline{\varphi_{80}} * P_{LC}$ was also calculated with Eq. (2.8) with $\overline{\varphi_{80}}$ instead of φ_{80} .

We investigated whether the tower-derived GPP would correlate with P_{LC} . Year-to-year anomalies in the P_{LC} (δP_{LC} , Eq. 2.13) were calculated for each period with several land cover indicators (each individual vegetation type, the sum of DBF and ENF, and the total forest proportion) and with and without the weighting footprint density function.

$$\delta P_{LC,k}(m, n) = P_{LC,k}(m, n) - \overline{P_{LC,k}}(n) \quad (2.10)$$

where $P_{LC,k}(m, n)$ is the proportion of k -type land cover in m -year n -period ($m = 1999$ -2008, $n =$ green-up, mature, and senescence periods and growing season). $\overline{P_{LC,k}}(n)$ is the mean proportion of k -type land cover in n -period from 1999 to 2008 ($\overline{P_{LC,k}}(n) = \sum_{m=1999}^{2008} P_{LC,k}(m, n) / (2008 - 1999)$). Year-to year anomalies in GPP from the mean GPP for each period (δGPP) were calculated in the same way ($\delta GPP(m, n) = (m, n) - \overline{GPP}(n)$; $m = 1999$ -2008). Correlation analysis was performed using a simple linear regression to quantify the degree to which δGPP in each period can be explained with each δP_{LC} indicator.

2.2.4. Spatial representative evaluation I – Semivariogram analysis

The semivariogram model (Carroll & Cressie, 1996; Curran, 1988) has been recognized as one of the most efficient tools to describe spatial variation and autocorrelation in the sample measurements, and widely applied to numerous geostatistical studies ranging from abiotic phenomena (e.g. temperature and precipitation; Haylock et al. 2008) to biophysical attributes (e.g. surface vegetation albedo; Román et al. 2009). We quantified spatial variation within the field of MODIS GPP products (MOD17 and MYD17; 1.0 km) with the omnidirectional semivariogram model using all the available Landsat-retrieved EVI from 1992 to 2008 (Román et al., 2009; Susaki et al., 2007). We also examined spatial variation in 1.5 km as well because the spatial grid of the MODIS GPP product does not have its center exactly at the EMS-tower location. Three Landsat TM/ETM+ scenes in green-up, mature, and senescence periods in 2008 are shown in Figure (2.2a) along with the EVI (Figure 2.2b) and a very-high resolution (30

cm) photo-orthography image taken in green-up period a year after (2009) in Figure (2.2d).

The semivariance is defined as the average of the half variances of $N(h)$ pairs of observations at an interval distance (lag distance) of h (Curran, 1988). The semivariance estimator, $\bar{\gamma}_{EVI}(h)$, was calculated as half the average-squared-difference between EVI values at a pair of pixels separated by a distance h .

$$\bar{\gamma}_{EVI}(h) = \frac{\sum_i^{N(h)} \gamma_i(h)}{N(h)} = \frac{\sum_i^{N(h)} (Z_{xi} - Z_{xi+h})^2}{2N(h)} \quad (2.11)$$

where Z_{xi} is the EVI value at a pixel (x_i), and Z_{xi+h} is the EVI value at another pixel (x_{i+h}) within a lag distance h that is multiples of 30 m, the nominal resolution of TM/ETM+. Therefore the maximum lag distance for 1.0 km field would be 690 m, half of the length of the diagonal of 1.0 km boundary. The isotropic spherical variogram model (Eq 1.11, Matheron 1963) was fitted to the semivariance estimators to systematically obtain variogram parameters: *nugget effect* (c_0), *sill* (c), and *range* (a) in Figure (2.2c).

$$\gamma_{SPH}(h) = \begin{cases} c_0 + c \left(1.5 \left(\frac{h}{a} \right) - 0.5 \left(\frac{h}{a} \right)^3 \right), & 0 \leq h < a \\ c_0 + c & , h \geq a \end{cases} \quad (2.12)$$

The *nugget effect* is an estimation of the variance at a lag distance of zero, indicating microscale variability within the smallest sampling distance, errors in the measurements, or combination of both factors (Noréus et al., 1997). The *sill* is the horizontal asymptote of the variogram, reflecting absolute magnitude of heterogeneity within the region (1.0 km and 1.5 km in this study). The *range* is the lag distance at

which the variogram reaches the *sill*, beyond which there is no further spatial covariance between biophysical properties, and therefore is spatially uncorrelated. It can be also treated as the average size of heterogeneous attributes in the properties. Therefore when tower footprint extents reach beyond the *range*, they can be considered as a representative values for the entire study field (Kim et al., 2006).

2.2.5. Spatial representative evaluation II – Window size analysis

While semivariogram analysis only provides spatial variation of the entire study field not the adjacent landscape around the tower, spatial heterogeneity surrounding the tower was assessed with a window size analysis (B. Chen et al., 2012; Kim et al., 2006). The vegetation index, EVI in this study, within a window having the tower at its center was averaged (\overline{EVI}), increasing the width of the window horizontally and vertically (rectangle window). Variation in the window-averaged EVI (ΔEVI_i , Eq. 2.12) as the window width increases was calculated relative to the reference value, the 1.0 km field-averaged EVI (\overline{EVI}_{1km})

$$\Delta EVI_i = \overline{EVI}_i - \overline{EVI}_{1km} \quad (2.13)$$

while the width of window (i) increases by the multiples of 30 m, the nominal resolution of Landsat TM/ETM+: $i = 30, 90, \dots, 990$ m (width of \overline{EVI}_{1km}), \dots , 1500 m.

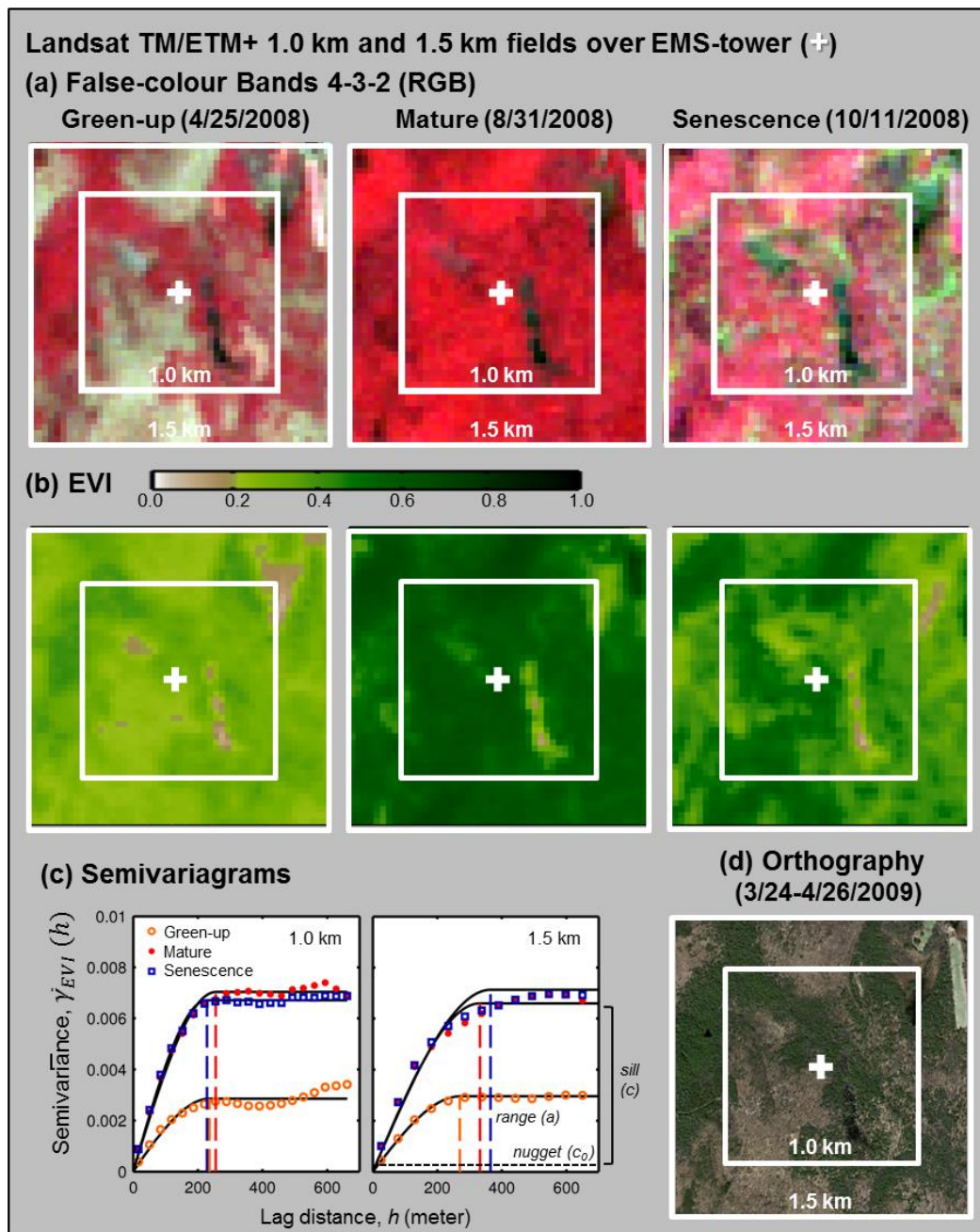


Figure 2.2. (a) Top-of-the-atmosphere (TOA) surface reflectance composites (Landsat TM/ETM+ Band 4-3-2) retrieved during green-up (4/25/2008), mature (8/31/2008) and senescence (10/11/2008) within 1.0 km and 1.5 km fields centered over the Harvard Forest EMS-tower. (b) EVI on the same date with (a). (c) Semivariogram estimators calculated with EVI values in each period (points), the fitted isotropic spherical variogram models (solid curves), and *ranges* (dash vertical lines). (d) Orthography was presented as a reference scene at a very-high resolution (30 cm) that was created by the USGS (MassGIS: <http://www.mass.gov/>)

2.3. Result

2.3.1. Seasonal and interannual variations in flux tower footprints

In the Harvard Forest, prevailing wind directions during the study period (from 1992 to 2008) were from the SW and the NW (Figure 2.3a-on the left side). Year-to-year prevailing wind direction, however, sometimes varied dramatically from these predominantly SW-NW directions, as well as the frequency of wind speed in each of the wind directions (examples in Figure 2.3a-on the right side). Strong winds are most frequent in spring (during the green-up period) from the north-northwest (NNW), but sometimes occur in autumn (during the senescence period) from the east or the west (Figure 2.3b).

As expected, footprints were largely dependent on the wind directions. The estimated footprints (φ_{80}) overlaid on the year-to-year EVI are presented in Figure (2.4). Distribution of the footprint density can be quantitatively analyzed with the location of the density peak point ($\varphi_{80,peak}$). The green-up period density peak points were mostly on the west side of the tower between 1992 and 2008 ($\mu_{\varphi_{80,peak}}=275^\circ$), but largely dispersed from SW to NW ($\sigma_{\varphi_{80,peak}}=63^\circ$), sometimes even on the east side (88°) in 2003. Density peak points of the mature and growing seasons were mostly on the south-southwest side of the tower ($\mu_{\varphi_{80,peak}}=211^\circ, 214^\circ$, respectively) with little dispersion ($\sigma_{\varphi_{80,peak}}=19^\circ, 25^\circ$, respectively). The senescence period had the most density peak points on the west-southwest side ($\mu_{\varphi_{80,peak}}=256^\circ$) dispersed from south-southwest to west-northwest ($\sigma_{\varphi_{80,peak}}=47^\circ$). The extent of φ_{80} was mostly about 300 m and up to 370

m from the tower, which is about half the length of the HEM-tower footprints (Hadley et al., 2002). The average area of the footprints ($A\phi_{80}$) was about 0.23 km^2 ($\sigma = 0.017 \text{ km}^2$), ranging from 0.16 km^2 in 1998 senescence period to 0.26 km^2 in 2003 growing season (Figure 2.5). In general, footprints tended to be larger (extended) in size during the green-up period due to the strong NW and E winds, and smaller (focused) during the mature period. However, there was neither significant seasonal pattern nor noticeable long-term trends in the variations in the footprint size.

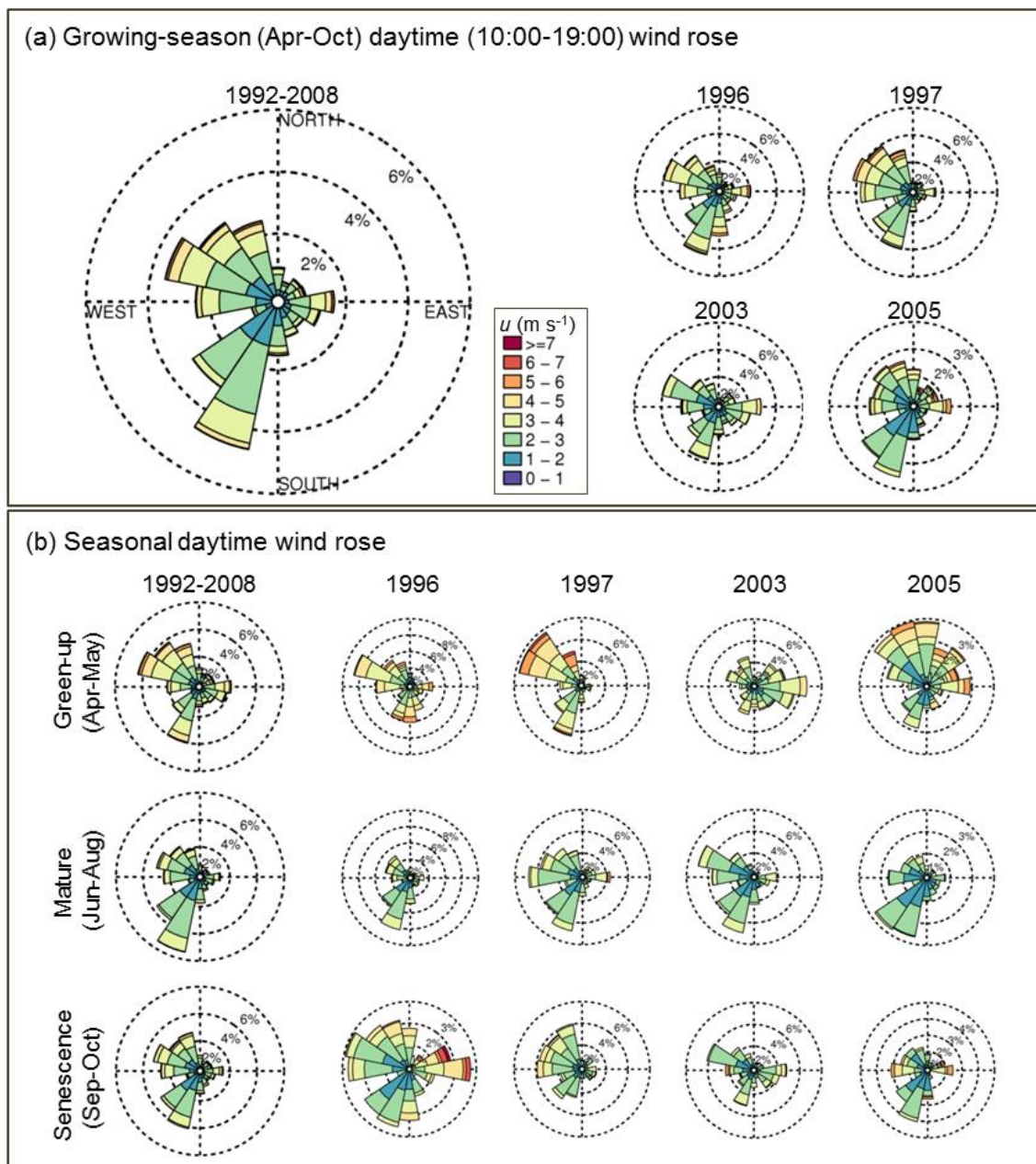


Figure 2.3. Wind rose of daytime (10:00-19:00) horizontal wind at Harvard Forest from 1992 to 2008: distribution and frequency of speed and direction (a) during growing season (April-October) for the entire study period (1992-2008 on the left side) and four examples of individual years (on the right side) (b) for each period: green-up, mature, and senescence during the study period (1992-2008 on the left side) and four examples of individual years (on the right side)

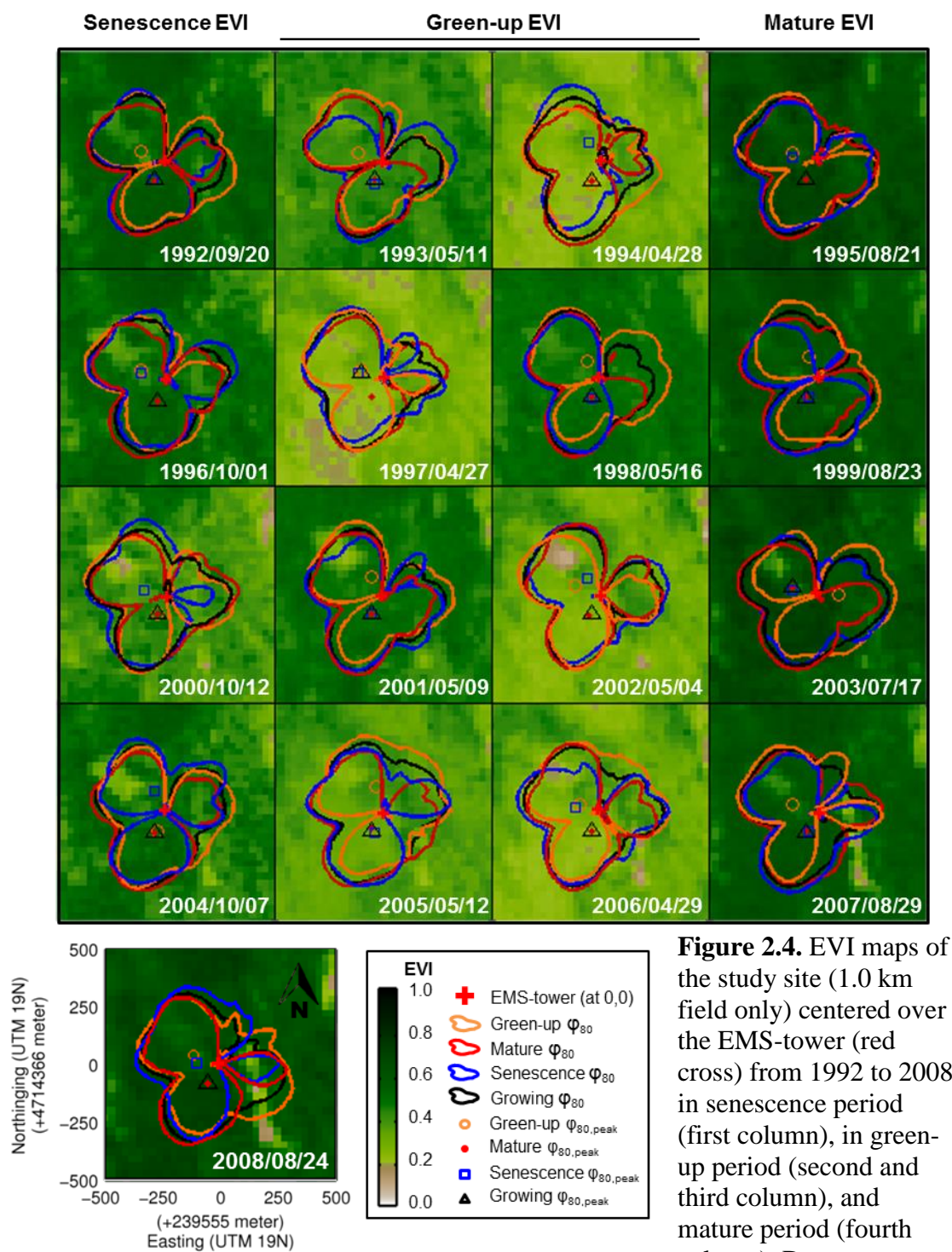


Figure 2.4. EVI maps of the study site (1.0 km field only) centered over the EMS-tower (red cross) from 1992 to 2008 in senescence period (first column), in green-up period (second and third column), and mature period (fourth column). Dates were

selected in neither ascending nor descending order because of the limited availability of Landsat TM/ETM+ scenes. The contours represent ϕ_{80} in each period in the year, and points represent $\phi_{80,peak}$ location.

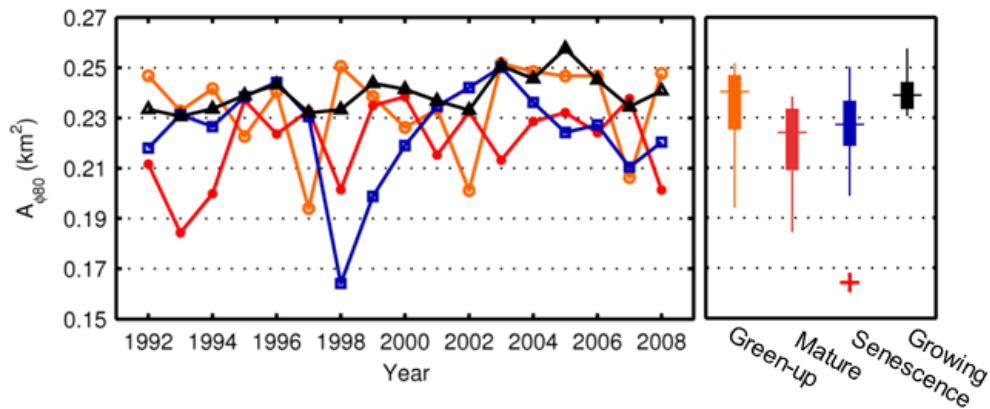


Figure 2.5. Footprint areas ($A_{\phi 80}$) from 1992 to 2008 in each period (green-up period in open orange circle, mature period in solid red circle, senescence period in open blue square, and growing season in open black triangle) and boxplot (first quartile-the median-the third quartile)

2.3.2. Spatial heterogeneity in the regional ecosystem scale

In the study area, the *nugget effect* values showed that there was a strong seasonality in the spatial variations at the sub-pixel scale (Figure 2.6a). The *nugget effect* values of 1.0 km field were high during dormancy (about 0.001), and they gradually decreased during green-up period. There was almost no sub-pixel scale variance during growing-season because the forest canopy within each pixel was completely closed, and it started to increase until the end of senescence. Since our interest is the spatial structure and variation in growing-season, the *nugget effect* values near zero in the period indicate that the sampling interval (i.e. 30 m in this study) is appropriate to resolve the spatial sources of variation in this study. The pasture area and woody wetlands that are located at the NE corner of 1.5 km field caused high *nugget effect* during the mature period. The *sill*

values of both 1.0 km and 1.5 km fields exhibited comparable magnitudes and profiles (Figure 2.6a). There were high spatial variations about 0.005 at the beginning of the green-up period before the phenological cycle of deciduous stands in the fields started. Spatial variations decreased until the beginning of the mature period. Although we expected that the study field would become most homogeneous (low spatial variations) in mature period once the deciduous stands were fully developed and the canopy around the tower was closed (Lévesque et al., 1999), the result showed that the spatial variations in both fields were increased during the early mature period, as the forest canopy was becoming closed, and it remained relatively constant at the high magnitude by the end of the senescence period. In mid-September of 1999, beaver activity caused a flood on the NW side of the tower, developing a small woody wetland (Savage et al., 2001; Urbanski et al., 2007). The *sill* values started to increase in 2001 due to the development of this wetland, remained at a similar magnitude, and then started to increase again because of the development of the Bigelow swamp on the SE side of the tower (Figure 2.7c).

The 1.0 km field had fairly constant *range* values during the whole growing season without any noticeable seasonality, an average *range* of 250 m during green-up period, 230 m during mature period, and 240 m during senescence period (Figure 2.7). Most of the *range* values were smaller than the radius of the circle which has a median footprint area in each period ($\sqrt{A_{\varphi 80}/\pi} = 276$ m, 267 m, and 269 m in green-up, mature, and senescence period, respectively). This implies that footprints were sufficiently expanded to represent the spatial variation of the EVI in the 1.0 km field (Kim et al., 2006). The 1.5 km field had smaller *range* values than the 1.0 km field during dormancy,

and higher *range* values during growing-season due to the clear cut areas on the NE outer corner of 1.0 km field, as already seen in *nugget effect* value.

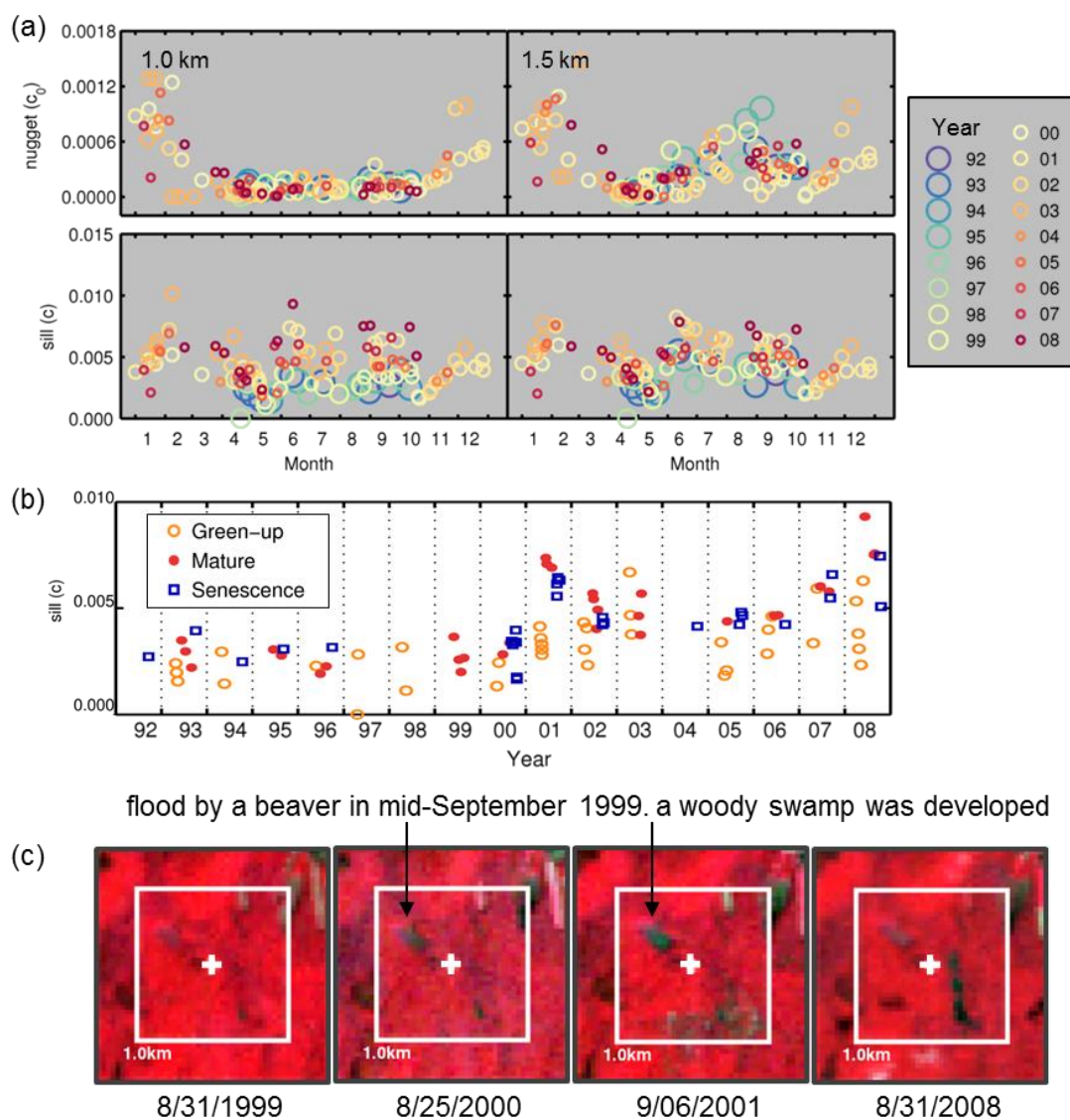


Figure 2.6. (a) Semivariogram parameters, *nugget effect* and *sill*, of EVI in 1.0 km and 1.5 km fields respectively. Years were presented in different colors and sizes. (b) The *sill* values of 1.0 km field from 1992 to 2008 (c) TOA surface reflectance composites (Landsat TM/ETM+ Band 4-3-2) in 1999, 2000, 2001, and 2008 showing the gradual changes in the land cover over the study site (e.g. a woody swamp on the NW side of the

tower because of beaver activity and the development of the Bigelow swamp on the SE side.

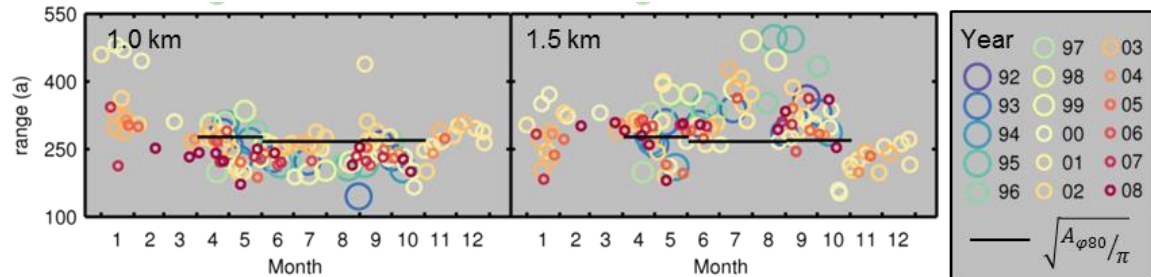


Figure 2.7. Semivariogram parameter, *range*, of EVI in 1.0 km and 1.5 km fields respectively. Years were presented in different colors and sizes (same setup in Fig 1.6). Horizontal black bar is the radius of the circle having the median footprint area in the period ($\sqrt{A_{\phi 80}/\pi}$)

2.3.3. Spatial variation around the flux tower

The \overline{EVI} shows the seasonality of the study field (Figure 2.8), starting with low values in the green-up period (mean and standard deviation between 1992 and 2008: $\mu=0.32$, $\sigma=0.07$), increasing during the mature period ($\mu=0.64$, $\sigma=0.06$), and returning to the initial level in the senescence period ($\mu=0.48$, $\sigma=0.09$). Variations in the ΔEVI in the green-up period were very small (less than 5%) regardless of the window width. The ΔEVI were lower than the \overline{EVI}_{1km} around the tower, where most of the canopy was composed of deciduous species that had not yet started their annual growth cycle. The ΔEVI slightly increased at the window width of 250 m, where the conifer canopies located on the NW, NE, and SE sides of the tower were included, and then gradually converged to the \overline{EVI}_{1km} . This indicates the distribution of vegetation surrounding the tower was heterogeneous in part but offset at the field scales during the green-up period.

Meanwhile, the ΔEVI in the mature and senescence periods reveals strong spatial heterogeneity around the tower in those periods. The ΔEVI around the tower was higher than the \overline{EVI}_{1km} up to 0.1 which is almost 10% of the absolute magnitude of the \overline{EVI}_{1km} , and then gradually converged to zero by the window width of 500 m. This result confirms the semivariogram analysis result that the study field was more spatially heterogeneous during the mature and senescence periods than the green-up period (due to the woody wetlands on NW and SE. As the Bigelow swamp on the SE of the tower developed, heterogeneity during the mature and senescence periods increased. It also indicates that the eddy-flux measured at the tower during mature and senescence periods would be more sensitive to the wind direction and footprint (B. Chen et al., 2012). There was no noticeable variation in the ΔEVI at the window widths larger than 1.0 km. We can also expect that the footprint (φ_{80})-averaged EVI in each period would adequately represent both the \overline{EVI}_{1km} and $\overline{EVI}_{1.5km}$ because the ΔEVI is around zero at the “effective” footprint-width that was calculated by taking root of the median footprint area in each period ($\sqrt{A_{\varphi_{80}}} = 490, 473, \text{ and } 476 \text{ m}$ in the green-up, mature, and senescence periods, respectively).

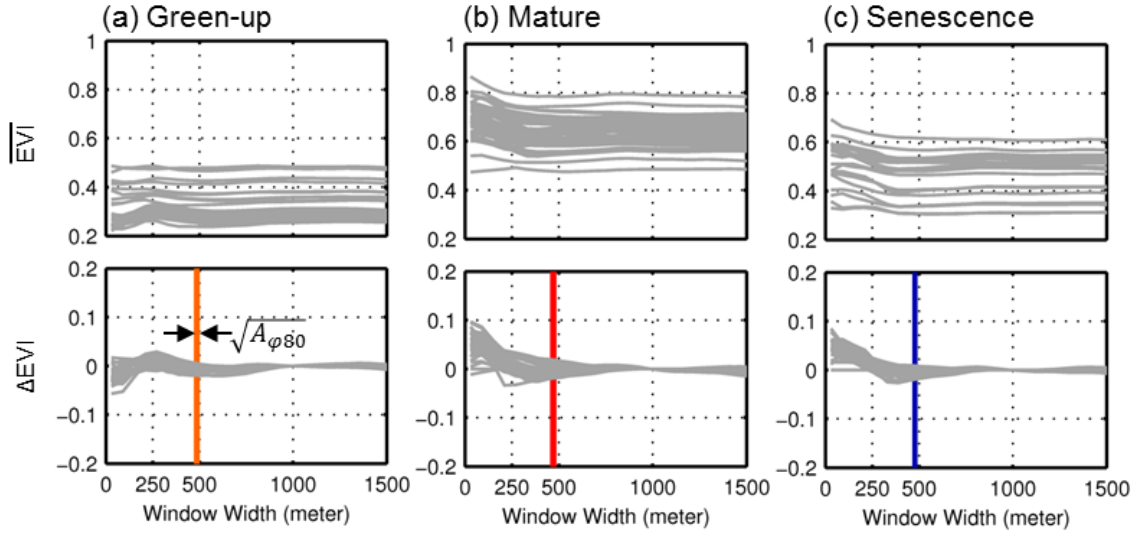


Figure 2.8. The window-averaged EVI value (\overline{EVI} on the top row), and variations of the \overline{EVI} relative to the \overline{EVI}_{1km} (ΔEVI on the bottom row) of all the available EVI data between 1992 and 2008 in (a) green-up, (b) mature, and (c) senescence periods. Vertical colored bar is the window widths having the footprint areas in the period ($\sqrt{A_{\phi 80}}$).

2.3.4. Correlation between EVI and tower GPP

As shown in the semivariogram and window size analyses, the footprints are spatially representativeness of the 1.0 km field, and therefore, the \overline{EVI}_{1km} displayed a good capability in estimating tower-derived daily GPP for the growing season ($r^2=0.72$, Figure 2.9a) as much as the footprint (ϕ_{80})-averaged EVI did ($EVI_{\phi 80-unweighted}$; $r^2=0.72$, Figure 2.9b). There are several studies that have shown improvements in the model performance by weighting the source area fraction (B. Chen et al., 2009; Forbrich et al., 2011), but we did not find any improvement in $EVI_{\phi 80-weighted}$ values as an indicator for the tower-derived GPP compared to the $EVI_{\phi 80-unweighted}$ or EVI_{1km} (Figure 2.9b).

Although the tower-derived GPP can be largely captured with the EVI during the entire growing season, the correlation substantially declined during the mature period with little significant dependence between the two variables ($r^2 = 0.04$, $p > 0.05$), as shown by previous study (Xiao et al., 2004). During the mature season, the anomalies in the environmental drivers, such as photosynthetically available radiation (PAR), land surface temperature (LST) and surface water content, are the important factors to account for the variations in the GPP (Gao et al., 2014; Jahan et al., 2009; Tang et al., 2012). However, these environmental factors also do not fully explain the anomalies in the tower-derived GPP during the mature season, only 40-50% (Urbanski et al., 2007).

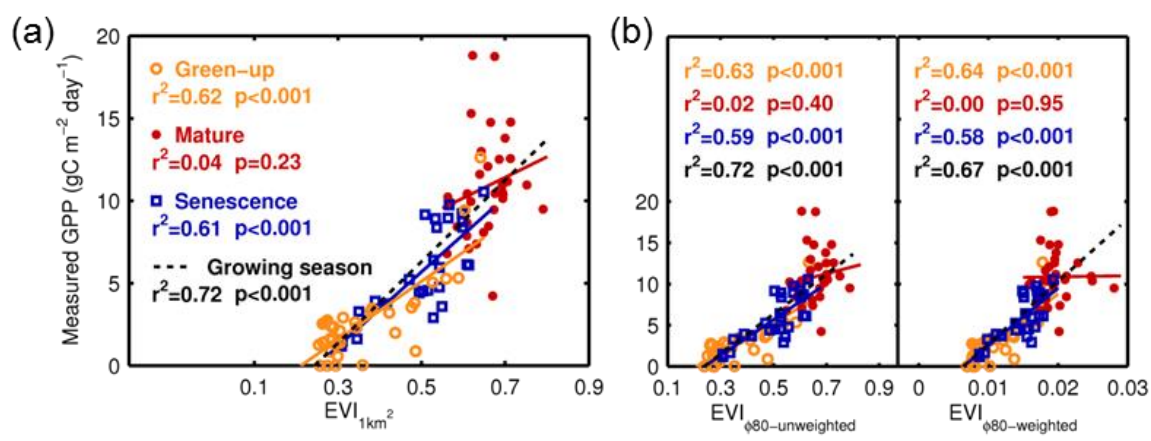


Figure 2.9. Scatterplot and linear regression fit between the tower-derived daily GPP from 1992 to 2008 and (a) the averaged EVI of 1.0 km field (\overline{EVI}_{1km}), (b) the averaged EVI within 80% cumulative footprint function without weighting footprint density ($EVI_{\phi80-unweighted}$), and (c) the averaged EVI within 80% cumulative footprint function with weighting footprint density for the period ($EVI_{\phi80-weighted}$)

2.3.5. Variations in the land cover proportions

Seasonal footprints (φ_{80}) from 1999 to 2008 are overlaid on the land cover maps and only 1.0 km fields are presented in Figure (2.10). The land cover proportion (P_{LC}) estimated by unweighting and weighting the footprint ($\varphi_{80} * P_{LC}$ and $\overline{\varphi_{80}} * P_{LC}$) and the difference between the two methods (ΔP_{LC}) are presented in Figure (2.11). First, in the field scale, the land cover proportions in both 1.0 km and 1.5 km fields (Figure 2.11a) are mostly similar, except that the 1.5 km field includes more non-forest components, especially woody wetland. In NLCD 2001, for example, 1.0 km field consisted of 47.5% of DBF, 22.1% of ENF, 15.0% of MF, 10.9% of woody wetland, and 4.5% of low residential area. 1.5 km field were composed of 44.1% of DBF, 21.6% of ENF, 15.4% of MF, 14.6% of woody wetland, 2.7% of low residential areas, and 1.6% of cultivated crops.

The entire growing season footprints and the mature period footprints were mostly governed by the DBF on the SW side of the EMS-tower, as shown in the location of the density peak points ($\varphi_{80,peak}$) in Figure (2.10), except for the year 2003 when the $\varphi_{80,peak}$ was governed by the NW-side ENF. The $\varphi_{80} * P_{LC}$ of the DBF was 57% in average, varying from 47% in the 2000 growing season to 65% in the 2004 mature period. The $\varphi_{80} * P_{LC}$ of the ENF was 27% in average with a range from 21% in 2004 mature period to 34% in 2003 growing season. During the senescence periods, footprints were governed by the SW-side DBF for four years out of a total of ten years, and the rest years had footprints orientated more toward the NW-side ENF and woody wetlands. The $\varphi_{80} * P_{LC}$ of the DBF was similar over the entire growing season and mature period, but

the $\varphi_{80} * P_{LC}$ of the ENF varied $\pm 2\%$ more, from 19% in 2007 to 36% in 2002. The green-up period footprints were mostly toward the NW side because of the strong and frequent NNW, NE, and E winds, and therefore they contained more ENF and less DBF compared to the mature periods and the entire growing season. In 2003 and 2005, the forest proportion (sum of DBF, ENF, and MF) dropped to 84% due to the strong NE and NNW prevailing winds. The ΔP_{LC} reflects the integrated effect of the footprint distribution and the land cover heterogeneity within the footprint area. The difference was noticeably higher in the periods when the footprint was more over the homogeneous area, for example, the green-up period in 2003, and the senescence period in 2007.

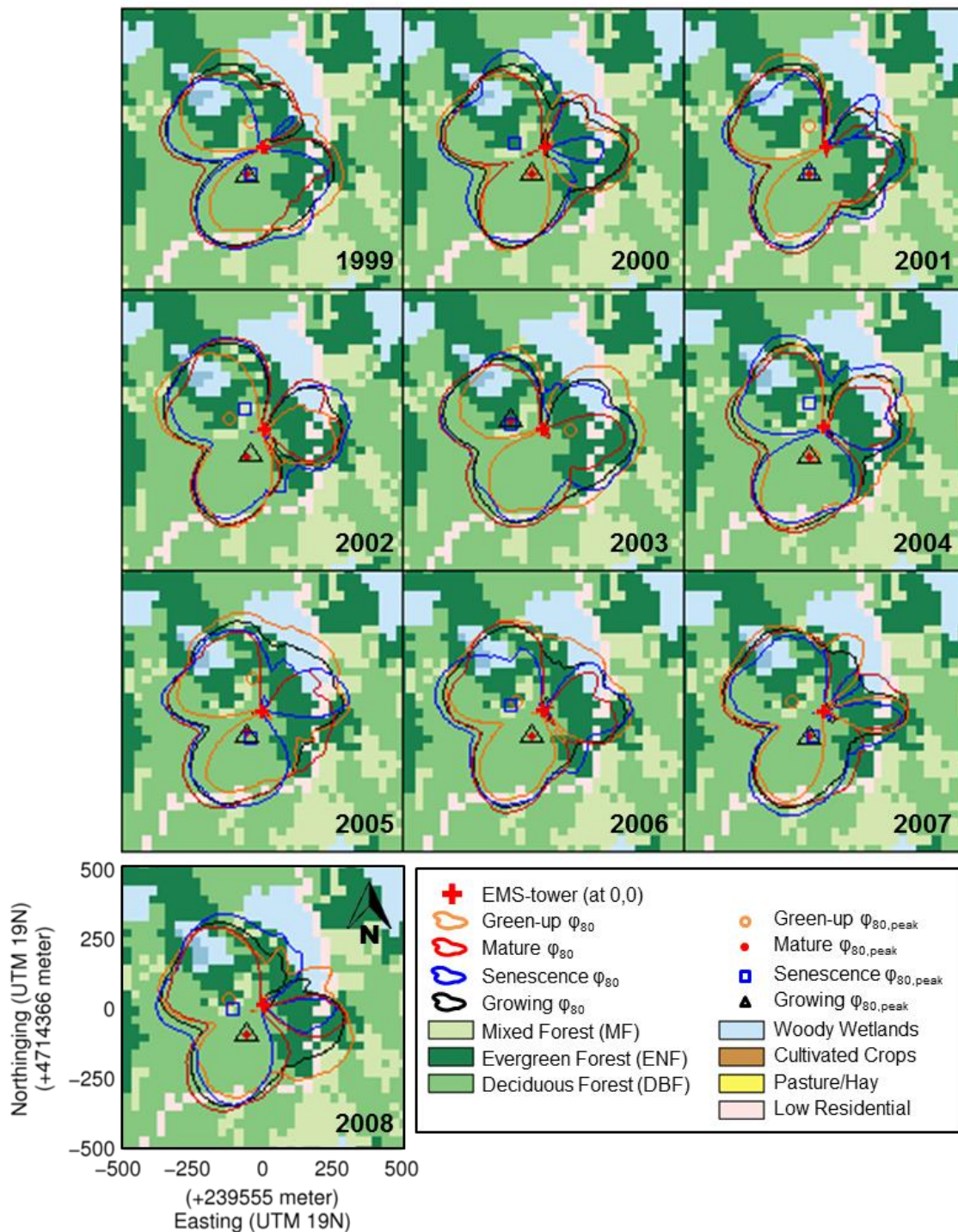


Figure 2.10. Seasonal footprints (ϕ_{80}) from 1999 to 2008 on the land cover maps centered over the EMS-tower (red cross). NLCD 2001 is assigned for the years from 1999 to 2003, and NLCD 2006 for the years from 2004 to 2008 (1.0 km field only). The contours represent ϕ_{80} in each period in the year, and points represent $\phi_{80,peak}$ location.

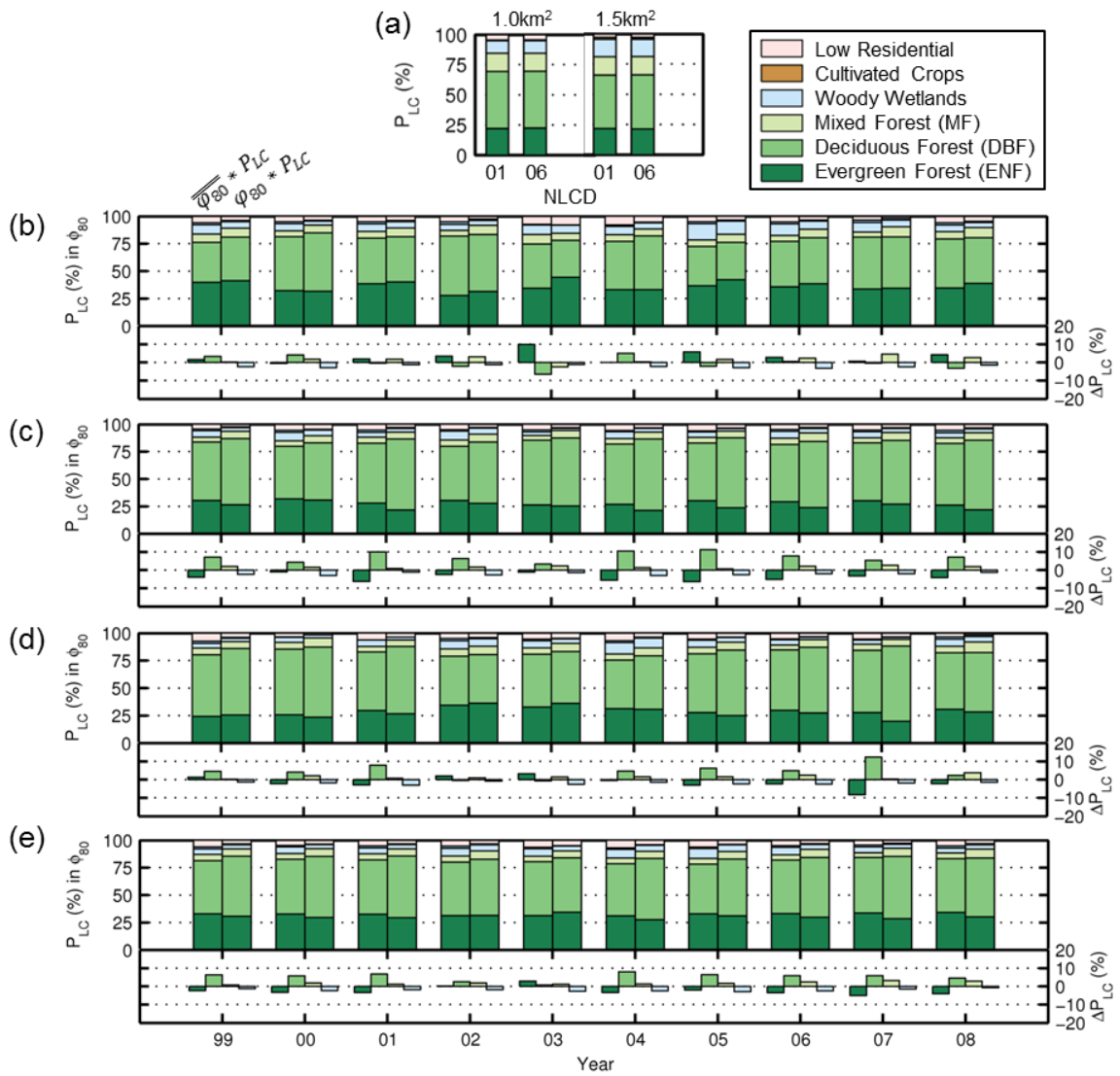


Figure 2.11. The land cover proportion (a) within 1.0 km and 1.5 km fields centered over the EMS tower calculated from NLCD 2001, and 2006 maps. Land cover proportion within footprints estimated by unweighting the footprint density ($\overline{\phi_{80}} * P_{LC}$ bars on the left-side in each year) and by weighting footprint density ($\phi_{80} * P_{LC}$ bars on the right-side in each year) during (b) green-up period, (c) mature period, (d) senescence period, and (e) growing season. Differences between two methods ($\Delta P_{LC} = \phi_{80} * P_{LC} - \overline{\phi_{80}} * P_{LC}$) are presented only for the four major land cover types (ENF, DBF, MF, and woody wetlands).

2.3.6. Impacts of land cover composition on the flux measurement

The results from the correlation analysis between the δP_{LC} and δGPP are summarized in Table (2.1). The best δP_{LC} indicator for δGPP in each period was selected (bold fonts in Table 2.1) based on the coefficient of determination (r^2) and the significance level (p-value), and presented in Figure (2.12). We found 33% of the variations in the δGPP during the green-up can be explained with the δP_{LC} of the sum of the DBF and ENF at 90% significant level ($p=0.08$). Every increment of the DBF and ENF proportion in percent resulted in 13 gC m^{-2} increment in the flux measurement. Urbanski *et al.* (2007) mentioned that wetland and coniferous proportions in the upwind area should be important in the spring flux. However, we found that the δP_{LC} of the sum of the wetland and ENF was less correlated with the δGPP compared to the sum of the DBF and ENF, by 22% (not shown in the Table 2.1), and the correlation was statistically not significant ($p = 0.16$). In the mature period, the δP_{LC} of the ENF was considerably correlated with δGPP at the statistically significant level ($r^2 = 0.48$, $p < 0.05$). The GPP was lower than the seasonal \overline{GPP} by 20 gC m^{-2} for every increment (%) of the DBF proportion within the footprint. The correlation of the δGPP with the δP_{LC} of the other forest types (the sum of the DBF and the MF) was not as high as the ENF ($r^2 = 0.35$, $p = 0.07$, slope = $+13.05 \text{ gC m}^{-2} \%^{-1}$, not shown in the Table 2.1). The GPP of the DBF is approximately 1.7 times higher than the ENF in the study region (Keenan *et al.*, 2013), therefore the negative effect of including more ENF portion in the tower footprint is reasonable. Having more ENF proportion in the footprint had a positive effect on the tower-measured GPP during senescence period, but the magnitude was small ($5 \text{ gC m}^{-2} \%^{-1}$).

¹) and the correlation was weak and not significant ($r^2 = 0.20$, $p = 0.19$). Although the ENF had the negative effect on the δGPP at the entire growing season scale ($-30\text{gC m}^{-2} \text{ \%}^{-1}$) as it did on the δGPP during the mature period, the correlation was weak and not significant ($r^2 = 0.24$, $p = 0.15$) and we found no other $\delta\text{P}_{\text{LC}}$ indicator that can explain δGPP at the entire growing season scale better than the ENF.

Table 2.1. Linear regression results between GPP anomalies in each period (δGPP) and land cover proportion anomalies ($\delta\text{P}_{\text{LC}}$): correlation coefficients (slope, β_1) and coefficient of determination (r^2)

		δGPP	Green-up	Mature	Senescence	Growing
			β_1 r^2	β_1 r^2	β_1 r^2	β_1 r^2
φ_{80} *	P_{LC}	DBF	4.677 0.20	11.12 0.27	-1.19 0.07	18.63 0.15
		ENF	-5.91 0.15	-20.34** 0.48	1.57 0.05	-30.11 0.24
		MF	13.18 0.04	54.60 0.12	-2.05 0	37.26 0.04
		DBF+ENF	15.17 0.27	2.73 0	-3.06 0.07	0.71 0
		All (DBF+ENF+MF)	13.67 0.28	13.51 0.04	-4.29 0.11	10.47 0.01
		DBF	4.02 0.1	9.74 0.12	-3.01 0.18	27.43 0.13
$\overline{\varphi_{80}}$ *	P_{LC}	ENF	-0.22 0	-25.84 0.33	5.19 0.2	-4.89 0
		MF	-12.86 0.05	97.29 0.32	-3.16 0	-121.20 0.19
		DBF+ENF	13.01* 0.33	-0.98 0	-3.32 0.07	13.84 0.06
		All (DBF+ENF+MF)	15.23 0.32	11.74 0.03	-3.79 0.09	9.58 0.02

** $p < 0.05$ * $p < 0.1$ **bold-font**; best $\delta\text{P}_{\text{LC}}$ indicator for the seasonal δGPP

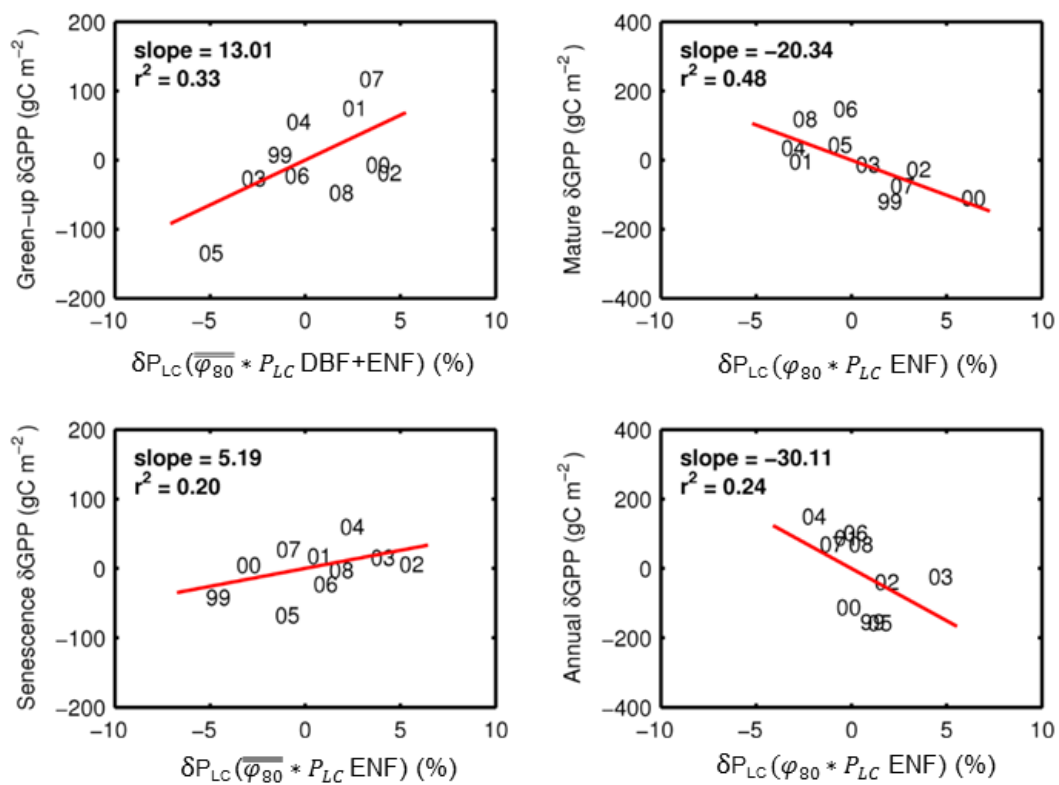


Figure 2.12. Scatterplots and linear regression fits between the tower-derived daily GPP anomalies (ΔGPP) and the selected land cover proportion anomalies (ΔP_{LC}) in each period

2.4. Discussion and conclusion

In this study, we assessed the representativeness of a flux tower footprint located in a mixed temperate forest for a regional scale in terms of vegetation density variation as well as land cover composition. We examined the landscape at the spatial scale of the MODIS (1.0 km and 1.5 km), one of the widely applied remote sensing data for ecosystem studies, by using Landsat TM/ETM+ datasets from which we can acquire decades of intra-annual surface information at a finer resolution (30 m).

The extents and the shapes of tower footprints were largely determined by the wind direction. In the study site, prevailing wind directions were SW and NW, but sporadic strong winds from N and E stretched tower footprints out toward N and E landscapes, where coniferous stands dominate, especially during green-up. Mature periods had generally smaller footprints relative to other periods, extended toward SW and NW which landscapes are mostly composed of deciduous stands.

The vegetation density variation at sub-pixel scale, estimated with the EVI retrieved from Landsat TM/ETM+, had noticeable seasonal variability, following the phenological cycle of the deciduous stands. It was relatively high during dormancy and very low during growing season once the forest canopies within the pixels were closed (*nugget effect* in Figure 2.6a). Our results suggest that the vegetation density variation in the study fields were more heterogeneous during mature and senescence periods than green-up period (higher *sill* in Figure 2.6a and smaller *range* values in Figure 2.7). The tower footprints covered enough area to adequately represent the average magnitude of

the vegetation density as well as the variation in the density distribution within the 1.0 km and 1.5 km fields (Figure 2.8).

Due to the heterogeneous land cover around the flux tower, footprint land cover composition changed as the extent and the shape of tower footprints varied seasonally and interannually. We found that 48% of anomalies in the mature period GPP can be explained solely by anomalies in the proportion of ENF calculated by weighting footprint density. More ENF area included in the tower footprint during a mature period in a year, smaller GPP measured at the tower in the year compared to the average mature period flux from 1999 to 2008. There are also small correlation that larger DBF and ENF area in the tower footprint during green-up period resulted in higher flux compared to the average from 1999 to 2008.

Future work will focus on assessing the within-seasonal flux variations resulting from the variabilities in the footprint land cover composition. The variabilities in other flux towers footprints locating in mixed forests will be also analyzed. In the Harvard Forest, the growth of red oak has been increasing over the last decade and oak has become the dominant species. The correlation between the flux anomalies and the footprint land cover composition, therefore, depend on the changes in the landscape, and the significance of this correlation needs to be quantified in future work.

This study suggests that our understanding of ecosystem behaviors would be largely improved by examining spatial representativeness of tower flux footprints for the regional ecosystem and implementing the footprints into our current ways of using flux measurements, especially in mixed forests. These analyses would help to identify and

select desirable flux towers that appropriately represent the broader regional ecosystems so that one can actually compare the characteristics of multiple ecosystems. One could also reduce the errors in the processes of calibrating and validating biome-specific parameters in ecosystem models as well as in remote sensing-based estimates with the knowledge of how much proportion of the flux was measured from the targeted land cover or forest type.

Chapter 3. Long-term carbon and water cycles in mixed forest catchments: ecohydrological modeling from patch-scale to catchment-scale

3.1. Introduction

For the past three decades, dozens of terrestrial ecosystem models have been developed to improve our understanding of the ecosystem processes and to predict the responses of those ecosystems to climate changes. These ecosystem models were built upon different approaches: regression approaches between climate drivers and vegetation responses (e.g., Urbanski et al., 2007), model-data fusion frameworks that constrain model parameter with field observations (e.g., Keenan et al., 2012), and process-based approaches using theoretical understanding of relevant underlying processes (e.g., Running & Hunt Jr, 1993). These ecosystem models have shown their ability to reproduce the patterns in field measurements related to certain underlying processes, but most of them were evaluated over relatively short-periods of time (several years) at a particular spatial scale. Most frequently these were at a stand-species scale (Medvigy et al., 2009), or a canopy scale as an aggregation of several plant function types within the scale (Kucharik et al., 2006). These ecosystem models have a hierarchical structure allowing vertical nutrient (carbon, water, and nitrogen) transport between functional units (leaf level(s), soil level(s)), but most of the models do not consider the lateral transport of nutrients between adjacent spatial units.

The lateral transport, however, is a key process in hydrology including surface runoff and subsurface flow. Most of the hydrological models (e.g. the most-widely used hydrological model SWAT (Arnold et al., 1998)) have modeling schemes based on the hydrological response units, such as sub-basins and hillslopes, and simplified representations of aboveground ecosystem processes. Therefore, the hydrological models may not adequately describe the nutrient cycles in the region where there are multiple species distributed over the landscape, e.g. mixed forests.

Regional Hydro-Ecologic Simulation System, RHESSys (Band et al., 1993; Tague & Band, 2004), is a process-based ecohydrological model able to simulate carbon, water and nitrogen cycles (storages and fluxes) throughout components (vegetation, soil, and stream) at the catchment scale. It integrates a number of algorithms evolved from several existing independent and specialized models: Biome-BGC (Running et al., 1993) to account for carbon and water cycles, DHSVM (Distributed Hydrology Soil Vegetation Model; Wigmosta et al., 1994) to explicitly represent spatially distributed hydrologic pattern through a landscape, CENTURY_{NGAS} (Parton et al., 1993; Parton et al., 1996) for enhanced nitrogen processes, and MT-CLIM (Running et al., 1987) to extrapolate microclimate conditions through the landscape depending on elevation, aspect and slope. The Geographic Information System (GIS)-based framework of RHESSys allows it to directly incorporate remote sensing data to describe the fully-distributed spatial information such as land cover, soil type, leaf area index (LAI), and topographical information (slope, aspect and elevation) from digital elevation model (DEM). The spatial information is partitioned into a nested series of functional dimensions (a so called

“patch”) with which microclimate, hydrological, and ecological processes are associated. RHESSys allows lateral nutrient (carbon and nitrogen) transport by the lateral hydrologic connectivity between adjacent patches, in the forms of dissolved organic carbon (DOC) and dissolved organic nitrogen (DON) in surface lateral flow and subsurface lateral flow. RHESSys has been applied and evaluated at a number of ecohydrological study sites across different types of ecosystems; a high-elevation mountain watershed, a snow-dominated mountain ecosystem, a Mediterranean ecosystem, and deciduous-conifer ecosystems in a humid continental climate (Baron et al., 2000; Christensen et al., 2008; Nemani et al., 1993; Tague et al., 2009; Vicente-Serrano et al., 2015). Because of its structural framework, all the processes are simulated at every patch, and RHESSys is capable of describing ecosystem processes in a spatially complex landscape; such as spatial patterns of vegetation growth and species in topographically-varying regions (Mackay & Band, 1997; Meentemeyer & Moody, 2002; Tague et al., 2009), for landslide hotspot prediction (Band et al., 2012; Hwang et al., 2015), and for hydrological processes in a spatially-segmented urban area (Mittman et al., 2012; Shields & Tague, 2012; Tague & Pohl-Costello, 2008).

The objectives of this chapter are to (1) calibrate and validate a spatially distributed process-based ecohydrological model at mixed forest headwater catchments in the Harvard Forest Long Term Ecological Research (LTER) site, where long term eddy-flux measurements are available along with various independent ground data, and (2) to analyze the long-term patterns of carbon uptake and water flux at the patch scale as well as at the catchment scale in this mixed forest site

3.2. Model Overview - Summary of key processes

As mentioned, RHESSYS couples a number of process models to appropriately capture the biogeochemical and hydrological functions of an ecosystem in a spatial distributed manner. The key process models are described below. Detail description about RHESSys is primarily available at (Tague et al., 2004).

Farquhar photosynthesis model

The net carbon assimilation of C3 plants is assumed to be constrained by either the maximum carboxylation rate (A_v) or the electron transport rate (A_j) (Farquhar et al., 1980). The maximum carbon uptake rate (A), therefore, is determined by the minimum of these two rates.

$$A = \min(A_v, A_j) \quad (3.1)$$

where the carboxylation rate (A_v) and the electron transport rate (A_j) are expressed as

$$A_v = V_{Cmax} \cdot \frac{C - \Gamma_*}{C + K_C(1 + O/K_O)} - R_d \quad (3.2)$$

$$A_j = J \cdot \frac{C - \Gamma_*}{4.5C + 10.5\Gamma_*} - R_d \quad (3.3)$$

where V_{Cmax} represents the maximum carboxylation velocity ($\mu\text{mol} \cdot \text{m}^{-2} \cdot \text{sec}^{-1}$; a linear function of leaf nitrogen content, nitrogen in Rubisco, and temperature-dependent Rubisco activity) and J represents the electron transport rate ($\mu\text{mol} \cdot \text{m}^{-2} \cdot \text{sec}^{-1}$. root of a quadratic function having the maximum electron transport rate and effective irradiance in its coefficients; Farquhar & Caemmerer, 1982). A_v and A_j are controlled by Rubisco

activity and Ribulose-1,5-bisphosphate (RuBP) generation, therefore they are also described as Rubisco-limited photosynthesis or RuBP-limited photosynthesis, respectively. C and O are intercellular partial pressure of CO_2 and O_2 within leaf (Pa in this study). K_c and K_o are the Michaelis-Menten constant of Rubisco for CO_2 (carboxylase reaction) and O_2 (oxygenase reaction) respectively. Γ_* and R_d indicate CO_2 compensation point(Pa) and the dark respiration rate (i.e. leaf respiration in $\mu\text{mol m}^{-2} \text{sec}^{-1}$).

Modified Penman-Monteith evapotranspiration model

Total potential evapotranspiration rates are decided as the sum of the evaporative fluxes from the intercepted water on the canopy and the litter, sublimation from the snowpack on the ground and on the canopy, and diffused water vapor from inside the sunlit- and sunshade-leaves (transpiration) (Tague et al., 2004). Each flux is calculated using the modified Penman-Monteith equation (McNaughton and Jarvis, 1983), which takes the coupling effects of climate variables on evaporation. It is assumed that transpiration does not occur during rainfall and as long as intercepted water still exists on the leaf surface.

$$E = \frac{s \cdot R_{net} + \rho_a \cdot c_p \cdot g_a \cdot VPD}{\lambda [s + \gamma \left(1 + \frac{g_a}{g_s}\right)]} \quad (3.4)$$

where s is the rate of change of the saturation vapor pressure with temperature, R_{net} is the incidence flux density (W m^{-2}), ρ_a is the density of air as a function of temperature, c_p is the specific heat of air ($\text{J kg}^{-1} \text{ }^\circ\text{C}^{-1}$), g_a is the aero-dynamic conductance (m s^{-1}),

VPD is the vapor pressure deficit (Pa), λ is the latent heat of vaporization (2.4-2.5 MJ kg^{-1}), γ is the psychrometric constant (65-68 Pa K^{-1}). g_s (m s^{-1}) is the atmospheric heat conductance for evaporation process, otherwise it stands for the stomata conductance, indicating stomatal control on transpiration.

Jarvis stomata conductance model

The diffusion processes of two gas molecules (CO_2 molecule and water vapor) between atmosphere and inside the leaf follow concentration gradients of its own, and they are physically coupled under the control of the stomata. The gas exchange rate through stomata (stomata conductance, g_s) is computed based on the Jarvis multiplicative model (Jarvis, 1976) for sunlit and shaded leaves separately ($g_{s,\text{sunlit}}$ and $g_{s,\text{shaded}}$) (Chen et al., 1999).

$$g_s = g_{s,\text{max}} f(\text{APAR}) \cdot f(\text{VPD}) \cdot f(\Psi) \cdot f(T_{\text{avg}}) \quad (3.5)$$

where $g_{s,\text{max}}$ is the species-specific maximum stomatal conductance, and f is the multiplicative function to account for stomata response to the environment driver (light, water stress, and temperature) from 0 (completely closed stomata) to 1 (no effect on stomata) (Körner, 1994). It is assumed that stomata response to the each environmental factor is independent, and therefore, the net response is expressed as the simple multiplication of the individual functions.

Vegetation dynamics

Allocation is a key physiological metabolism factor determining plant growth by proportioning assimilated carbon into the compartments (roots, stems, and leaves), therefore it is an important factor in simulating vegetation responses to the availability of each resource (light, water, and nutrient etc.). Following Biome-BGC (White et al., 2000), species-specific constant ratios were applied to determine (1) the amount of carbon out of the total newly assimilated carbon available for allocation after taking out autotrophic respiration (maintenance and growth respirations), and (2) the partitioning of the carbon into each of the growing compartments (roots, stems, and leaves). The actual amount of carbon to be consumed to grow each part is proportionally rescaled depending on nitrogen availability.

Daily turnover rates at a structural level (leaf, fine-root, coarse-root and live-stem) and mortality at a stand level (annual mortality and fire mortality) decide the secondary C and N fluxes by transferring a certain fraction of C and N from the first storage areas into the secondary pools (coarse woody debris, litter, and soil). These rates are assumed to be physiologically characteristic (species-specific parameters), therefore, they are set to a constant without any specified disturbances such as distinguishable hurricane, fire and insect outbreaks. Competition between species is not considered in this study.

Vertical hydrologic processes

After the aboveground hydrologic processes (gross precipitation, interception by leaves and litters, and partition of throughfall into surface flow and infiltrated water) have

been considered, the belowground hydrologic processes start with partitioning the infiltrated water into subsurface and ground storages. Rootzone soil moisture not only regulates ecophysiological responses of vegetation to drought condition, but also adjust decomposition activity of microbial community in the soil which provide nutrients (nitrogen, for example) that vegetation need to grow. Soil moisture in the rootzone (ΔS) is calculated assuming the water mass is balanced (Eq. 3.6).

$$\Delta S = q_{infl} + q_{cap} - q_{drain} - ET \quad (3.6)$$

where q_{infl} , q_{cap} , and q_{drain} refer to infiltration, capillary rise and drainage respectively, and ET is evapotranspiration at sunlit and sunshade leaves by plant uptake from the rootzone. Detailed descriptions of each flux is available at Tague & Band (2004).

Hydraulic fluxes (q_{infl} , q_{cap} , and q_{drain}) are largely determined by vertical hydraulic conductivity profile, which describes the soil's property of transmitting water.

RHESSys adapts an exponential profile to estimate saturated hydraulic conductivity at the depth z , $K_{sat}(z)$ (meters day⁻¹) unless specific field measurements are available;

$$K_{sat}(z) = K_{sat0} \cdot e^{-z/m} \quad (3.7)$$

where K_{sat0} is hydraulic conductivity (meters day⁻¹) at the surface and m (meter⁻¹) indicates the decay rate of the conductivity with depth z .

Lateral redistribution

Lateral hydrologic fluxes (Hortonian overland flow and saturated subsurface throughflow) follow the explicit routing path driven by surface topography assuming that hydraulic gradients are parallel to the surface topography (Distributive Hydrology Soil

Vegetation Model; Wigmosta et al., 1994). Lateral redistribution of hydrologic flows modulates the entire BGC-cycles in various dimensions, for example, by altering soil moisture which is a critical factor on soil respiration at Harvard Forest (Savage et al., 2001). Soil respiration rate is a signature of the decomposition rate of the soil organic matter, therefore, eventually indicating the soil moisture control on nitrogen availability through the following processes such as mineralization and nitrification.

3.3. Materials and Methods

3.3.1. Study site overview

The main study sites are two adjacent headwater catchments, Bigelow-Brook (42.53901°N, 72.17201°W) and Nelson-Brook (42.53485°N, 72.18654°W), on the Prospect Hill Tract of the Harvard Forest in Petersham, Massachusetts (Figure 3.1). Harvard Forest was designated as a Long Term Ecological Research site in 1988 (<http://harvardforest.fas.harvard.edu/>), and three towers have been measuring gas (CO₂ and water vapor) exchange between ecosystem and atmosphere using the eddy covariance technique (Baldocchi et al., 1988; Goulden et al., 1996). These towers have operated since 2004 at the Hemlock tower site (Fluxnet site code: US-Ha2, referred to as the "HEM-tower" hereafter), since 2002 at the Little Prospect Hill tower site (without a Fluxnet site code), and since 1991 at the Environmental Measurement Site tower (US-Ha1, referred to as the "EMS-tower" hereafter), which is the world's longest record of flux exchange. Harvard Forest is dominated by a cool and moist temperate climate with

an annual mean temperature of 8.5°C, varying from 20°C in July to -7°C in January. Mean precipitation is approximately 1100mm and distributed evenly throughout the year, 25% of which falls as snow (Xu et al., 2012). The moderate topography ranges from 250m to 430m above sea level. The forest is mainly dominated by northern red oak (*Quercus rubra L.*), red maple (*Acer rubrum L.*) and eastern hemlock (*Tsuga canadensis L.*), black birch (*Betula lenta L.*) and white pine (*Pinus strobes L.*). Stands are generally 75-110 years old, re-established on abandoned farmlands and re-grown after hurricanes, including the most recent and strongest one, the Great Hurricane of 1938. Soils are generally well-drained sandy-loam types (NRCS, 2009) with about 3m-depth derived from the gneiss and schist bedrock with acidity of pH 4.2-4.7 (Currie *et al.*, 1996; Xu & Saiers, 2010). There are some very poorly drained woody wetlands.

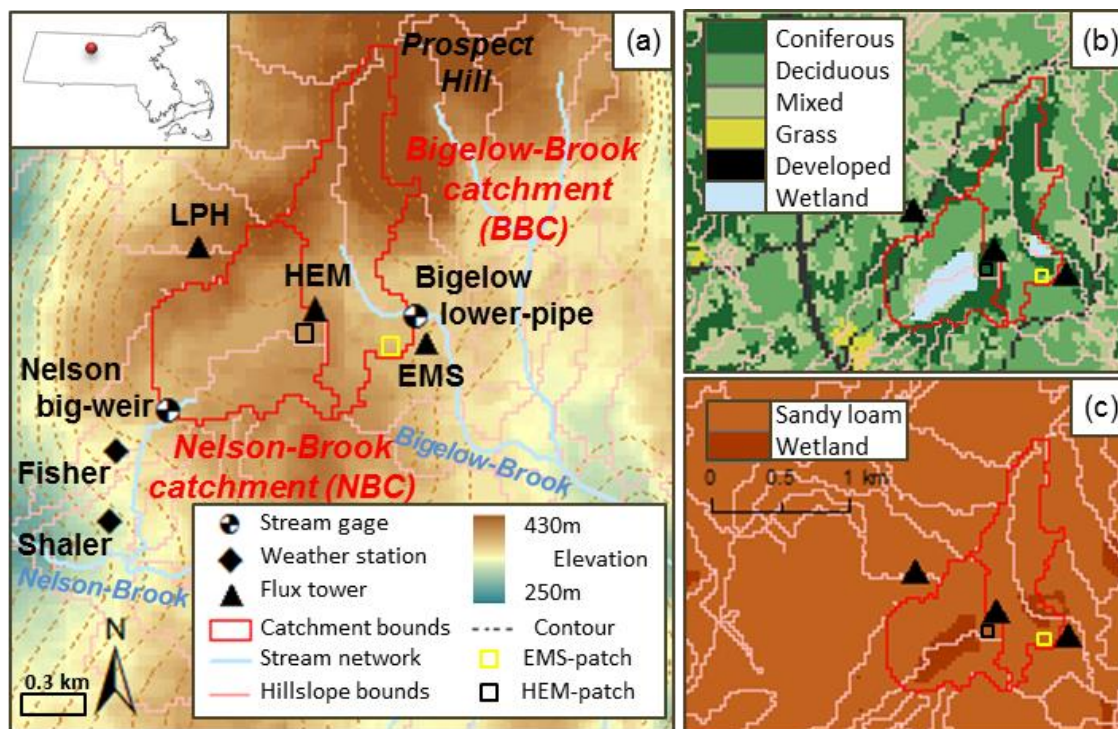


Figure 3.1. Two study catchments on the Harvard Forest Prospect hill. (a) Catchment boundaries (red lines) and stream networks (cyan lines) for Bigelow-Brook catchment (BBC) and Nelson-Brook catchment (NBC) delineated by Bigelow lower pipe and Nelson big weir (black and white divided circles). This study mainly incorporated; meteorological data from Fisher and Shaler weather stations (diamonds), and water and carbon flux from HEM and EMS towers (triangles). Canopy-level results are from the area in black and yellow squares, for HEM-tower and for EMS-tower respectively (b) Vegetation was reclassified from 2001 National Land Cover Dataset (NLCD). (c) Soil distribution, generated by aggregating soil classes in the USDA National Resources Conservation Service (NRCS) soil survey database.

3.3.2. Data overview

Station measurements: meteorological and hydrological data

Daily meteorological data (maximum, minimum and average temperature and precipitation) have been measured at Shaler station since 1964 (Harvard Forest LTER archive ID: hf000. Boose & Gould, 1999), and have been succeeded by the Fisher station in 2001 (Harvard Forest LTER archive ID: hf001. Boose, 2001). Both stations are located close to the study sites. Gaps in the temperature data were filled by averaging the median temperature of the 20-years with the median temperature of the 10-days surrounding the day without data. Gaps in precipitation data were filled by taking the average of nearby National Climate Data Center (NCDC) records from four stations (GHCND Name-ID: Orange Municipal Airport-USW00054756, Birch Hill Dam-USC00190666, Barre Falls Dam- USC00190408).

For the first two years of the Harvard LTER hydrological monitoring project, stream discharge was estimated occasionally based on the water levels at each outlet point (Bigelow lower and upper pipes and Nelson small and big weirs) from May 16, 2005 to December 31, 2007 (Harvard Forest LTER archive ID: hf070-02. Boose, 2007). Starting December 21, 2007, continuous daily discharges have been estimated from 15-min interval automatic pressure transducers (Harvard Forest LTER archive ID: hf070-03. Boose, 2007). Uncertainty in the observed/estimated discharge varies depending on the measurement methods, from 0.1% by pressure transducers up to 20% by the stage measurement (Harmel et al., 2006).

Tower measurements: eddy-covariance flux and ancillary climate data

This study used hourly GEE estimates and water vapor flux measurements (F_{H_2O} , equivalent to ecosystem evapotranspiration, ET) from 1992 to 2008 at EMS-tower (Harvard Forest dataset ID: HF004; Munger & Wofsy, 1999), and half-hourly flux data from 2004 to 2008 at HEM-tower (Harvard Forest dataset ID: HF103; Hadley, 2003). Both datasets are open to the public research and available at the website (<http://harvardforest.fas.harvard.edu/data-archive>). Gross ecosystem exchange (GEE, Eq. 3.8) is the sum of day-time net ecosystem exchange ($NEE_{day-time}$) measurement and ecosystem respiration (R_e) that is empirically scaled based on night-time NEE measurement depending on the air and soil temperature (Falge et al., 2001; J. Lloyd et al., 1994)

$$\begin{aligned} GEE &= NEE - R_e & (3.8) \\ &\approx NEE_{day-time} - NEE_{night-time,scaled} \end{aligned}$$

Sub-daily GEE and water fluxes were integrated to daily fluxes for those days when there were missing gaps existing due to equipment failure and poor quality. It should be noted that this study adapted the GEE data at EMS-tower with quality-filtering and gap-filling processes (HF004-02.filled) for this long-term trend analysis even though gap-filling processes inevitably require assumptions can also cause uncertainty and errors in the results (Urbanski et al., 2007). The daily GEE flux was converted to daily gross primary productivity (GPP) rate, assuming photo-respiration (dark respiration) and the effect of understory canopy are ignorable ($GPP \approx -GEE$). Negative sign indicates the conversion from the gas exchange (uptake from the atmosphere to the vegetation) to the

vegetation productivity (emission from the vegetation to the atmosphere). For this study, flux data measured at the HEM-tower was accepted only when the wind blew from southwest (190-225 degree) where the eastern hemlock and white pine stands are located. ET flux at both towers measured during rainy days was removed because of the significant but unpredictable factors that come with rainfall (Loescher et al., 2005) (e.g., a rapid change in pressure in tubes due to the sudden cooling of the skin from the rain, water droplets on the anemometer affecting pulse times, and moisture in all the electronic instruments producing electrical noise (Hadley et al., 2002)).

Atmospheric CO₂ concentration (parts per million:ppm) data measured at the EMS and HEM towers were combined to produce daily regional atmospheric CO₂ mixing ratio in the study area. Abnormal peaks and drops (>420 ppm and <340 ppm) were removed from the data. Gaps were filled by combining the reference annual cycle, the average of annual cycles from 1992 to 2008, to the long-term trend measured from the ice cores at East Antarctica (Etheridge et al., 1996). Additional meteorological data are collected as following: daily median vapor pressure deficit (VPD) estimated at HEM-tower, daily median wind speed above canopy (29 m) measured by sonic anemometer on EMS-tower, daily total photosynthetically active radiation (PAR) above canopy (28 m) at EMS-tower.

Field measurements: soil, leaf, and tree data

Ground-measured LAI, diameter at breast height (DBH) and soil data (temperature, surface CO₂ efflux, and moisture) were used for model calibration and performance evaluation. Since the flux measured at a tower comes from the surface at the prevailing wind direction, which is the southwest in the Harvard Forest (except the period between December 1992 and February 1993 when northwest winds were dominant, Barford *et al.*, 2001), ground-measurements only from the southwest were used in this study. Basal area increment (BAI) was calculated using DBH measurements of dominant trees: red oak and red maples (EMS-tower), and eastern hemlock and white pine (HEM-tower). Only live trees from 1999 to 2008 were considered and dead or newly counted trees were excluded in the calculation. DBH measurements of eastern hemlock and white pine were taken within the EMS-tower footprint due to the lack of data within the HEM-tower footprint. A summary of data sets descriptions (archive ID, period, transect ID or compass angle, instrument or method, and data set original investigators) used in this study is given in the Table 3.1. Detailed maps of transects are available at the Harvard Forest LTER archive (<http://harvardforest.fas.harvard.edu/data-archive: hf069-01> and [hf069-02](http://harvardforest.fas.harvard.edu/data-archive: hf069-02)).

Table 3.1. List of ground-measurements used in this study

	EMS-tower		HEM-tower	
	Data ID	Description	Data ID	Description
Soil CO ₂ efflux and temperature	hf006-01 ¹	1995 June - 2004 Dec Southwest transects (SWF,SWM) dynamic chamber systems	hf148-01 ³	1997 July - 2000 Apr : 210,240,270 transects 2000 Apr-2007 Nov : 195,225,255 transects LI-6200 System
	hf069-10 ²	1998 June - 2003 Oct 232, 243 transects (B,C) LICOR-6252 Munger & Wofsy (1999)		
Soil moisture	hf006-01 ¹	1995 June - 2004 Dec Southwest transects (SWF,SWM) 15-cm TDR-probe	hf153-02 ⁴	2004 May - 2007 Aug 195,225,255 transects soil core samples at 10-15cm
	hf069-09 ²	1998 June - 2003 Oct 232, 232, 243 transects (B,C) 15-cm TDR-probe Munger & Wofsy (1999)		
Leaf area index (LAI)	hf069-03 ²	1998-1999, 2005-2008 232, 243 transects (B,C) LAI-2000 Munger & Wofsy (1999)	hf150-01 ⁵	2008 Aug 195,225,255 transects LAI-2000
Tree data	hf069-11 ²	1999-2008 232, 243 transects (B,C) DBH of red oak and red maple	hf069-11 ²	1999-2008 232, 243 transects(B,C) DBH of eastern hemlock and white pine

TDR: time-domain reflectometry probes

Datasets original investigators : ¹Davidson & Savage (1999) ²Munger & Wofsy (1999)

³Hadley (2009) ⁴Hadley (2009b) ⁵Hadley (2009c)

3.3.3. Modeling procedure

Modeling site configuration and description

Stream networks and boundaries of the two catchments were derived from the Global Digital Elevation Model version-2 (GDEM V2) at the 1 arc-second resolution (equivalent to approximately 30-meter at the equator) using GRASS Geographic Resources Analysis Support System (GIS) [<http://grass.osgeo.org/>]. Bigelow lower-pipe and Nelson big-weir are the outlet points of the Bigelow-Brook catchment (referred to as “BBC” hereafter) and Nelson-Brook catchment (referred to as “NBC” hereafter), respectively (Figure 3.1). BBC is the headwater of Quabbin reservoir, the largest inland water feature in Massachusetts and the biggest source of water for Boston and its vicinity. The delineated catchment boundaries agree with the catchments’ map on the Harvard Forest website [<http://harvardforest.fas.harvard.edu/meteorological-hydrological-stations>].

Despite the mild slopes in the area, topography does influence plant distribution: broadleaf deciduous vegetation are distributed on east-facing hill of BBC and on south-facing hill of NBC, whereas coniferous vegetation dominate the west-facing hill of BBC and the north-facing hill of NBC. Woody wetlands can be found where the local terrain is relatively flat, on about 6% of BBC and 20% of NBC.

EMS-tower is located about 70-meters away from the closest southeast boundary of BBC and the majority of the footprint of EMS-tower is not included in the BBC when considering the dominant south-west wind direction. Several patches within BBC that are close to the EMS-tower were selected based on the aspect and slope of the hill as well as soil and vegetation types as a “virtual footprint” of EMS-tower (yellow square in Figure

3.1, referred to as “EMS-patch” hereafter). The footprint of the HEM-tower is located within the NBC, and therefore several patches of NBC within the footprint were selected for the canopy-scale evaluation (black square in Figure 3.1. referred to as “HEM-patch” hereafter). Despite of their spatial proximity, there is a noticeable difference in the vegetation composition in the footprint of each tower: 74% basal area of EMS tower footprint is dominated by deciduous species (red oak and red maple) and 83% basal area of HEM tower footprint is mainly hemlock (Belmecheri et al., 2014; Fluxnet web: <http://fluxnet.ornl.gov/site/887>).

Modification using field data: decomposition scaling factor

The conventional way of estimating heterotrophic respiration rates with an exponential function (Eq. 3.9), known as Q_{10} respiration, tends to underestimate the respiration rates at low temperatures, and overestimate the rates at high temperatures (J. Lloyd et al., 1994). RHESSys uses an adaptation of the potential decomposition rate scaling factor (t_{scalar}) from Lloyd & Taylor (1994), which accounts for the complex variation of activation energies of reacting organisms in a simplified exponential function (Eq. 3.10).

$$Q_{10} \equiv \left(\frac{R_2}{R_1}\right)^{\left(\frac{10}{T_2-T_1}\right)}, R_2 = R_1 \cdot e^{\left(\frac{T_2-T_1}{10}\right) \cdot \ln(Q_{10})} \quad (3.9)$$

$$t_{scalar} = R_{10} e^{308.56 \left(\frac{1}{a} - \frac{1}{T_{soil}(K)-b}\right)} \quad (3.10)$$

where a and b are data-set dependent variables, in other world, they are site-specific parameters. The soil decomposition rate is substantially underestimated with the default

coefficients ($a=71.02$ and $b=227.13$, Tague & Band, 2004), also showing systematic bias at high temperatures (Figure 3.2). The coefficients, a and b , were estimated based on the field-measured soil respiration data using the nonlinear regression function, *nlinfit*, in Matlab (Matlab R2013a, MathWorks Inc., Natick, MA) ($R^2=0.72$).

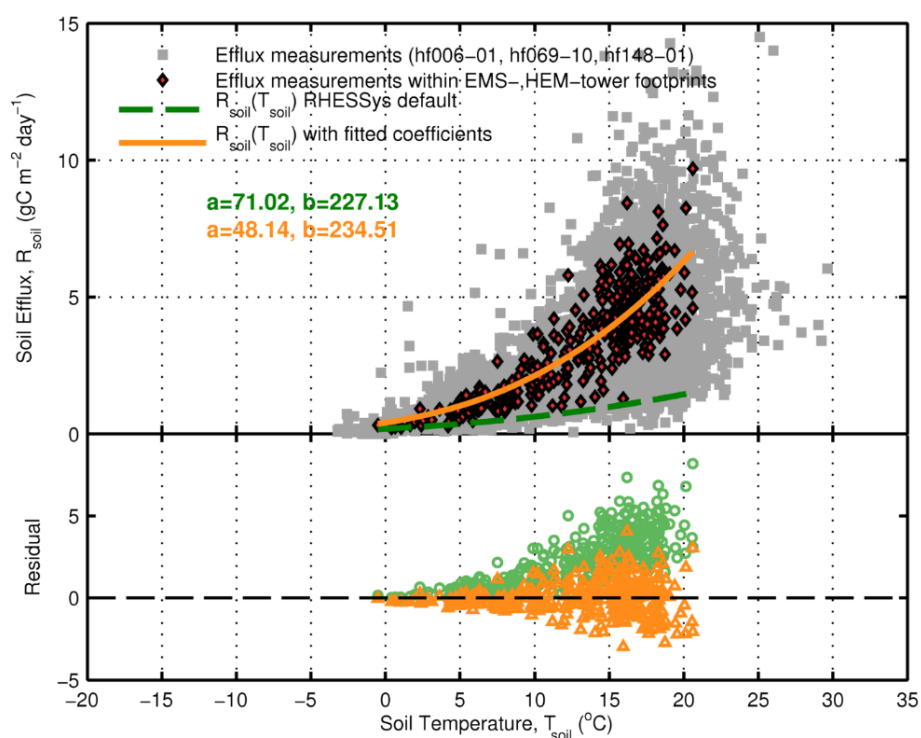


Figure 3.2. Estimation of soil decomposition-rate scaling. (Top panel) Dots indicate the field-measured soil efflux (gray squares: all available soil temperature and efflux data, red diamonds: data only within the towers' footprint). The green dash line is the RHESSys default function (with coefficients $a=71.02$, $b=227.13$) and the orange solid line is the modified function using the fitted coefficients ($a=48.14$, $b=234.51$). (Bottom panel) Residual plots of the default function (green squares) and modified function (yellow triangles).

Parameterization: initialization and calibration

The model parameters that specify the physical characteristics of the soil and the physiological characteristics of vegetation components were initialized with field measurements and previous studies (Tables 3.2 and 3.3). Since there is no consensus on the mathematical expressions to prescribe phenological timings (green-up, maturity, senescence, and dormancy), they were estimated as the timings when there were greatest changes in the curvature of logistic functions (Fisher et al., 2006; Zhang et al., 2003) fitted to the ground-based observations of leaf-sizes during spring and leaf-colorizations during autumn (Harvard LTER archive-ID: hf003-03 and hf003-04 : O'Keefe, 2000). Detail description is in Appendix. Based on the parameters, soil carbon and nitrogen storages were built up from the initial bare ground by spinning-up the system, assuming the current system is in the equilibrium state. It took about 500 years for this ecosystem to reach its equilibrium state. Vegetation carbon and nitrogen storages were initialized using the field-estimated LAI data in 2000 which was made for the purpose of validating MODIS land products (Cohen et al., 2006). LAI was converted to carbon and nitrogen storages in each component (leaf, root, stem, coarse root, live stem, and dead stem) of the vegetation depending on the biome type and its physiological characteristics, such as the specific leaf area (SLA), carbon and nitrogen ratios in each component, and carbon allocation strategy.

Table 3.2. Parameterization of soil components

Soil types	Sandy Loam	Wetland
Areal composition (% of basal area)		
in Bigelow-Brook catchment (BBC)	56.2ha (93%)	3.7ha (7%)
in Nelson-Brook catchment (NBC)	47.0ha (81%)	11.2ha (19%)
Physical properties		
Texture: fraction of sand-silt-clay (%)	65-25-10 ¹	20-65-15 ¹
Hydrological parameters		
Porosity at soil surface, ϕ_0 (range. 0 - 1)	0.435 ²	0.485 ³
Pore size index, p (unitless)	0.204 ²	0.589 ³
Air entry pressure, ψ_{ae} (meters of water)	0.218 ²	0.786 ³

¹ Soil Survey Geographic data set (SSURGO) from the Natural Resources Conservation Service (NRCS)

² Dingman, 2009

³ Yun et al. in Neponset catchment, MA (in preparation)

Table 3.3. Ecophysiological parameterization in the model

Vegetation types	Deciduous	Mixed	Coniferous
Class numbers in NLCD 2001 ¹	41	43	42
Physiological parameters			
Specific leaf area, <i>SLA</i> (m ² kgC ⁻¹)	18 ^{2,3,4}	17 ²	10 ^{2,5}
Fraction of N in Rubisco compared to total N in leaf, <i>FNLR</i> (kg kg ⁻¹)	0.088 ⁶	0.1 ²	0.1 ²
Leaf C:N ratio (kgC kgN ⁻¹)	21 ⁸	32 ⁹	42 ⁸
Litter C:N ratio (kgC kgN ⁻¹)	53 ⁸	80 ⁹	104 ⁸
Carbon allocation parameters (unitless) ²			
fine root : leaf	1.2	1.30	1.4
coarse root : stem	0.22	0.26	0.29
stem : leaf	2.2	2.20	2.2
live wood : total wood	0.16	0.116	0.071
Phenological timings			
Start days of green-up (DOY)	113-140 ¹⁰	113-140 ¹⁰	80 ⁷
Green-up length (days)	20-41 ¹⁰	20-41 ¹⁰	55 ⁷
Start days of senescence (DOY)	256-270 ¹⁰	256-270 ¹⁰	260 ⁷
Senescence length (days)	21-38 ¹⁰	21-38 ¹⁰	88 ⁷
Ecophysiological parameters			
<i>Q</i> ₁₀ for maintenance respiration (unitless) ¹¹	3.9	4	5.6
Stomatal conductance closure ²			
starts at leaf water potential (MPa)	-0.34	-0.495	-0.65
completes at leaf water potential (MPa)	-2.2	-2.350	-2.5
starts at VPD (Pa)	1100	800	0
completes at VPD (Pa)	3600	3350	3100

¹Detailed information about each class is available at [<http://www.mrlc.gov/>]

² White et al., 2000 ³ Waring et al., 1995 ⁴ Bartlett et al., 2011

⁵ Wythers et al., 2013 ⁶ estimated using *V*_{c,max} from Dillen et al., 2012

⁷ Yun et al. in Neponset catchment, MA (in preparation)

⁸ Harvard Forest LTER database HF069 (W. J. Munger et al., 1999)

⁹ Mean value of deciduous and coniferous.

¹⁰ Estimates using ground-based observation (HF003-03, HF003-04. O'Keefe, 2000).

Detail description is in Appendix

¹¹ Optimized values based on Chen et al. (2000), Davidson et al. (2006), Davidson & Savage (1999)

Physical properties of soils play a vital role in controlling hydrologic fluxes (e.g., infiltration, surface-runoff, drainage, capillary rise and subsurface-runoff) and storage (surface detention, soil moisture, and groundwater), and therefore they modulate the ecophysiological responses of the vegetation to the environment. In theory, soil-type-specific parameters (e.g. K_{sat0} and m in Eq. 3.7) are constants, however, those values exhibit significant spatial heterogeneity due to highly variable geologic formations such as unevenly distributed macro-pores and root-growth. To calibrate those intrinsically variable parameters with the observed streamflow data and to assess the uncertainty propagated through the process, the generalized likelihood uncertainty estimation (GLUE) methodology (Beven & Binley, 1992) was adapted for this study because of the following reasons; its relative ease of implementation which does not require major modifications to the model structure, lack of prior information about parameter distributions, and its parallel properties which significantly reduce computational time. Rejecting the idea of having one single optimized scenario, GLUE provides a behavioral range of the plausible scenarios, assuming “equifinality” in which different model structures and parameter sets would produce acceptable representation of the observed behavior (Beven & Freer, 2001). This range indicates the integrated uncertainties coming from the errors in the model structures and the parameters of the model and even in the observations for validation. The range is confined by the posterior likelihood of the simulation, $L(y|\theta_i)$, with the i -th parameter sets (θ_i) when

$$L(y|\theta_i) = L(\theta_i|y)L_o(\theta_i)/C \quad (3.11)$$

where $L(\theta_i|y)$ is the likelihood measure of the simulation with the i -th parameter sets and prior distribution, $L_o(\theta_i)$ is the prior distribution of the i -th parameter set (θ_i), and C is a scaling constant for normalization ($\sum_{i=1}^n L(\theta_i|y)/C = 1$). As mentioned above, due to the lack of prior knowledge of the parameter distributions and uncertainty of the parameters in the reality, initial distributions of the parameters were assumed as uniform within the given range (Table 3.4).

Table 3.4. List of parameters calibrated with GLUE method, their initial values and calibrating factor ranges.

Parameter	Initial value		Calibrating factor (Multiplier)
	Sandy loam	Wetland	
Vertical-flow Parameters			
Saturated hydraulic conductivity at the surface, K_{sat0}	3	0.0001	0 – 5
Decay rate of the hydraulic conductivity with depth, m	0.12	0.12	0 – 500
Lateral-flow Parameters			
Saturated hydraulic conductivity at the surface, $K_{sat0,v}$	3	0.0001	0 – 20
Decay rate of the hydraulic conductivity with depth, m_v	0.4	0.16	0 – 10
Explicit calibration factors			0 – 1
The fraction of water from the saturated store to the groundwater, gw_1			
The fraction of water from the groundwater to the streamflow, gw_2			

A total number of 3000 parameter sets (N=3000) was generated in a random way, known as *Monte Carlo* sampling method. Three years (October 2010-September 2013; water year 2011-2013) were chosen for calibration to include both wet and dry years (water year 2011: 1550 mm, water year 2012: 1064mm), so that the physical

characteristics of the soil can be calibrated to represent the soil moisture status in both wet and dry conditions. The Nash-Sutcliffe efficiency (referred to as “NSE” hereafter) of streamflow at a log-scale (base 10) was used (Eq. 3.12) as the likelihood measure because the baseflow represents the soil moisture status better than do peak-flows (to which linear-scale streamflow NSE values have a tendency of being sensitive).

$$\text{NSE}(\theta_i|\log(y)) = 1 - \left[\frac{\frac{1}{N} \sum_{t=1}^N \left(\log(y_t) - \log(Y_{\theta_i,t}) \right)^2}{\frac{1}{N} \sum_{t=1}^N \left(\log(y_t) - \overline{\log(y)} \right)^2} \right] \quad (3.12)$$

Where t is the time-point, N is the total number of the points, $Y_{\theta_i,t}$ is the model simulated with the i -th parameter set (θ_i) at the time t , y_t is the observation at the time t , and $\overline{\log(y)}$ is the mean value of log values of observation ($\overline{\log(y)} = \frac{1}{N} \sum_{t=1}^N \log(y_t)$). The maximum log-NSE values during growing season were 0.59 at BBC and 0.65 at NBC. Criteria for accepting simulations as behavioral scenarios were set to log-NSE 0.2 for BBC and 0.1 for NBC, and 95% uncertainty boundaries were accepted as the final confidence intervals to either reject over-conditioning (over-fitting to any single data) and under-conditioning models.

3.4. Result

3.4.1. *Parameter calibration and validation*

Most of the observed streamflow at both catchments lay within the 95% confidence intervals of the simulated streamflow at the monthly scale hydrograph (Figure 3.3). Winter snowpack (e.g. February and December in 2008) and early spring snow-melt (e.g. March in 2008 and 2009) caused high uncertainties (wide confidence intervals) and deviations in the simulated streamflow from the observations. Snow accumulation and melting processes are mainly controlled by temperature coefficients which are set to constants in the current version of RHESSys (ver. 5.15.333). Focusing on growing season (May-October) when the soil moisture modulates vegetation response to climate, mean values of the confidence intervals of simulated streamflow at the monthly scale showed a high agreement with the observations at both catchments (Figure 3.4). The maximum monthly log-NSE values during the growing season were 0.8 for calibration and 0.6 for validation at BBC and 0.52 for calibration and 0.53 for validation at NBC. At the annual scale, simulated streamflow explains about 80% variance of the observation but the total discharge was overestimated due to the overestimated snow-melt streamflow.

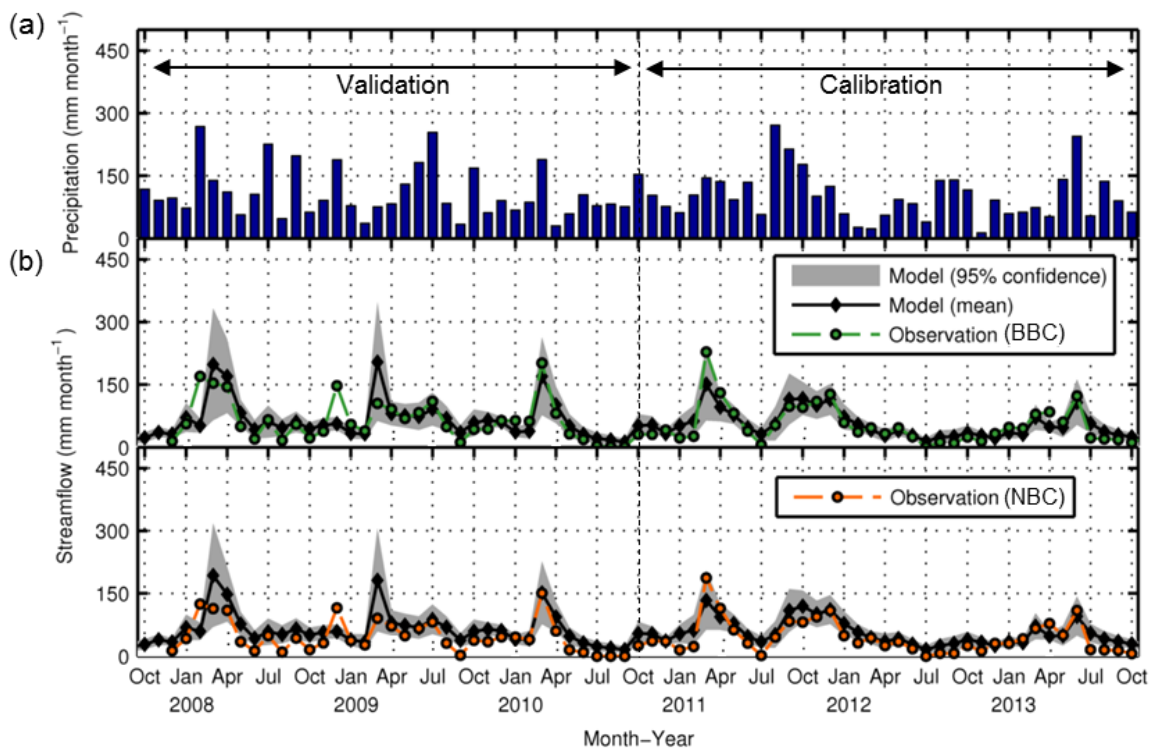


Figure 3.3. (a) Monthly precipitation. (b) Calibration and validation results with monthly streamflow discharge at BBC and NBC. Gray area indicates 95% confidence intervals estimated from GLUE method with the likelihood measure log-NSE. Black diamonds are the mean value of the confidence interval and circles are monthly-total streamflow discharge. Dash lines are the observed streamflow at BBC (green) and NBC (orange).

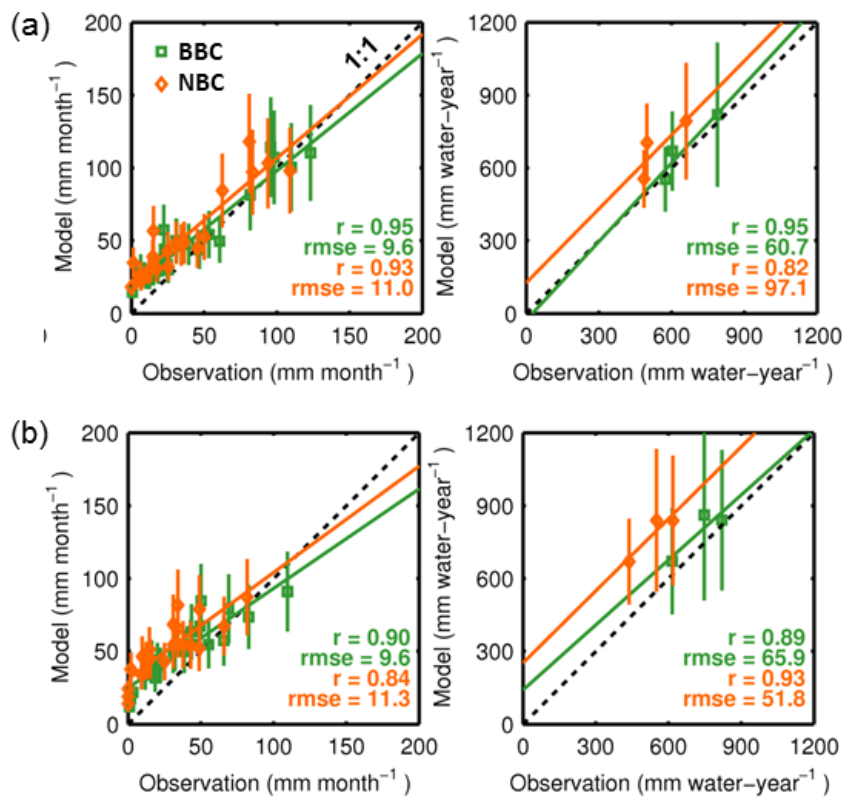


Figure 3.4. Scatter plots between observed and simulated streamflow at monthly, and annual scales at BBC (green) and NBC (orange) for (a) calibration and (b) validation periods. Monthly scatter plots evaluated streamflow during growing-season (May and October) when soil moisture modulates vegetation responses to the climate.

3.4.2. Below-ground processes at patch scale

Soil moisture

The simulated soil moisture represents averaged soil moisture in the root-zone from the ground surface to the simulated root-depth (70-80 cm), therefore it is not exactly comparable to the field observation measured at the shallow fixed depths (10-15 cm). In general, the simulated root-zone soil moisture at the EMS-patch followed the overall profile of the areal mean of the measurements, and the confidence intervals contained most of the measurements (Figure 3.5a). It also showed strong seasonality that gradually declines to 15-20% during the maturity season and recharges back to 32-35% throughout senescence and dormancy phases. Simulated root-zone soil moisture at HEM-patch tended to be fairly constant and high throughout the seasons, which accounts for the formation of the nearby wetland. Soil moisture is not only dependent on the precipitation quantity but also on the timing (Figure 3.5b). For example, annual total precipitation was almost identical in 1999 and 2000, but soil moisture dropped to 10% at the end of August 1999 while it was higher than 20% throughout the seasons in 2000. This was because the most of the precipitation in 1999 was concentrated in September, in contrast to more evenly distributed precipitation in 2000.

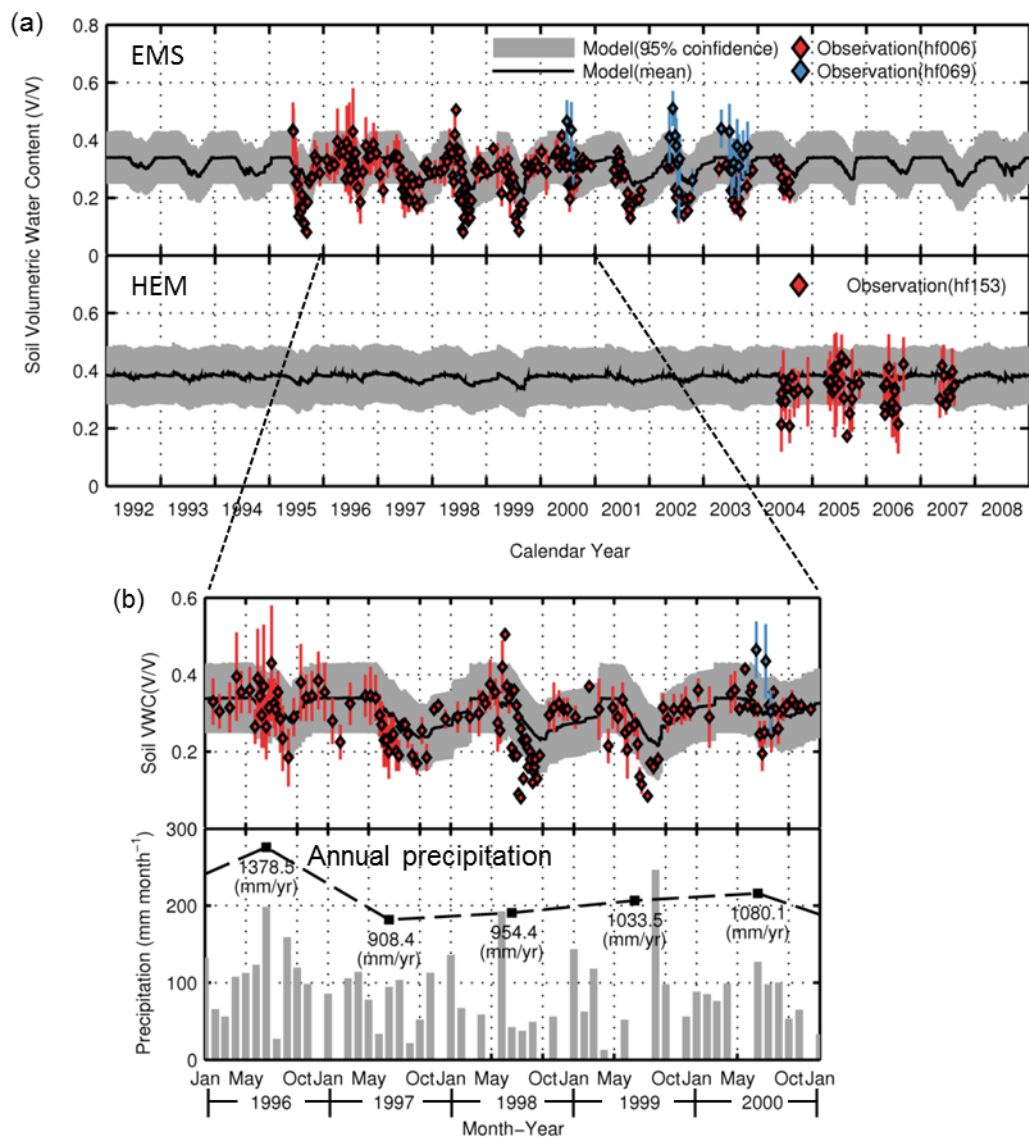


Figure 3.5. The time series of observed and simulated soil moisture values in the study sites. (a) Gray area indicates 95% confidence intervals of the soil moisture at the EMS-patch (top) and HEM-patch (bottom), respectively. Dots are the areal mean value of the observations within the footprints. Bar indicates standard deviation of the observations (b) Soil moisture of EMS-tower from 1996 to 2000 with the monthly and annual precipitation

Soil surface CO₂ efflux

Soil surface CO₂ efflux (here after “R_{soil}”) is one of the major carbon cycle fluxes, of up to 75GtC year⁻¹ at the global scale, and acts as a primary route for fixed carbon to return to the atmosphere (Schlesinger et al., 2000). Although it is the integrated flux of autotrophic (root and associated mycorrhizal) respiration and heterotrophic (microbial) respiration that are difficult to examined individually, the seasonal and interannual changes in R_{soil} can be a good indicator of belowground processes: plant metabolism such as carbon allocation to root and respiration from the root, and also response of soil microbes to the changing climate (Norby et al., 2000). Furthermore, the process of decomposing soil organic matter produces a by-product, nitrogen, most often limiting nutrient for plant growth (LeBauer et al., 2008).

Observed R_{soil} (Figure 3.6) showed strong seasonal and inter-annual changes but no long-term trend is noticeable. Mean R_{soil} during growing season was 4.96 gC m⁻² day⁻¹ at EMS-tower and 4.03 gC m⁻² day⁻¹ at HEM-tower, 18% lower than EMS-tower. Lower R_{soil} at coniferous forest compared to nearby broad-leaved forest on the same soil type under the same local climate was also reported from other studies by an average of 10% (Raich et al., n.d.). Dependence of R_{soil} on soil moisture and air temperature was noticeable. For example, mean air temperature between June and September in 1997 and 1998 was similar (14.1 °C in 1997 and 14.5 °C in 1998), but soil moisture in 1998 dropped below 10% (18% in 1997), resulting in higher R_{soil} at both the EMS and HEM towers in 1998 compared to 1997. Furthermore, soil moisture in 1995 and 1998 was

below 10%, but the lower mean temperature in 1995 (13.5 °C) might have induced the low R_{soil} in 1995.

The simulated R_{soil} values have a fair agreement with the observed R_{soil} ($r=0.75$ at the EMS-patch and $r=0.79$ at the HEM-patch. Figure 3.6), considering the substantial spatial heterogeneity and microscale variability along the 200-meter transects (Stoyan et al., 2000). Mean R_{soil} during growing season was $4.45 \text{ gC m}^{-2} \text{ day}^{-1}$ at EMS-patch and $4.14 \text{ gC m}^{-2} \text{ day}^{-1}$ at HEM-tower, 7% lower than EMS-tower. Strong peaks at the EMS-patch at the beginning of senescence were from the decomposition of the fallen leaves (litter), which might not have been included in the field measurements.

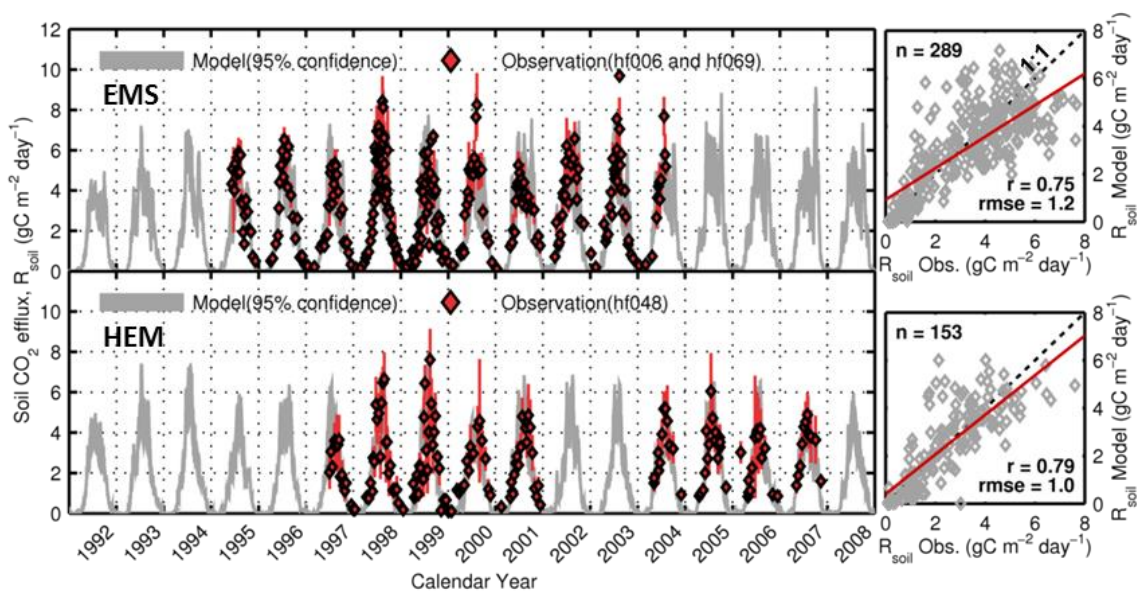


Figure 3.6. Soil respiration. Gray areas indicate 95% confidence intervals at the EMS-patch (left-top) and HEM-patch (left-bottom). Red diamonds are the areal mean values of the observations within the footprints. Bar indicates standard deviation of the observations. Scatter plot of model versus observation at EMS-patch (right-top) and HEM-patch (right-bottom).

3.4.3. Above-ground processes at canopy scale

Leaf area index (LAI)

Evaluating LAI results with independent observations is very important not only because it is the physical interface between the carbon and water cycles through stomatal responses, but also because it is the key vegetation compartment of the allocated carbon and nitrogen. Compared to other compartments of vegetation such as root or woody parts (stem and branch), it is also relatively easy to measure in the field. Simulated LAI values at the EMS-patch ranges about 5.5 ± 0.5 ($\text{m}^{-2} \text{m}^{-2}$) during growing season, while LAI at the HEM-patch is about 3.8 ± 0.2 (Figure 3.7). The overall seasonal profile was well described ($r=0.93$), but the maximum LAI at the EMS-patch is generally overestimated ($\text{rmse}=0.9$) while underestimated at the HEM-patch by 0.5. The prescribed growing season dynamics from the ground-observed leaf phenology tends to be later than the observed LAI leaf-out, as well as for early dormancy.

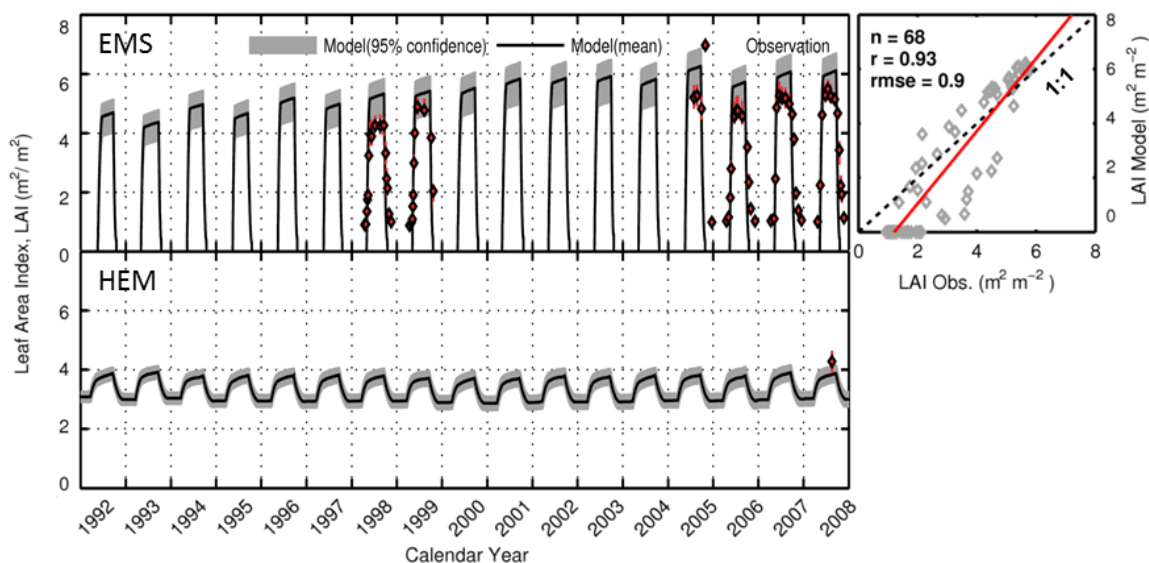


Figure 3.7. LAI simulation (Left-top) Gray area indicates 95% confidence intervals at the EMS-patch and HEM-patch (Left-bottom). Dots are the areal mean value of the observations within the footprints. Bar indicates standard deviation of the observations. (Right-top) Scatter plot between observed and simulated LAI at EMS-patch.

Gross primary productivity (GPP)

The observed GPP has gradually increased from 1992 to 2008, and there were differences in the magnitude of the increment between the seasons (Figure 3.8). The distribution of the number of days with GPP during spring-time (April-June) and autumn-time (September-November) exhibited a highly positively skewed distribution, and the spring-time distribution skewness has gradually increased over the study period while the autumn distribution did not reveal any noticeable changes. The peak rate of daily GPP during spring-time has increased by 56% (from $12.6 \text{ gC m}^{-2} \text{ day}^{-1}$ in 1992 to $19.6 \text{ gC m}^{-2} \text{ day}^{-1}$ in 2008), and seasonal total flux increased by 28% (from $393.5 \text{ gC m}^{-2} \text{ spring}^{-1}$ in 1992 to $503.9 \text{ gC m}^{-2} \text{ spring}^{-1}$ in 2008). In the meantime, both the autumn peak rate and

the total flux did not increase significantly (8% increment of peak rate from $8.8 \text{ gC m}^{-2} \text{ day}^{-1}$ in 1992 to $9.5 \text{ gC m}^{-2} \text{ day}^{-1}$ in 2008; 18% increment of seasonal total flux from $255 \text{ gC m}^{-2} \text{ fall}^{-1}$ in 1992 to $302 \text{ gC m}^{-2} \text{ fall}^{-1}$ in 2008). The summer-time (July-August) GPP showed the most significant and noticeable growth trend both in the peak rate (66% increment from $10.5 \text{ gC m}^{-2} \text{ day}^{-1}$ in 1992 to $17.4 \text{ gC m}^{-2} \text{ day}^{-1}$ in 2008) and in the total flux (56% increment from $502 \text{ gC m}^{-2} \text{ summer}^{-1}$ in 1992 to $781 \text{ gC m}^{-2} \text{ summer}^{-1}$ in 2008). The number of days distribution had a negative skewness with a high degree of peaks in 1992, and gradually changed to a plateau distribution (a bimodal distribution) that indicates multiple processes are acting at a similar significance.

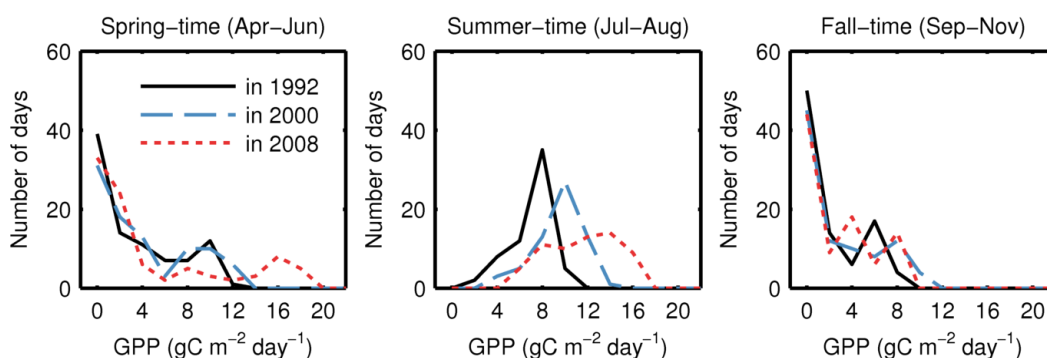


Figure 3.8. Distribution of number of days of the observed GPP during spring-time, summer-time, and fall-time in 1992, 2000, and 2008

The simulated GPP at the EMS-patch was compared to the observed GPP at the EMS tower at both daily scales (Figure 3.9a) and monthly scales (Figure 3.9b). Simulated GPP at the EMS-patch showed gradually increasing trends during the study period both in magnitude and quantity. Spring-time peak rate was simulated as $11.8 \text{ gC m}^{-2} \text{ day}^{-1}$ in 1992 and rose to $16.5 \text{ gC m}^{-2} \text{ day}^{-1}$ in 2008 (40% increment), while total flux increased

from $312 \text{ gC m}^{-2} \text{ spring}^{-1}$ in 1992 to $504 \text{ gC m}^{-2} \text{ spring}^{-1}$ in 2008 (61% increment). Summer-time peak rate has increased from $12.7 \text{ gC m}^{-2} \text{ day}^{-1}$ in 1992 to $16.4 \text{ gC m}^{-2} \text{ day}^{-1}$ in 2008 (30% increment), and total flux from $572 \text{ gC m}^{-2} \text{ summer}^{-1}$ in 1992 to $760 \text{ gC m}^{-2} \text{ summer}^{-1}$ in 2008 (34% increment). Fall-time peak rate has increased from $10.2 \text{ gC m}^{-2} \text{ day}^{-1}$ in 1992 to $14.2 \text{ gC m}^{-2} \text{ day}^{-1}$ in 2008 (40% increment), and total flux from $253 \text{ gC m}^{-2} \text{ fall}^{-1}$ in 1992 to $340 \text{ gC m}^{-2} \text{ fall}^{-1}$ in 2008 (34% increment). The narrow width of the confidence interval compared to the wide confidence interval of the simulated soil moisture indicates soil moisture does not play a significant role on regulating carbon uptake in the study area, which is an area primarily not under water-stress (Urbanski et al., 2007). High frequency (daily scale) reductions in GPP in the middle of the maturity seasons were well captured as shown in the daily scale plot. The prescribed phenological timings were mostly consistent with the timings of the green-up and dormancy GPP flux data, except for the significant difference of green-up timing in 2007.

The simulated GPP showed a high capability in capturing the intensity and the pattern of the GPP at EMS for seventeen years both at the daily and monthly scales (Figure 3.10a; $r=0.93$ at daily scale and $r=0.98$ at monthly scale). Model performance was stable throughout the study period without either an improving or deteriorating tendency in the performance over the whole study period (Figure 3.10b; $r=0.94$ between 1992 and 1995; $r=0.94$ between 1996 and 1999; $r=0.93$ between 2000 and 2003; $r=0.93$ between 2004 and 2008).

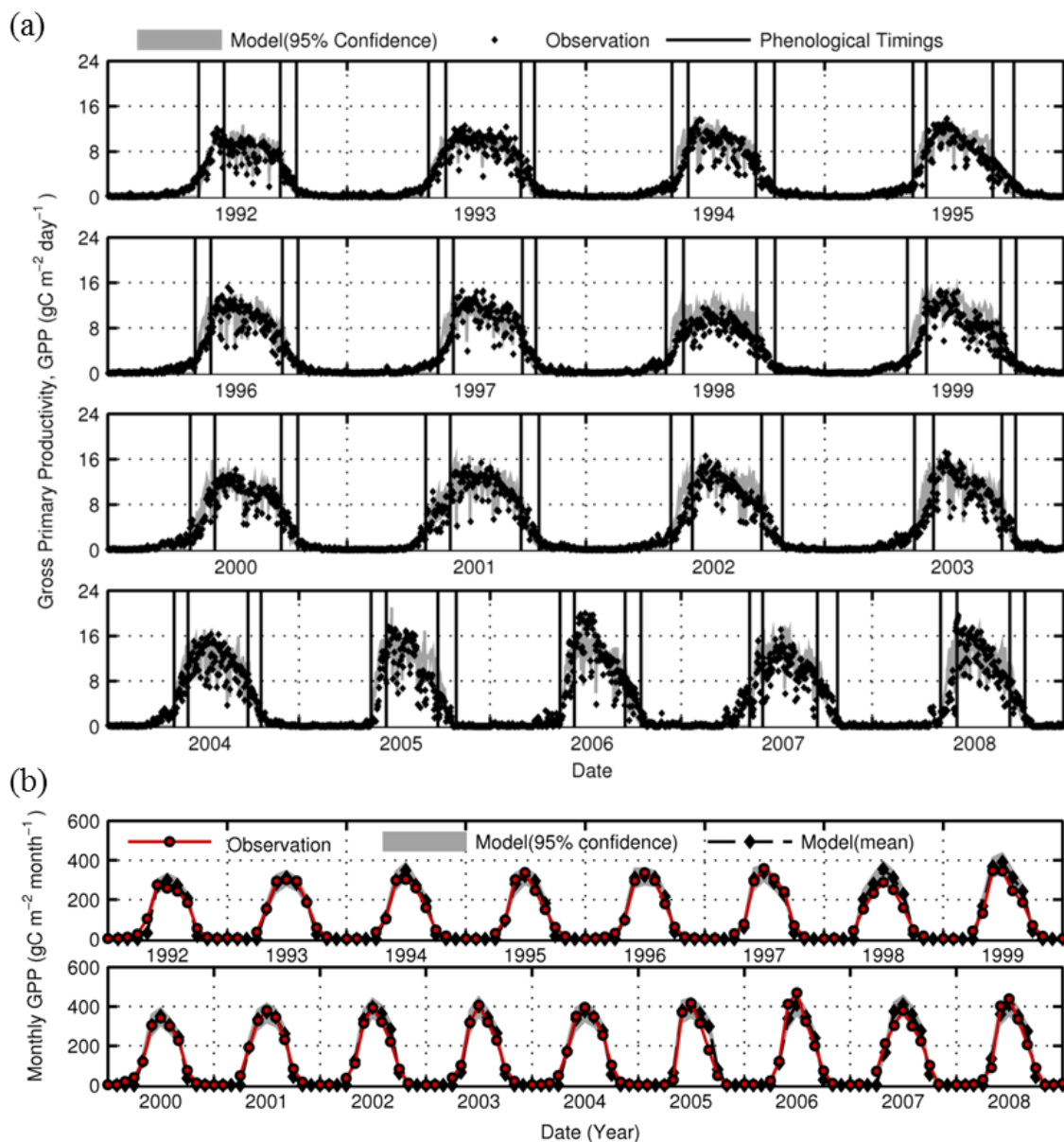


Figure 3.9. GPP simulation at EMS-patch (a) Daily scale temporal plot. Gray area indicates 95% confidence intervals. Dots are GPP at EMS-tower. Vertical lines are the prescribed phenological timings (growing-up, maturity, senescence, and dormancy) (b) Monthly scale temporal plot. Black diamond represents mean of the 95% confidence interval, and red circle indicates monthly-total GPP at EMS-tower.

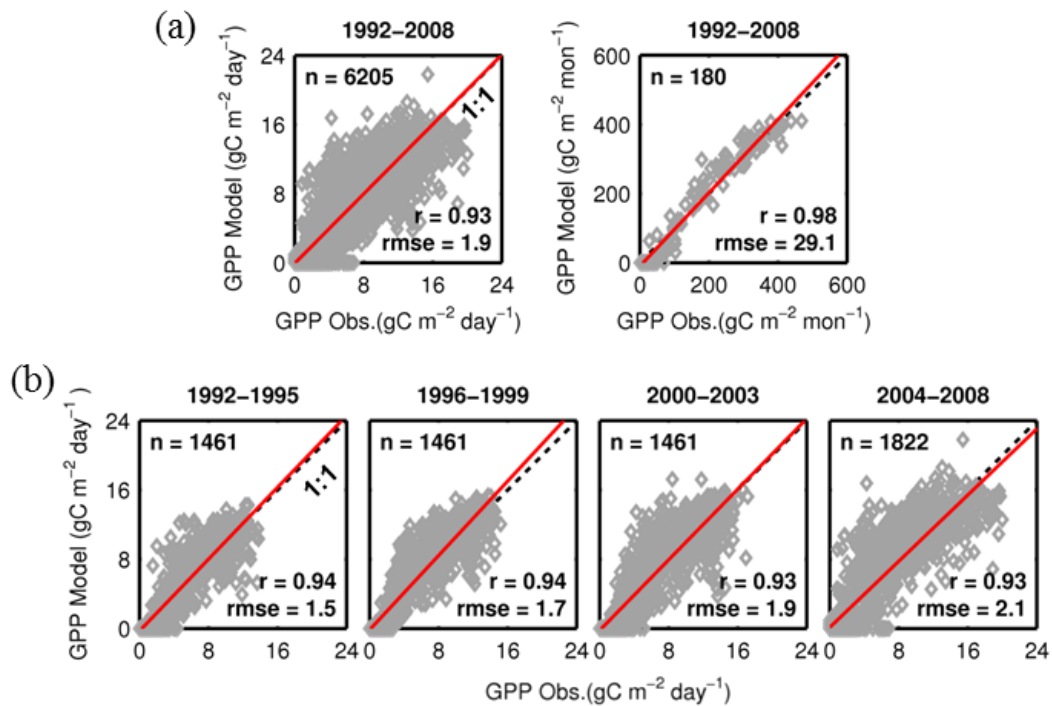


Figure 3.10. GPP simulation scatter plots of model versus observation (a) during the entire study period at daily and monthly scales (b) during the subdivided periods with the least square regression line in solid red

The average carbon uptake at the HEM-patch (Figure 3.11) during the growing-seasons (July-September) between 2004 and 2008 was simulated as $6.0 \text{ gC m}^{-2} \text{ day}^{-1}$, while observed as $5.9 \text{ gC m}^{-2} \text{ day}^{-1}$. In 2006, GPP was observed as $10.9 \text{ gC m}^{-2} \text{ day}^{-1}$, while simulated GPP is $9.7 \text{ gC m}^{-2} \text{ day}^{-1}$. There are limited amount of GPP data available at HEM site, but the simulated GPP showed high agreement with the observed GPP at the HEM-tower ($r=0.89$).

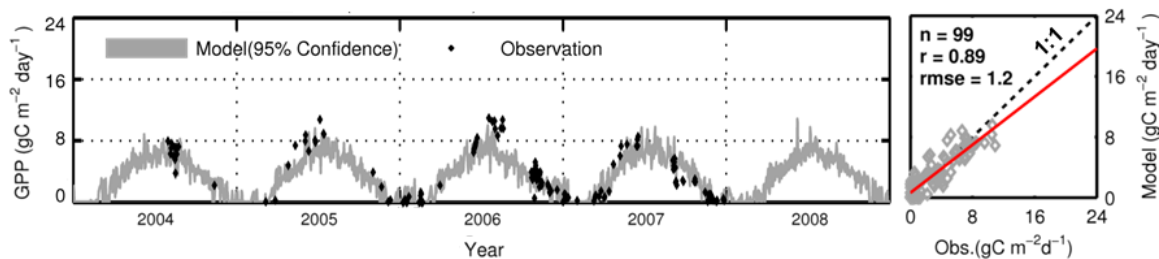


Figure 3.11. GPP simulation at HEM-patch. (left) Daily scale temporal plot. Gray area indicates 95% confidence intervals. Dots are GPP at HEM-tower (right) scatter plot of model versus observation daily scale with the least square regression line in solid red.

Evapotranspiration (ET)

The simulated ET profile at the EMS-patch generally followed the simulated GPP profile (Figure 3.12a), which indicates strong coupling between carbon and water exchanges under the control of stomata. The peak rate of the simulated ET in July 2004 was 5.6 mm day^{-1} and monthly mean rate was 4.25 mm day^{-1} . Hadley *et al.* (2008) took the weekly mean value of the daily LPH-tower measurements, and estimated the peak rate from the red oak forest as 4.3 mm day^{-1} ($\sigma=0.7 \text{ mm day}^{-1}$) in July 2004 that is comparable to the monthly mean rate of the simulated ET. Strong evaporative fluxes during winter and early spring in 1996, 1997 and 2008 were not well represented in the simulation. The simulated ET was not able to be evaluated at longer timescales (monthly, seasonal, and annual scales) because of the unevenly distributed gaps. Overall performance at the daily timescale is generally acceptable ($r=0.90$ in Figure 3.12b), showing neither improving or worsening performances over the whole study period (Figure 3.12c; $r=0.89$ between 1992 to 1995; $r=0.93$ between 1996 to 1999; $r=0.9$ between 2000 to 2003; $r=0.87$ from 2004 to 2008). The increment trend in the seasonal ET from 1992 to 2008 was different from the trend in GPP (Figure 3.13). Peak rate values during all seasons did not show any significant growth. Mean rate during spring and summer times has increased significantly between 2000 and 2008.

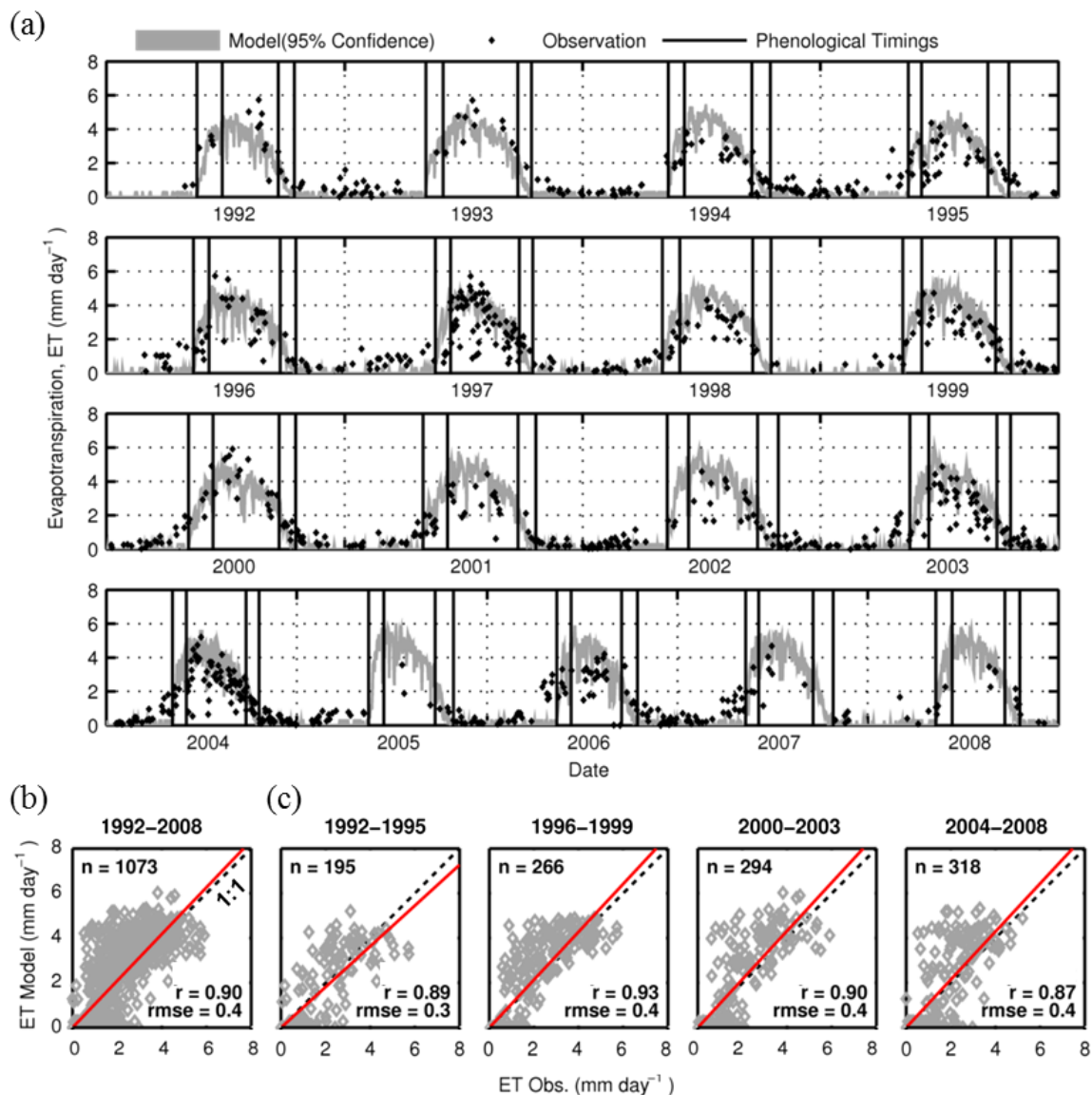


Figure 3.12. ET simulation at EMS-patch (a) Daily scale temporal plot. Gray area indicates 95% confidence intervals. Dots are water vapor flux measured at EMS-tower. Vertical lines are the prescribed phenological timings (growing-up, maturity, senescence, and dormancy) Scatter plots of model versus observation with the least square regression line in solid red (b) during the entire study period (c) during the subdivided periods

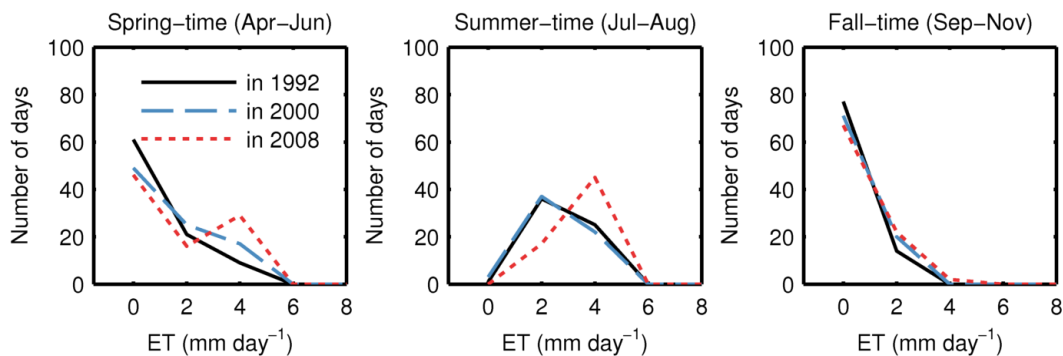


Figure 3.13. Distribution of number of days of the simulated ET during spring-time, summer-time, and fall-time in 1992, 2000, and 2008

Simulated ET at the HEM-patch showed a good correlation with the observed ET ($r=0.88$; Figure 3.14). Simulated ET at HEM-patch has wider confidence boundaries compared to EMS-patch, which implies that hemlock forest is more sensitive to the soil moisture status than red-oak stands. Simulated evaporative flux during dormancy seasons is noticeably higher than simulated ET at the EMS-patch. The peak rate of the simulated ET in July 2004 was 4.4 mm day^{-1} and monthly mean rate was $3.0 \pm 0.03 \text{ mm day}^{-1}$, which is 30% higher than $2.3 \pm 0.5 \text{ mm day}^{-1}$ estimated by Hadley et al. (2008) that took weekly mean value of the daily HEM-tower measurements in the period.

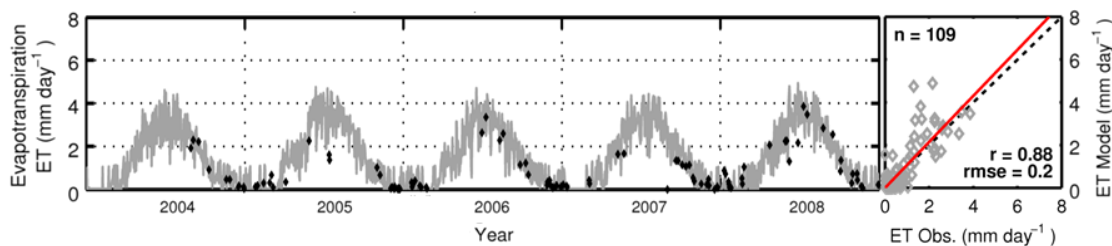


Figure 3.14. ET simulation at HEM-patch (left) Daily scale temporal plot. Gray area indicates 95% confidence intervals. Dots are water vapor flux measured at HEM-tower. (right) scatter plot of model versus observation daily scale with the least square regression line in solid red.

3.4.4. Annual magnitudes and long-term trends of carbon and water fluxes

At canopy scale

Simulated annual GPP and ET fluxes at EMS and HEM patches were presented along with the observed annual GPP at EMS-tower and the basal area increments depending on the footprint-dominant vegetation type (deciduous trees for EMS-patch and coniferous trees for HEM-patch) (Figure 3.15). Long-term trends were estimated using the nonparametric Spearman Rho's test (H_0 : null hypothesis-all the data in the time period are independent and identically distributed ; H_1 : alternative hypothesis-increasing or decreasing trends exist in the data in the time period) at the 5% significant level. Trends, coefficients, and significances are summarized in Table (3.5).

The simulated annual GPP showed high agreement with the observed GPP in the respect to correlation ($r=0.78$ and $rmse=109.7 \text{ gC m}^{-2} \text{ year}^{-1}$ in Figure 3.15) as well as with respect to increasing trends. The observed annual GPP at the EMS-tower has increased significantly over the study period from $1170 \text{ gC m}^{-2} \text{ year}^{-1}$ in 1992 to $1600 \text{ gC m}^{-2} \text{ year}^{-1}$ (about $+27 \text{ gC m}^{-2} \text{ year}^{-1}$ per year). The simulated annual GPP captured the increasing rate, $+30.2 \text{ gC m}^{-2} \text{ year}^{-1}$ per year, from $1140 \text{ gC m}^{-2} \text{ year}^{-1}$ in 1992 to $1620 \text{ gC m}^{-2} \text{ year}^{-1}$ in 2008 (Figure 3.16). Mean GPP flux during the study period was $1410 \text{ gC m}^{-2} \text{ year}^{-1}$ ($\sigma= 165 \text{ gC m}^{-2} \text{ year}^{-1}$). The observed GPP deviated from its own growth trend in years 1993, 1998, 2001, 2004, and 2005 (called “anomalies” in this study). It is noticeable that the simulated GPP does not account for the negative GPP anomalies in 1998 and 2005, but it did simulate the full magnitude of the positive anomaly in 2001 and half magnitude of the positive anomaly in 2004. The model also overestimated carbon

uptake in the normal years (1999 and 2002) by 15%. The observed BAI of deciduous trees also showed an increasing trend between 1999 and 2008 at a significant level ($+1.63 \text{ cm}^2 \text{ year}^{-1}$ per year). In 2006, BAI dropped to $4.1 \text{ cm}^2 \text{ year}^{-1}$ due to the significantly decreased GPP in 2005, showing the one-year lagged effect of the fixed carbon at the leaf level being allocated to the aboveground woody biomass. Simulated ET at the EMS-patch has also increased at a small but significant rate ($+6.77 \text{ mm year}^{-1}$ per year). Mean ET flux during the study period was 516 mm year^{-1} ($\sigma = 47 \text{ mm year}^{-1}$).

The simulated annual GPP at the HEM-patch has increased over the seventeen years from $985 \text{ gC m}^{-2} \text{ year}^{-1}$ in 1992 to $1030 \text{ gC m}^{-2} \text{ year}^{-1}$ in 2008 at an increasing rate ($+5.8 \text{ gC m}^{-2} \text{ year}^{-1}$ per year) that is smaller compared to EMS-patch, but the increasing trend was statistically significant. Mean GPP flux during the study period was $1020 \text{ gC m}^{-2} \text{ year}^{-1}$ ($\sigma = 50 \text{ gC m}^{-2} \text{ year}^{-1}$). The increasing trend of the observed BAI of coniferous trees ($+0.79 \text{ cm}^2 \text{ year}^{-1}$ per year) was almost half that of the deciduous trees and the trend was also significant ($p < 0.01$). Simulated ET showed a significantly increasing trend at a small rate ($+3.87 \text{ mm year}^{-1}$ per year) with weak linearity ($r = 0.56$). Mean ET flux during the study period was 502 mm year^{-1} ($\sigma = 35 \text{ mm year}^{-1}$).

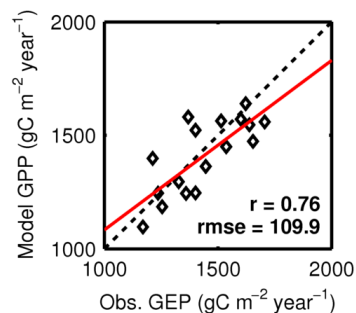


Figure 3.15. Scatter plot and regression analysis of (a) observed annual GPP at EMS-tower versus simulated annual GPP at EMS-patch

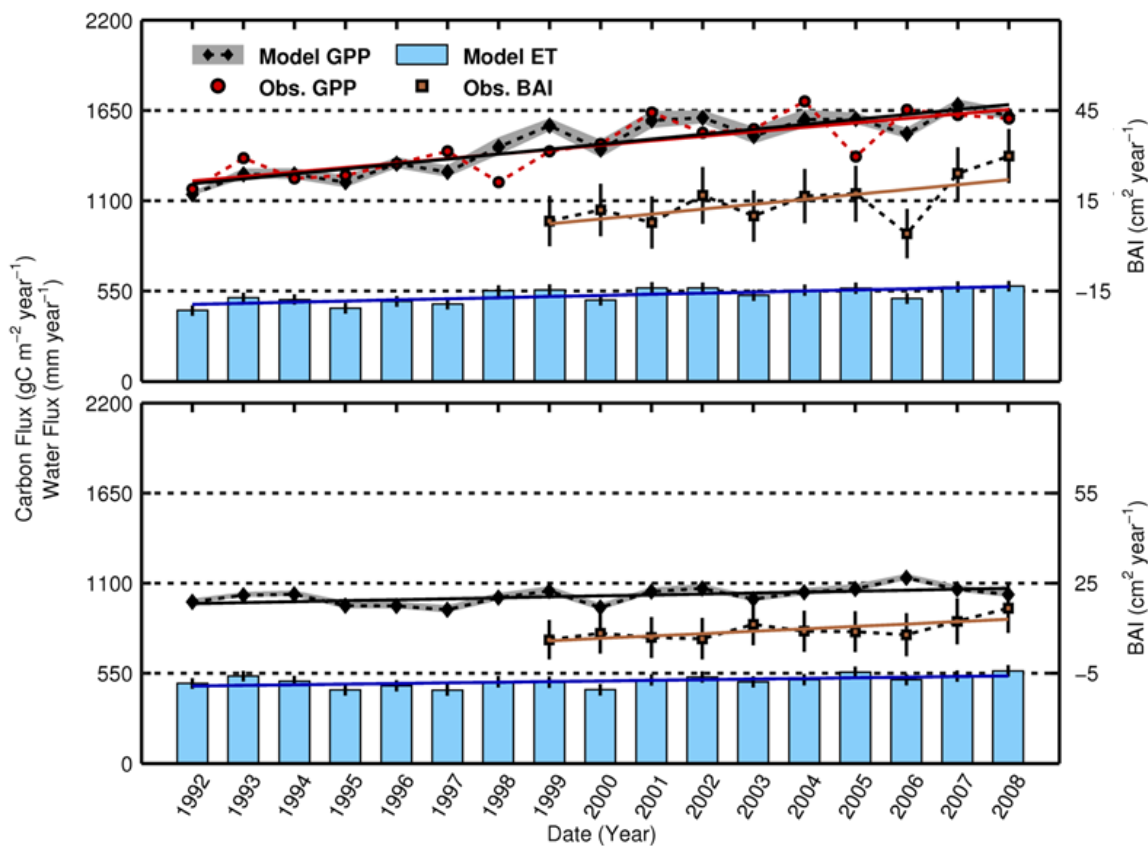


Figure 3.16. Annual flux and long-term trends in annual GPP, ET and basal area increment at (top) EMS-patch and (bottom) HEM-patch. Black dots are the means of 95% confidence intervals (gray area) of simulated GPP, red circles are annual GPP at EMS-tower. Brown squares are basal area increments. Light-blue bars are simulated ET. Vertical lines are 95% confidence intervals of ET. Solid lines are the regression lines estimated using Spearman Rho's test (slopes, correlation coefficients, and significances are summarized in Table 3.5)

At catchment scale

The simulated water fluxes (ET and streamflow) at the catchment scales were evaluated using the precipitation measurements. At both catchments, the sum of the simulated fluxes showed good agreement with the precipitation amounts ($r=0.89$ at BBC and $r=0.87$ at NBC in Figure 3.17), indicating that the annual total water mass was well balanced at both catchments.

At BBC (Figure 3.18a), the simulated annual GPP has increased over the seventeen years by 27% (from $907 \text{ gC m}^{-2} \text{ year}^{-1}$ in 1992 to $1152 \text{ gC m}^{-2} \text{ year}^{-1}$ in 2008) at a rate ($+15.71 \text{ gC m}^{-2} \text{ year}^{-1}$ per year) showing significant and linear trend ($p<0.0001$; $r=0.88$). The simulated ET also exhibited significant and linear increasing trend as well ($+5.68 \text{ mm year}^{-1}$ per year; $p<0.01$; $r=0.7$). At NBC (Figure 3.18b), the simulated annual GPP has increased over the seventeen years by 27% (from $843 \text{ gC m}^{-2} \text{ year}^{-1}$ in 1992 to $1193 \text{ gC m}^{-2} \text{ year}^{-1}$ in 2008) at a rate ($+22.12 \text{ gC m}^{-2} \text{ year}^{-1}$ per year) showing significant and linear trend ($p<0.0001$; $r=0.91$). The simulated ET also exhibited a significant and linear increasing trend as well ($+8.71 \text{ mm year}^{-1}$ per year; $p<0.0001$; $r=0.84$)

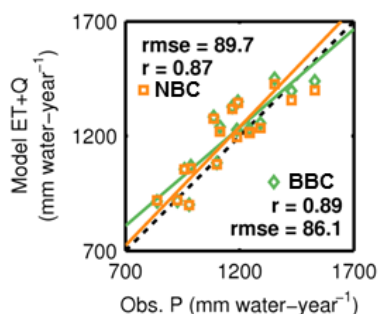


Figure 3.17. Scatter plots and regression analysis of the observed precipitation in the water years versus the sum of simulated ET and streamflow in BBC (green dots and lines) and in NBC (orange dots and lines)

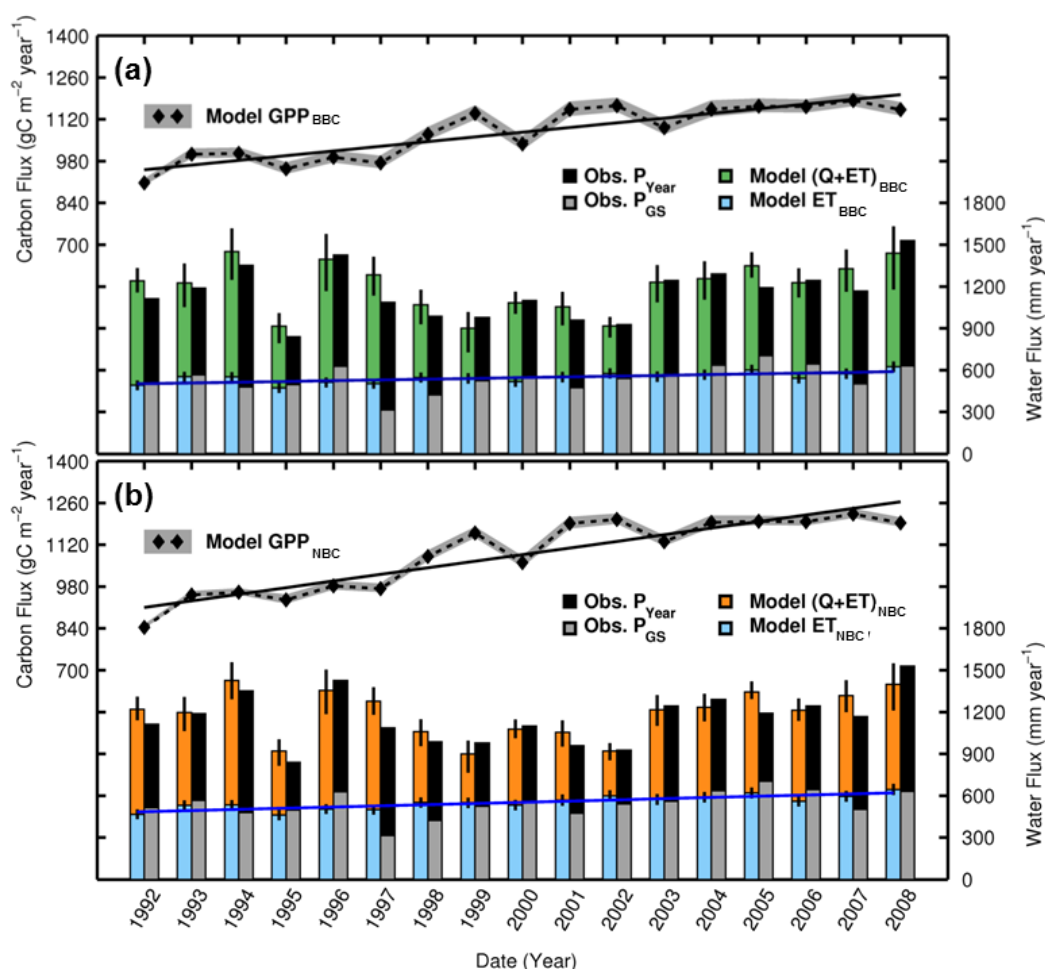


Figure 3.18. Long-term trends of catchment-scale GPP and ET at (a) BBC and (b) NBC. Black dots are the means of 95% confidence intervals (gray area) of simulated GPP. Light-blue bars are simulated ET, and streamflow is expressed in green bars (BBC) and orange bars (NBC). Vertical lines are 95% confidence intervals of simulated streamflow and ET. Solid lines are the regression line estimated using Spearman Rho's test (slopes, correlation coefficients, and significances are summarized in Table 3.5)

Table 3.5. Long-term trends in annual fluxes from 1992 to 2008 at patch scales and catchment scales

Field data based estimations	EMS-tower	HEM-tower		
GPP (gC m ⁻² year ⁻¹ per year)	+27.24*** (0.81)	NaN	regression slope (correlation coefficient)	
Basal area increment from 1999 to 2008 (cm ² year ⁻¹ per year)	+1.63* (0.62)	+0.79** (0.75)		
Simulated fluxes	EMS-patch	HEM-patch	BBC	NBC
GPP (gC m ⁻² year ⁻¹ per year)	+30.20*** (0.90)	+5.80* (0.58)	+15.71*** (0.88)	+22.12*** (0.91)
ET (mm year ⁻¹ per year)	+6.77** (0.73)	+3.87** (0.56)	+5.68** (0.70)	+8.71*** (0.84)

Significance (p-value): ***p<0.0001 **p<0.01 *p<0.05

3.5. Discussion and conclusion

In this study, we simulated the carbon and water cycles in the Harvard Forest using a spatially-distributed process-based ecohydrological model (RHESSys), which was applied to a mixed forest ecosystem in the northeastern United States for the first time. The performance of RHESSys at different spatio-temporal scales, from daily to annual time scale and from plot-scale to catchment scale, was validated for the two major forest types separately (deciduous forest and coniferous forest) and also for two mixed forest catchments during the study period of 17 years (1992-2008). The validation data included quantitative and qualitative data that has been collected in support of Harvard Forest's role as a Long Term Ecological Research (LTER) site: these include catchment

streamflow data, soil moisture and respiration measurements, LAI measurements, and GPP and ET flux data.

In the study area, the carbon uptake by predominantly deciduous forests (represented as the EMS-patch in the result) is much more variable as compared with coniferous forests (represented as the HEM-patch in the result). The deciduous forests had higher carbon uptake and variability (Figure 3.19), along with a six times higher increasing trend (Table 3.5). The GPP increment of the deciduous forests at the study site is considerably higher for the mid-successional (70-100 years-old) temperate deciduous forests that have already passed their initial rapid growth period (Ryan et al., 1997). However, this acceleration of gross productivity might be explained by the metabolic scaling theory that mass growth rate would increase continuously as tree grows (Enquist et al., 1999). Aboveground woody biomass of red oaks at the Harvard Forest is mostly between 0.1Mg and 1Mg (estimated from the DBH measurements and the allometric equation: Harvard Forest LTER archive ID: hf069-15. Munger & Wofsy, 1999), which is the critical mass range at which the rapid increase in growth rate starts (Stephenson et al., 2014). This could imply that the carbon update by the deciduous forests at the Harvard Forest may now start to increase significantly as the old trees gain more mass if there is no external factor causing mortality.

The behaviors of the water fluxes from deciduous and coniferous forests are different from the carbon fluxes (Figure 3.19). The flux from the deciduous forest was slightly higher, 14 mm year⁻¹ in average, compared to the coniferous forest (mean ET between 1992 to 2008: 516 mm year⁻¹ at the EMS-patch, 502 mm year⁻¹ at the HEM-

patch, 535 mm year^{-1} at BBC, and 524 mm year^{-1} at NBC) with a very small increment over the study period (Table 3.5). The interannual variation ($\sigma = 47 \text{ mm year}^{-1}$ at the deciduous forest; $\sigma = 35 \text{ mm year}^{-1}$ at the coniferous forest) was small compared to the interannual variations in precipitation ($\sigma = 185 \text{ mm}$). This confirms the concept of the “conservative” pattern of the ET flux in that the magnitude of decrease in ET due to water-stress during dry years is comparable to the amount of decrease in ET by other-resource-stresses in non-dry years at a canopy-level (Stoy et al., 2006; Oishi et al., 2010). For example, limited-light and lower-temperature due to the increased number of cloudy-days during growing season would result in an annual ET conservative at an annual scale. This conservative behavior was also reported in other temperate broadleaf forests (Stoy et al., 2006; Oishi et al., 2010). For example, even though there was a significant reduction in GPP in 2005 when the growing-season precipitation was largest during the study period, the annual ET remained at the mean level, showing the conservative behavior of the forest. These conservative water fluxes from both forests, as a result, resulted in an annual streamflow highly correlated with the precipitation ($r = 0.83$ at BBC, $r = 0.78$ at NBC; Figure 3.20).

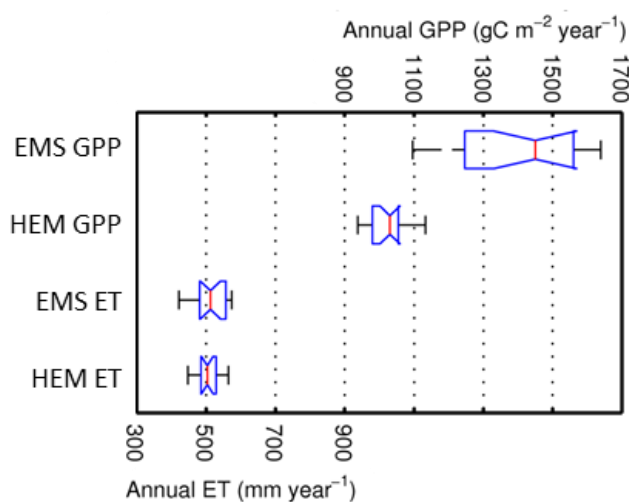


Figure 3.19. Annual GPP and ET from 1992 to 2008 at EMS-patch and HEM-patch

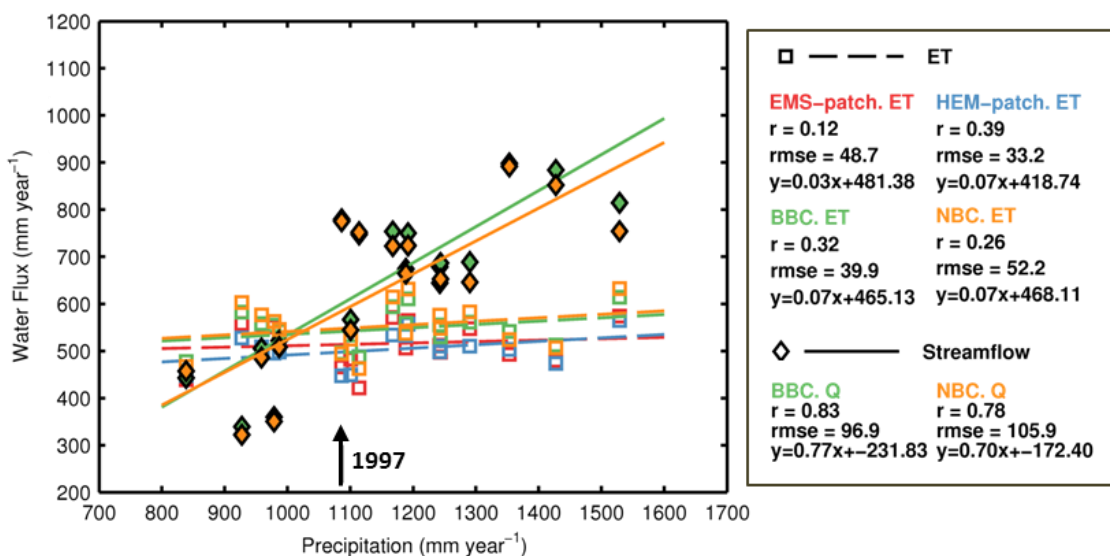


Figure 3.20. Scatter plot and regression analysis of observed annual precipitation versus simulated annual ET at both patches and catchments. Spatial scales (patches and catchments) are distinguished by color, and fluxes by symbol.

In this mesic forest, it is hard to assess the impact of drought on the carbon and water cycles. The water use efficiency of coniferous forests, $1.01 \text{ gC kgH}_2\text{O}^{-1}$, might

indicate that the carbon uptake by coniferous forests in the study area would be more sensitive to drought events. Mean water use efficiency (slope of the linear regression in Figure 3.21) of deciduous forests over the study period was $3.2 \text{ gC kgH}_2\text{O}^{-1}$ that falls in the range of the inherent water efficiencies between 1992 and 2010 estimated only using tower flux and VPD measurements ($20\text{-}50 \text{ gC kgH}_2\text{O}^{-1} \text{ hPa}$; Keenan *et al.*, 2013; VPD during growing season is about 10 hPa). Mean water use efficiency of coniferous forests for the same period was $1.01 \text{ gC kgH}_2\text{O}^{-1}$ that is smaller than $30 \text{ gC kgH}_2\text{O}^{-1} \text{ hPa}$ between 2005 and 2010 (Keenan *et al.*, 2013).

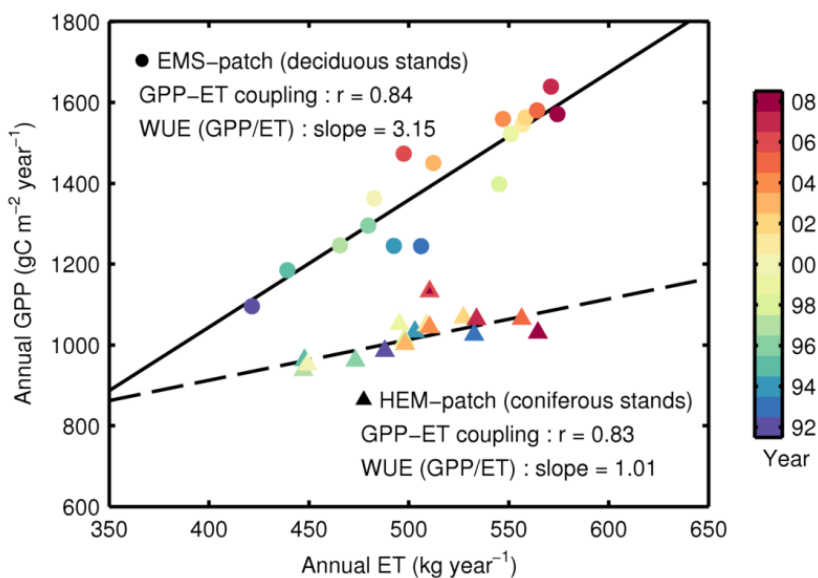


Figure 3.21. Scatter plots and regression analysis of annual GPP compared to annual ET at EMS-patch (colored circle) and HEM patch (colored triangle). Each year is colored in unique color.

It should be noted that there are a number of uncertainties that this study might not be fully accounted for. One of the critical inputs, precipitation, contains significant uncertainty in quantity as well as quality (snow or rain). Depending on the type of gauge,

up to 40% of the snow fall could be not measured at a wind speed of $2.5 \text{ m second}^{-1}$ (Yang et al., 1998). Snow amount determines soil moisture as well as soil temperature in the early spring, controlling springtime vegetation physiology. More analysis should be undertaken about the effect of uncertainties in the snow observations on the modeling result.

The uncertainties in the field-measured data should also be considered for a fair evaluation on the model performance. It is inevitable for field-data to have a wide-range of uncertainties that can be even as large as the order of the data. Tower- measured NEE with the eddy-covariance method can have uncertainties as high as $\pm 50\%$ of the measured flux or even larger (Keenan et al., 2011). The tendency of these uncertainties is heteroscedastic (increasing magnitudes when the flux magnitude increases) rather than constant, and also varies over time (Richardson et al., 2008). Water (energy) fluxes are also subject to significant uncertainties as well. Hollinger and Richardson (2005) stated that the stochastic nature of turbulence could induce 20% of uncertainty in latent heat flux and 20% in sensible flux.

This study only calibrated hydrological variables, adapting physiological parameters from previous studies and field measurements. Although inherent uncertainties in the hydrological variables were represented as the confidence intervals, extensive and robust tests about the uncertainties in the other parameters and model sensitivity to those parameters should be followed as more field-data becomes available for future research.

APPENDIX

Phenological timing estimation

Ground-based visual observation data was adapted to append phenological indices to the developmental stage of the northern hardwood forest : leaf-sizes during spring and leaf-colorizations during autumn from 1992 to 2008 (Harvard LTER archive-ID: hf003-03 and hf003-04 : O’Keefe, 2000.) The percentage size of leaves of three dominant species, northern red oak (*Quercus rubra L.*), red maple (*Acer rubrum L.*) and yellow birch (*Betula alleghaniensis L.*), relative to their final size (hf003-03.LFIN) was converted into spring phenological index from 0 to 1, and the percentage of discolored-leaves on the same tree (hf003-04.LCOLOR) was converted into autumn phenological index from 1 to 0.

A piecewise logistic function (Eq. A3.1) was adapted to build a phenology model describing the temporal pattern of the spring and phenological indices of the individual year (Zhang et al., 2003).

$$\begin{aligned}
 I(t) &= [I_1(t), I_2(t)] \\
 &= [(\frac{c_1}{1+e^{a_1+t \cdot b_1}} + d_1), (\frac{c_2}{1+e^{a_2+t \cdot b_2}} + d_2)] \quad (A3.1)
 \end{aligned}$$

where t is the day of year (DOY) in spring and autumn of each year, a_1 and b_1 are the fitting coefficients for spring phenology model (I_1) and a_2 and b_2 are the fitting coefficients for the autumn phenology model (I_2) for the year. The constants, c_1 and c_2 , decide the amplitudes and the slopes of the model, and d_1 and d_2 are the minimum phenological indices (therefore, $c_1=1$, $c_2=-1$, $d_1=d_2=0$ by the definition of the

phenological index in this study). The fitting coefficients (a_1 , a_2 , b_1 and b_2) were estimated using the nonlinear regression function, *nlinfit*, in Matlab (Matlab R2013a, MathWorks Inc., Natick, MA) by finding the parameter set having the least sum of squared residuals (SSR) among 5000 iterations or the parameter set of having the SSR below the default threshold, 10^{-8} . The fitted logistic functions are shown in Figure A3.1.

Phenological transitional timings (green-up, maturity, senescence and dormancy) were defined as the dates when the fitted phenology profile, I_1 or I_2 , starts to show a rapid and sustained increase or decrease tendency. Therefore, the timings can be found in a robustly objective manner as the dates when the curvature (κ , Eq.A3.2) of the fitted phenology model has the greatest changes (Zhang et al., 2003).

$$\begin{aligned}\kappa(t) &= \frac{d^2 I(t)}{dt^2} \\ &= \left[\frac{d^2}{dt^2} \left(\frac{1}{1+e^{a_1+t \cdot b_1}} \right), \frac{d^2}{dt^2} \left(\frac{1}{1+e^{a_2+t \cdot b_2}} \right) \right]\end{aligned}\quad (\text{A3.2})$$

The rate of the curvature change ($d\kappa(t)/dt$) has the local minimum and maximum values when the second derivative of the curvature ($d^2\kappa(t)/dt^2$), which is equivalent to the fourth derivative of the phenology model, becomes zero (Eq. A3.3). The analytical solutions of the fourth derivative of the phenology model (Hwang, 2010) are the transitional timings (t_G , t_M , t_S , and t_D in Eq. A3.4, Figure A3.1):

$$\frac{d^2\kappa(t)}{dt^2} = \frac{d^4 I(t)}{dt^4} = 0 \quad \text{at } t = [t_G, t_M, t_S, t_D] \quad (\text{A3.3})$$

$$\text{where } [t_G, t_M] = \frac{\ln(5 \mp 2\sqrt{6}) - a_1}{b_1}, \quad [t_S, t_D] = \frac{\ln(5 \mp 2\sqrt{6}) - a_2}{b_2} \quad (\text{A3.4})$$

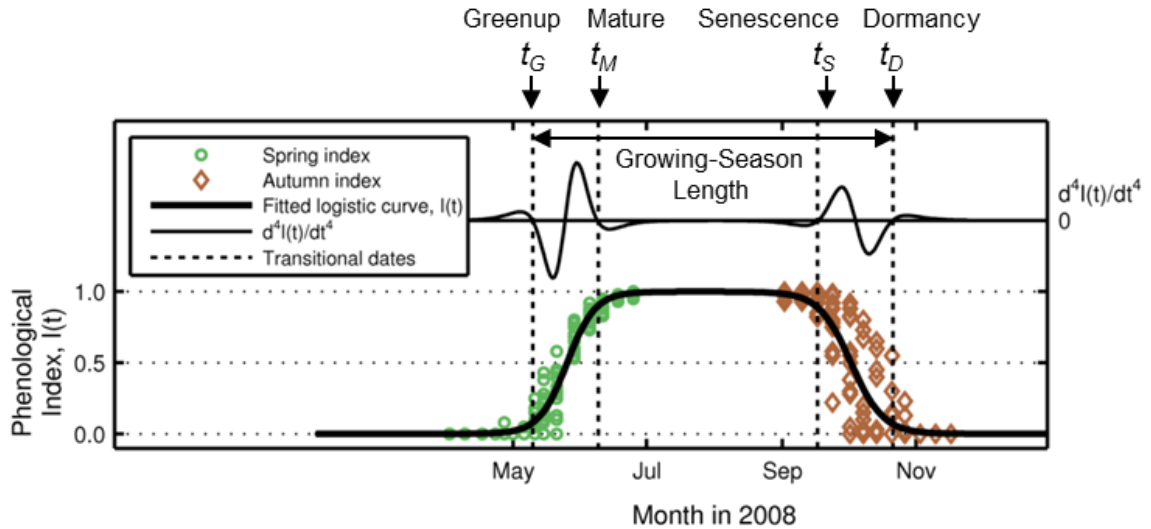


Figure A3.1. Schematic diagram of estimating phenological transitional timings. Spring and autumn phenological indices (green circle and brown diamond) using the ground-based visual observations in 2008 (hf003-03, hf003-04). The black thick line is the fitted logistic phenology model (Eq. A3.1). The solutions of the fourth derivative of the fitted model (thin black line on the top) are the phenological transitional timings (Eq. A3.4) expressed as vertical dash lines (t_G , t_M , t_S , t_D).

Phenological transitional timings from the seventeen years from 1992 to 2008 were estimated by repeating the above method for each year individually (Figure A3.2), and identifying the interannual variations in the timings (Figure A3.3). These interannual phenological timings were incorporated in the parameterization of the deciduous and mixed forest (Table 3.3).

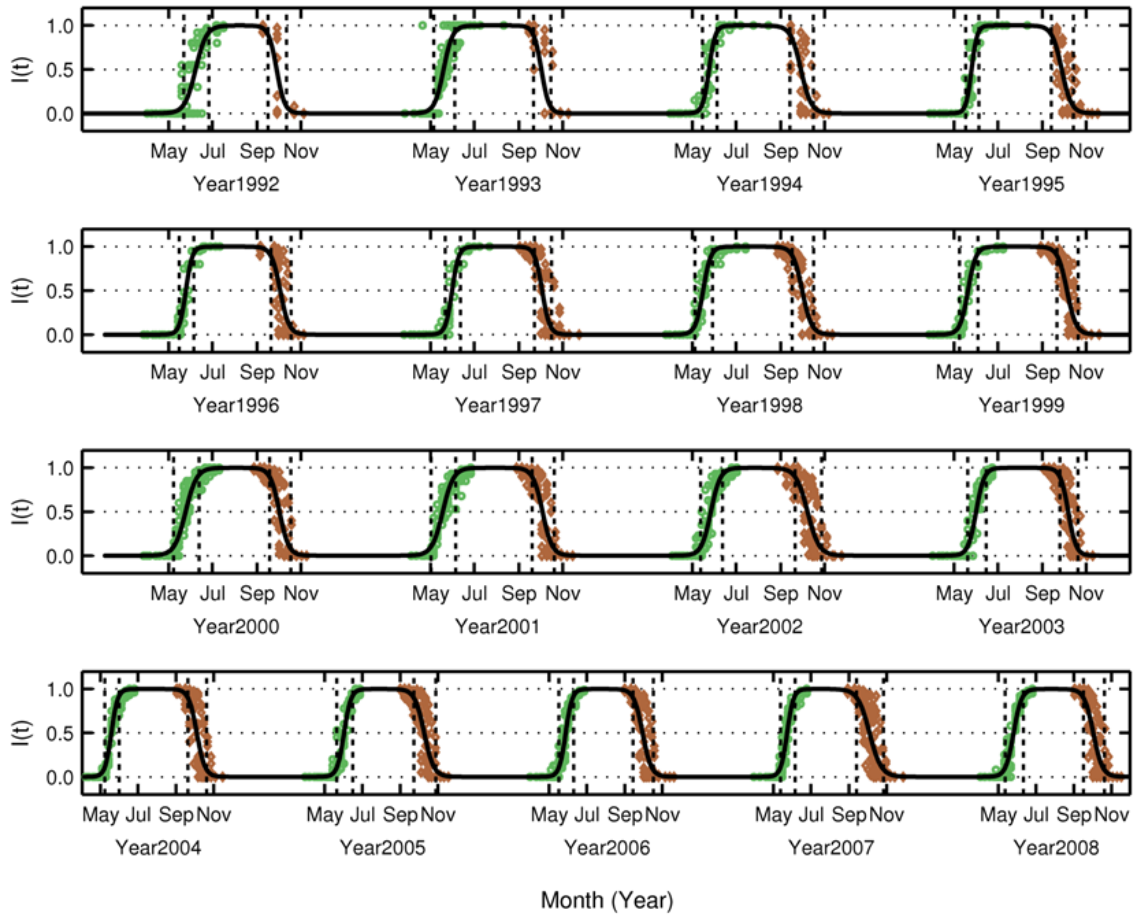


Figure A3.2. Schematic diagram of estimating phenological transitional timings from 1992 to 2008. Setup is the same as Fig A2.1. Spring and autumn phenological indices (green circle and brown diamond) using the ground-based visual observations (hf003-03, hf003-04). The black line is the fitted logistic phenology model (Eq. A3.1), and the phenological transitional timings (Eq. A3.4) expressed as vertical dash lines (t_G , t_M , t_S , t_D).

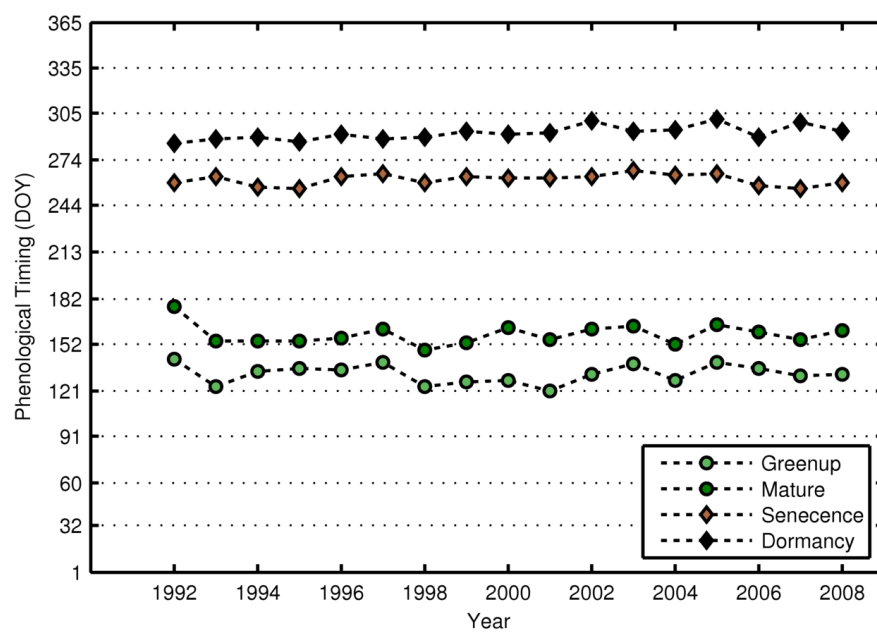


Figure A3.3. Temporal plot of phenological timings from 1992 to 2008.

Chapter 4. Simulating hydrological impact of Hemlock woolly adelgid (*Adelges tsugae*) damage on downstream freshwater yield: early assessment using a distributed ecohydrological model

4.1. Introduction

The hemlock woolly adelgid (HWA), *Adelges tsugae* Annand, is an invasive destructive pest in the eastern United States, first reported in Richmond, Virginia in 1951 (Evans, 2004). A HWA inserts its long, thin, flexible stylet into the base of a hemlock needle and feeds on nutrients in the xylem ray parenchyma cells of the needle (Havill et al, 2014). HWA has a two-generations per year life cycle in North America, increasing its population at an explosive growth rate, resulting in as many HWA as there are needles in just a few years. The infested hemlock starts to be covered by a white woolly coating at the base of its needles, accompanied by a number of symptoms (such as discoloration, desiccation, and a gradual loss of needles) and eventually the tree dies within 4-15 years (Evans, 2004; Stadler et al., 2005).

HWA is not considered a destructive pest in its native habitat (Japan) or in the western North America where it was first sighted in the early 1920s. Mountain hemlock (*Tsuga mertensiana*) and western hemlock (*Tsuga heterophylla*) from northern California to southeastern Alaska have not exhibited significant mortality. However, eastern hemlock (*Tsuga Canadensis*) in the northeastern United States and Carolina hemlock (*Tsuga caroliniana*) in the southern Appalachian Mountains have shown little or no resistance to the insect, and these hemlock populations have substantially declined over

the past few decades as HWA has gradually spread out of its initial infestation area (Ellison et al., 2010; Evans & Gregoire, 2007; Stadler et al., 2005). Starting from Virginia in 1951, HWA has spread at an average rate of 12.5-20.8 km/year (Evans & Gregoire, 2007), marching up to southern New England by 1985, covering 40% of Massachusetts by 2000 (Orwig et al., 2008), and currently affecting about half of the entire eastern hemlock forests in the northeast (Havill et al., 2014).

Eastern hemlock is the most dominant conifer along the riparian area in the northeast mountainous region, a so called “*foundation species*” (Orwig et al., 2008; Webster et al., 2012). This long-lived and shade-tolerant tree plays a unique and crucial role in northeastern ecosystems. Its dense canopy casts deep shade that creates cool and moist microclimates underneath the canopy, controlling biogeochemical cycles on the ground as well as in the soil (Eschtruth et al., 2013). Various kinds of studies have been conducted to investigate what changes the HWA-induced hemlock loss result in: changes in the microclimate and transitions such as understory light level, throughfall amount and chemical properties, soil and streamflow temperature, and soil and litter decomposition (Finzi et al., 2014; Orwig & Foster, 1998; Stadler et al., 2005; Webster et al., 2012). There are also studies assessing the impact of species composition change in the future on the carbon, water, and nitrogen cycles if hemlock stands are replaced by black birch (*Betula lenta*) in the northeast region and by great laurel (*Rhododendron maximum*) in the southern Appalachian (Brantley et al., 2013; Finzi et al., 2014; Jenkins et al., 1999; Stadler et al., 2005; Webster et al., 2012).

The loss of foundation species would alter hydrological cycle of northeastern ecosystems in several different ways (Adams et al., 2012; Brantley et al., 2014). The foremost and significant change would be reductions in transpiration due to the loss of canopy that would also alter the precipitation partitioning (i.e. decrease of interception and increase of throughfall). With increased solar radiation and wind through a more open canopy, evaporation on the ground surface would also be increased (Adams et al., 2012; Royer et al., 2011; Royer et al., 2010). Snow intercepted by needles usually has a higher sublimation rate compared to snowpack on the ground, therefore the amount of snowpack as well as the subsequent snowmelts in the early spring will be highly disturbed in snow-dominated regions (Adams et al., 2012; Boon, 2012). Besides the transitions listed above, a number of subsurface changes may occur simultaneously and also in subsequent periods (e.g. changes in soil moisture, dynamics of groundwater recharge and downstream freshwater yield). For example, Bearup et al. (2014) reported groundwater contribution to streamflow was increased after insect infestations (mountain pine beetle in the Rocky Mountain area), indicating that the loss of transpiration affected the entire hydrological processes.

The impact of HWA infestation on the downstream freshwater yield in the northeastern United States is particularly important for those regions that rely heavily on fresh surface water from the forested catchments for their human water use (Brantley et al., 2014; Vose et al., 2011), but poorly understood. Most of previous insect-infestation studies has focused on assessing the changes in the water yield resulting from the mountain pine beetle outbreaks in the Midwest United States and in Canada (reviewed in

Mikkelson et al., 2013), yet the impact of HWA on the water yield in the northeastern United States has been rarely investigated. One very recent study has reported that annual streamflow decreased after a HWA infestation, while storm-peak flow increased in the catchment in the southern Appalachian where eastern hemlocks cover 6% of catchment basal area (Brantley et al., 2014), which is opposite to the previous studies suggesting that streamflow of the insect-infested catchment would be increased because of the reductions in evapotranspiration (Adams et al., 2012; Ford et al., 2007; Mikkelson, Bearup, et al., 2013). Other previous HWA studies have mostly focused on measuring sap flux, leaf water potential, and leaf gas exchange rate to assess the hydraulic impact of HWA on a single tree (Brantley et al., 2013; Domec et al., 2013; Ford & Vose, 2007). These plot-scale measurements might have had difficulties in estimating the changes in the downstream freshwater yield from a catchment especially from those catchments having heterogeneous landscapes with mixed forests (Bearup et al., 2014).

The change in downstream freshwater yield from an insect-infested catchment with a landscape composed of multiple different species is the consequence of combined changes in the hydrological processes of each individual species and the water exchange among species and are connected through lateral surface runoff and subsurface runoff (Bearup et al., 2014; Mikkelson, Bearup, et al., 2013). Spatially-distributed process-based ecohydrological models, therefore, are particularly appropriate to disintegrate these combined effects into individual process (e.g., transpiration, evaporation, intercept, snowpack and snowmelt, etc) at different spatial scales (i.e., stand-scale as well as catchment-scale), which may not be fully assessed with previous empirical approaches

such as the temporal analysis of a single catchment and paired-watershed studies (Bethlahmy, 1974; Brantley et al., 2014; Guardiola-Claramonte et al., 2011; Livneh et al., 2015). Recently there have been increased efforts to estimate the impact of insect infestation on downstream freshwater yield with hydrologic models (Livneh et al., 2015; Mikkelsen et al., 2013), but the impact of HWA infestation in the northeastern region has not yet been investigated.

In this study, we scale up the stand-scale hydraulic failure caused by an HWA infestation into catchment-scale hydrological changes, focusing on the changes in the freshwater yield from a headwater catchment with mixed-species land cover. We first report HWA infestation conditions and the vigor conditions of eastern hemlocks in 2009 (early stage of the HWA infestation) and in 2014 in the study site, the Harvard Forest. A simplified representation of the hydraulic failure by the HWA infestation was calibrated using field data and incorporated into a spatially-distributed process-based ecohydrological model. We assess the changes in the freshwater yield caused by the HWA infestation using model estimates as well as field data.

4.2. Methodology

4.2.1. Study site

The main study site is the Bigelow-Brook (BB) headwater catchment (outlet: Bigelow lower pipe at 42.53901°N, 72.17201°W. Figure 2.1a) on the Prospect Hill Tract in the Harvard Forest. The forest experiences a cool and moist temperate climate with an annual mean temperature of 8.5 °C, ranging from -7 °C in January to 20 °C in July. Mean

precipitation is approximately 1100 mm distributed evenly throughout the year, 25% of which is snow (Xu et al., 2012). Topography in the catchment is moderate, varying from 365 m to 415 m above sea level. Soils are mostly well-drained sandy-loam types (*Berkshire-Marlow* association and *Peru-Marlow* association in USDA-NRCS soil survey database) with about 3 m-depth from the gneiss and schist bedrock (Currie *et al.*, 1996; Xu & Sayers, 2010). There are very poorly drained woody wetlands (*Bucksport and Wonsqueak* mucks in the USDA-NRCS soil survey database) at the lower edge of the catchment representing about 7% of the total area.

The forest is a hardwood - white pine - hemlock transitional region mainly dominated by red oak (*Quercus rubra*), red maple (*Acer rubrum*) and eastern hemlock (*Tsuga canadensi*), and also some black birch (*Betula lenta*) and white pine (*Pinus strobes*). In the catchment, eastern hemlock dominates the coniferous forest on the west-facing hill, encompassing about 44% of the catchment area (Figure 2.1b; Harvard Forest Data Map: 1986-1993 Stand Boundaries; <http://cga-5.hmdc.harvard.edu/forest/>). An adjacent Nelson-Brook (NB) headwater catchment (outlet: Nelson big-weir at 42.53492°N, 72.18661°W. Figure 2.1a) includes another hemlock-dominated forest on its north-facing hill, making up about 25% of that catchment area. This study focused on the streamflow change in the BB catchment assuming that the hydrological processes in the catchment have been more affected by the HWA-induced hemlock loss relative to the NB catchment with less of a hemlock-dominated conifer forest. However, the NB catchment was used to serve as the reference catchment in a comparative analysis. The Hemlock tower (Fluxnet site code: US-Ha2, hereafter "HEM-tower") was built at the northern edge

of the hemlock-dominated forest in the NB catchment. The HEM-tower measures carbon dioxide and water vapor flux exchanges between the forest and the atmosphere and data from June 2004 to July 2014 was used in this study.

4.2.2. Data overview

Tree inventory

A 0.72 ha (120 m × 60 m) sampling plot (northwest corner: 42.538306°N, 72.179028°W) was set up in 1990 in the hemlock-dominated forest in the NB catchment (Harvard forest dataset ID: HF031-01; Foster & Plotkin, 1999). Standardized sampling procedures that inspect for the presence or absence of HWA on two branches per stand for all the sample stands (Costa et al., 2006) were performed on 49 eastern hemlock stands in 2009 and for 41 eastern hemlock stands in 2014, and only stands that were inspected in both 2009 and 2014 were used to compare the infestation rates in 2009 and 2014, 29 stands in total.

Visual inspection of stand condition (dead or living) as well as vigor status in 1993, 1999, 2009, and 2014 were used in this study (Harvard forest dataset ID: HF031-01; Foster & Plotkin, 1999). Vigor index 1 refers to a healthy stand with the foliar loss less than 25%, vigor index 2 to 25%-50% of foliar loss, vigor index 3 to 50-75% of foliar loss, vigor index 4 to 75-99% of foliar loss, and vigor index 5 indicates a dead stand at the inspection time (D. Foster et al., 1999). For vigor status, only the stands observed in both 2009 and 2014 were considered as a measure of the changes in the vigor status. In calculating average annual mortality rate, stands that were observed at both the beginning

and the end of each sub-period (i.e. from 1993 to 1999, from 1999 to 2009, and from 2009 to 2014) were counted.

Ground-measured LAI (Harvard forest dataset ID: HF150-01; Hadley, 2009) was used for model performance evaluation and also as a measure of the impact of HWA. The mean and the standard deviation of LAI are calculated from the measurements along two transects with compass bearings of 195° and 225° that cut through the hemlock-dominated forest (Hadley et al., 2002). LAI in May 2012 was excluded which was measured around at noon under the direct sunlight, while others were measured at dawn or dusk.

Water flux estimates

This study used half-hourly water vapor flux (F_{H_2O} , equivalent to ecosystem evapotranspiration, ET) measurements using the eddy-covariance technique (Baldocchi et al., 1988) from 2004 to 2014 at the HEM-tower (Harvard forest dataset ID: HF103-03; Hadley, 2003). This dataset is open for public research and available at the website (<http://harvardforest.fas.harvard.edu/data-archive>). Since the landscape around the HEM-tower is quite heterogeneous due to a nearby red oak-dominated forest and woody wetland, flux data only from the hemlock-dominated forests (wind direction between 190 and 225 degree) were accepted (11% of total available data). ET flux data on the rainy days and the day after rain were removed to prevent any unpredictable bias resulting from rainfall (Loescher et al., 2005). Such unpredictable results include a rapid change in pressure inside the gas tubes due to the sudden cooling of the skin by the rain drops,

interference by water droplets on the anemometer affecting pulse times, and moisture inside the electronic instruments producing electrical noise (Hadley et al., 2002). Instead of filling the unevenly distributed gaps using an empirical model, the mean value of the daytime measurements (11am and 3pm) was taken as the representative daily flux (mm hour^{-1} , hereafter “ ET_{day} ”).

Daily streamflow estimates have been provided since December 2007 (Harvard forest LTER archive ID: hf070-03. Boose, 2007), and the record of estimates for 7 years between January 2008 and March 2015 were used in this study. Daily streamflow estimates were converted to area-normalized streamflow by dividing the drainage areas (BB catchment: 0.6 km^2 , NB catchment: 0.58 km^2). Drainage areas were delineated using *r.water.outlet* module in GRASS GIS 6.4.3 (GRASS Development Team, 2012). Daily streamflow was aggregated to monthly streamflow (mm month^{-1}) and annual streamflow (mm year^{-1}).

Meteorological data

Daily meteorological data (maximum, minimum and average temperature and precipitation) from Fisher station (42.53311°N , 72.18968°W . Figure 2.1a; Harvard forest LTER archive ID: hf001. Boose, 2001) was utilized for both catchments. Gaps in the temperature data were filled by the mean temperature of the 20-years combined with the mean temperature of the 10-days surrounding the day without data. Gaps in precipitation data were filled by taking average of nearby National Climate Data Center (NCDC) records from four stations (GHCND Name-ID: Orange Municipal Airport-

USW00054756, Birch Hill Dam-USC00190666, Barre Falls Dam- USC00190408). Daily atmospheric CO₂ mixing ratio was incorporated into the model by taking daily mean value of the atmospheric CO₂ concentration (parts per million:ppm) recorded at the HEM tower every 30 minutes (Harvard forest dataset ID: HF103-03; Hadley, 2003). Abnormal peaks and drops (>420 ppm and <340 ppm) were removed from the data. Gaps were filled by scaling the reference annual cycle, the average of annual cycles from 2005 to 2013, to the long-term trend measured from the ice cores at East Antarctica (Etheridge et al., 1996). Additional meteorological data used in this study is as follows: daily mean vapor pressure deficit (VPD) estimates, daily mean wind speed above canopy measured by sonic anemometer on the HEM-tower (27 m, 5 m-above average canopy top), daily total photosynthetically active radiation (PAR) above canopy (24m) (Harvard forest dataset ID: HF103-03; Hadley, 2003). More information about the instruments can be found in Hadley et al. (2008).

4.2.3. Tree inventory analysis

We first examined how much the HWA infestation had increased from 2009 to 2014. We grouped the total sample stands which were observed in both 2009 and 2014 (29 stands) into three infestation status categories: HWA presented on both branches ('+/+'), HWA on only one branch ('o/+'), and HWA on neither branch ('o/o'). In each infestation-status category, we counted the number of stands depending on the DBH classes (5 classes: <15, 15-30, 30-45, 45-60, and >60 cm). To determine whether or not the infestation status in 2014 is significantly differed from the status in 2009, we

performed the chi-square analysis for the overall stands as well as for each DBH class using *crosstab* in Matlab (R2013a, The MathWorks Inc., Natick, MA).

Stand vigor indices in 1999, 2009 and 2014 were also categorized depending on the DBH class. We calculated the mean vigor index for each DBH class as well as for the entire hemlocks. Stand vigor index in 1999 represented the initial reference stand vigor condition before the HWA infestation had started in the study site.

Average annual mortality rates (% year⁻¹) of each DBH class and of the entire sample of hemlocks were calculated (Eq. 4.1; Sheil et al., 1995). From the 4 years of stand condition data (1993, 1999, 2009, and 2014), mortality rates of 3 sub-periods were calculated (from 1993 to 1999, from 1999 to 2009, and from 2009 to 2014), with the assumption that the mortality is constant within the period.

$$M = 100 \left[1 - \left(N_{t2} / N_{t1} \right)^{1/(t2-t1)} \right] \quad \text{Eq (4.1)}$$

where N_{t1} and N_{t2} are the stand counts alive at the beginning and end year, $t1$ and $t2$, respectively.

4.3.4. Water flux change analysis

We employed a one-way analysis of variance (ANOVA) to test for significant differences in the summertime ET_{day} from 2005 to 2013 at the significance level of 0.05 (In this study, “summertime” was defined as the fixed-period between June 1 and August 31). Fisher’s least significant difference (LSD) post-hoc test, a set of individual t-tests comparing only two groups at a time and reiterating for all the possible pairs, was

followed to determine the years that were significantly different from the reference year, 2009.

The impact of HWA-induced Loss of Conductivity (LC) on the BB-catchment streamflow was assessed with the paired-catchment approach, one of the widely-used methods to examine the streamflow responses to the vegetation changes such as deforestation and forest type conversion within a disturbed catchment compared to a reference catchment that has similar characteristics of vegetation, soil, slope, aspect, and climate (Bates et al., 1928; Bearup et al., 2014; Brown et al., 2005). We first objectively sorted out the calibration period and the LC period based on the results from the LSD test on the summertime ET_{day} ; the calibration period when there was no significant LC-induced reduction in the ET_{day} and the LC period after significant ET_{day} reduction noticed from the test. The calibration relationship between the monthly streamflow of the study catchment (BB catchment) and the monthly streamflow of the reference catchment (NB catchment) was estimated with a linear regression. The deviations from the 95% confidence intervals during the LC period were considered as statistically significant changes in the streamflow (Hornbeck et al., 1993). The HWA-induced annual streamflow change (ΔQ_{BB}) was calculated by adding up the monthly deviation in vegetation-years, assuming there was no significant change in the annual groundwater storage. In this study, a vegetation-year was defined as the period from April 1 of a year to March 31 of the following year. Plant starts to transpire at the beginning of the vegetation year using soil water that was charged during the preceding winter and consumes as much of this stored water as it transpires during the growing season. The soil water consumed during the

growing season is recharged during the following dormancy, and thus less streamflow generated. The vegetation year is marked with the prefix “v” (e.g., v2012: April 1, 2012 and March 31, 2013).

4.2.5. Ecohydrological Modeling

The Regional Hydro-Ecologic Simulation System (RHESSys) is a spatially-distributed process-based ecohydrological model to simulate carbon, water and nitrogen cycles (storages and fluxes) within a catchment boundary (Band et al., 1993; Tague & Band, 2004) using a number of algorithms evolved from several existing independent and specialized models: Biome-BGC (Running & Hunt Jr., 1993) for carbon and water processes, DHSVM (Distributed Hydrology Soil Vegetation Model; Wigmosta et al., 1994) to explicitly represent spatially-distributed hydrologic pattern over a landscape, CENTURY_{NGAS} (Parton et al., 1993; Parton et al., 1996) for enhanced nitrogen processes, and MT-CLIM (Running et al., 1987) to extrapolate microclimate conditions through the landscape depending on elevation, aspect and slope. RHESSys has been evaluated at a number of ecohydrological study sites across different types of ecosystems; a high-elevation mountain watershed, a snow-dominated mountain ecosystem, a Mediterranean ecosystem, and deciduous-conifer ecosystems in a humid continental climate (Baron et al., 2000; Christensen et al., 2008; Nemani et al., 1993; Tague et al., 2009; Vicente-Serrano et al., 2015). RHESSys also has been applied in spatially heterogeneous landscapes (Hwang et al., 2015; Mackay et al., 1997; Mittman et al., 2012).

Loss of xylem conductivity

The exact mechanism of how an infested hemlock dies is still unknown. A significant depletion of nutrients (e.g. photosynthate) has been pointed out as a leading cause of mortality, which results from the inability of a tree to support its current metabolism and to generate new needles (Domec et al., 2013; Havill et al., 2014). Recent studies have shown that an infested hemlock develops "false growth rings", abnormal thick-walled xylem within an annual ring accompanied with traumatic resin canals, as a reaction to toxic HWA saliva that is injected to the tree through "the inserted stylets" (Domec et al., 2013; Gonda-King et al., 2012, 2014; Havill et al., 2014; Pontius et al., 2005a, 2005b). The distinctive features of the false growth rings, traumatic resin canals and thick parenchyma cells, can be also found in "ring shakes", abnormal but naturally-occurred ring structures. It has been suggested that the ring shakes result from the dehydration of the parenchyma cells due to sudden changes (increase or decrease) in the radial growth process (Koehler, 1933). Climate (temperature and wind), aging of the tree, as well as wounds by birds pecking for insects have been pointed out as additional significant causes of the sudden growth changes (Jorgensen et al., 1964; McManus et al., 1999; Shigo, 1963). However, the false growth rings in infested hemlocks may be an indicator that the water transport capacity within xylem parenchyma cells is disturbed, causing dehydration and water stress, which likely will contribute to mortality (Domec et al., 2013; Havill et al., 2014; Pontius et al., 2005b).

There are various approaches in describing individual tree mortality (Monserud et al., 1999; Temesgen et al., 2005). Instead of exerting direct control on the mortality, we

implemented the HWA-induced reductions in water transport into the model by embedding a simple probability function where the coefficients were calibrated with the response variable (i.e. the summertime-mean ET_{day} in this study). We adapted the survival (reliability) function (Eq. 4.2) of the Weibull probability density distribution (Somers, Oderwald, Harms, & Langdon, 1980) that has been shown to be a good approximation for the loss of xylem conductivity (referred to as “LC” hereafter) due to drought (Mcdowell et al., 2013; Sperry et al., 1998):

$$f_{LC}(t) = e^{-\left(\frac{t-t_0}{\lambda}\right)^k} \quad \text{Eq (4.2)}$$

where t is time in years, t_0 is the beginning year when the observable reduction in the water transport started, and λ and k are the function coefficients, scale parameter and shape parameter respectively. The LC function, $f_{LC}(t)$, is the probability density function ranging from zero (no reduction in xylem conductivity) to one (complete loss of xylem conductivity. no water transport in the xylem cells in the tree). It is unknown exactly when HWA started to show up in Harvard Forest. It had not been reported until 2004 (D. A. Orwig et al., 2004), and then was observed in 2009 (D. R. Foster et al., 1999). We tried to determine t_0 between 2005 and 2008 in a robust manner, by fitting the $f_{LC}(t)$ in Eq. 4.2 from 2005 to 2008 individually using a nonlinear regression function, *nlinfit*, in Matlab (R2013a, The MathWorks Inc., Natick, MA) (Figure 4.1). It was assumed that there was no LC until the beginning year t_0 , therefore the $f_{LC}(t)$ was set to one at t_0 . Example scales of the $f_{LC}(t)$ in 2005 and 2008 are presented on the right-side Y-axes in Figure 4.1. Mean square error (MSE, colored circles in Figure 4.1) display the lowest

values when the LC started in 2008, so we selected those fitting coefficients as the best behavioral LC function parameters: $\lambda = 8.2301$ and $k = 2.3541$. In 2013, the $f_{LC}(t)$ was 0.62, meaning a 38% reduction in the water transport, which is close to the 40% reduction in the field-measured stomata conductance (g_s) reported for HWA-infested eastern hemlock (Domec et al., 2013).

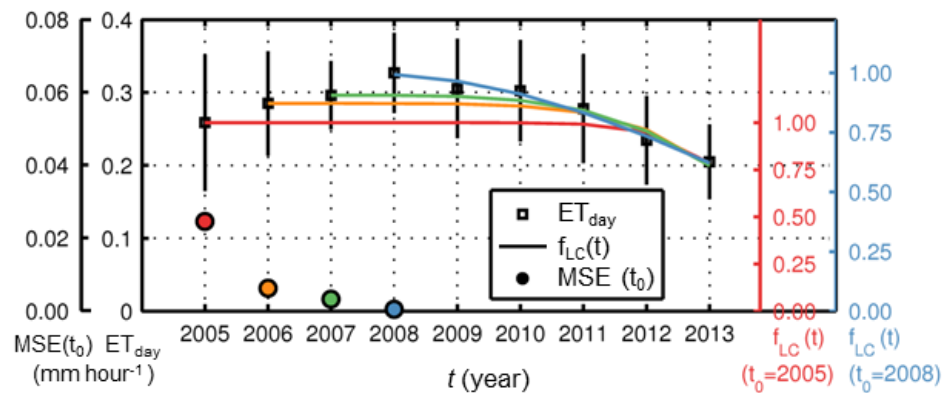


Figure 4.1. Summertime-mean ET_{day} (square symbol), mean square error (MSE, colored circles) and the survival functions with the Weibull probability distribution, $f_{LC}(t)$ in Eq. 4.2. Y-axes for MSE and ET_{day} are on left side, and Y-axes of the $f_{LC}(t)$ in 2005 and 2008 are on the right side, having same color with the MSE circle and the $f_{LC}(t)$ accordingly.

Stand-level water loss by transpiration (i.e. total water transportation throughout the xylem cells within the stand) in RHESSys is calculated using the Jarvis multiplicative model (Jarvis, 1976). The Jarvis model is an empirical estimates of the observed responses of g_s to each environmental factor, assuming the impact of each factor on g_s is independent to the other. Since there is no data yet to quantify the dynamics of LC depending on the environmental factors, we assumed the HWA-induced LC is independent of any other environmental factor over the study period. We multiplied the

$f_{LC}(t)$ to the existing multiplicative model (Eq. 4.3), and executed it only for the hemlock-dominated coniferous forests.

$$g_s = f_d(APAR) \cdot f_d(LWP) \cdot f_d(VPD) \cdot f_d(T_{avg}) \cdot f_d(T_{min}) \cdot f_{LC}(t) \quad \text{Eq (4.3)}$$

where APAR, LWP, and VPD stand for the absorbed photosynthetically active radiation, leaf water potential, and vapor pressure deficit, respectively. T_{avg} and T_{min} are daily average and minimum temperatures respectively. It should be noted that g_s is calculated every day with the daily environmental factors accordingly (we run the model at a daily scale), while the $f_{LC}(t)$ is assumed to be static over the given year. Each environmental factor function, f_d , has a different definition and mathematical formula from one and another, and more detailed description is available in references (Körner, 1995; Tague & Band, 2004; White, Thornton, Running, & Nemani, 2000; <http://www.ntsg.umt.edu/project/biome-bgc>).

Model implementation

The physical characteristics of the soil and the physiological characteristics of vegetation components in RHESSys were initially parameterized as in Table 3.2 and 3.3. The Generalized Likelihood Uncertainty Estimation (GLUE) method (Beven et al., 1992, 2001) was applied to calibrate soil parameters using the prior parameters summarized in Table 3.4. Three years (from 2008 to 2010) of streamflow estimates at the Bigelow lower-pipe is not long enough to be split into two sub-periods for calibration and validation, having wet and dry year in each sub-period. Assuming physical conditions of soils in the adjacent NB catchment can be transposable to the BB catchment

(geographical parameter transposability; Klemes, 1986; Mittman, Band, Hwang, & Smith, 2012), posterior parameter sets accepted as behavioral scenarios at the NB catchment were applied to the model runs at the BB catchment (likelihood measure: log-scale Nash-Sutcliffe Efficiency in Eq. 3.12; accepting threshold of 0.2; 95% confidence interval) and validated with the streamflow estimates at the Bigelow lower-pipe from 2008 to 2010. We also examined the model performance using the LAI measurements measured in the hemlock-dominated forest.

We then performed a scenario simulation without incorporating the HWA-induced LC under (referred as to “no LC” hereafter) the identical environmental conditions to explore the impact solely induced by LC reduction. Finally we compared the differences in LAI, ET, and annual streamflow quantities.

4.3. Result

4.3.1. HWA infestation condition and stand vigor condition

In 2009, the HWA infestation was not severe: 5 eastern hemlock stands were infested by HWA (17.2% of overall sampled stands), whereas 24 stands did not have HWA on any branch (Figure 4.2). The small stand class (DBH<15cm) was the most infested DBH class, 33.3%, while the infestation rate of the small-medium stands (15cm<DBH<30cm) were only 11.1%. Only one big stand (DBH>60cm) was sampled in both 2009 and 2014, and it did not have HWA on both branches in 2009 yet. In 2014, the overall HWA infestation rate had increased to 96.5%, counting hemlock stands at least

having one infested branch. The small stands were mostly infested, 93.7%, and medium stands as well as the big stands were all infested in 2014 (100%).

The distribution of the number of uninfested and infested stands in 2014 was significantly different from 2009 ($\chi^2=39.72$, $df=2$, $p<0.0001$). The change in the overall infestation status of small stands was the most significant among the DBH classes ($\chi^2=21.82$, $df=2$, $p<0.001$) as well as small-medium stands ($\chi^2=14.40$, $df=2$, $p<0.001$) whereas the medium stands (30cm<DBH<45cm) have experienced relatively less change ($\chi^2=4.00$, $df=2$, $p=0.135$).

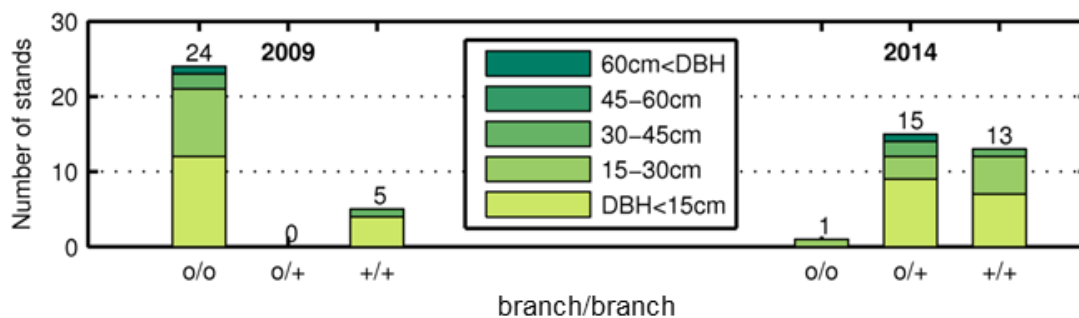


Figure 4.2. Absence/presence of HWA in 2009 and 2014. o/o indicates both branches were not infested; o/+ indicates one branch was infested and the other branch was not infested; +/+ indicates two branches were infested.

As HWA infestation progressed, stand vigor had gradually diminished. Mean and standard deviation of vigor index for each DBH class as well as the overall annual vigor index are summarized in Table 4.1 and plotted in Figure 4.3. Before the HWA infestation, in 1999, eastern hemlocks in any DBH class were mostly healthy, average vigor index of 1.09. In 2009, at the initial stage of the HWA infestation, small stands lost about half of the foliar area (mean vigor index of 2.08), and small-medium stands started to lose foliar

area as well. The sampled big stands were not infested in 2009, and as expected, there was no loss of foliar area recorded. Overall, stands were mostly healthy in 2009 with the mean vigor index of overall samples 1.45. In 2014, reductions in the vigor index were prevalent in all DBH classes. Small stands lost more than half of their foliar area (mean vigor index of 2.48), and medium and big stands also showed noticeable reductions in their vigor (mean vigor index between 1.65 and 2.05). In average, sampled eastern hemlocks lost 25-50% of its foliar area in 2014.

Table 4.1. Stand vigor index mean and standard deviation (within parenthesis) of each DBH class as well as overall class in 1999, 2009, and 2014.

Species	DBH (cm)	Vigor Index		
		1999	2009	2014
Eastern Hemlock	< 15	1.28 (0.67)	2.08 (0.72)	2.48 (0.81)
	15 - 30	1.06 (0.33)	1.48 (0.61)	2.05 (0.67)
	30 - 45	1.00 (0.00)	1.14 (0.42)	1.68 (0.58)
	45 - 60	1.00 (0.00)	1.00 (0.00)	1.65 (0.65)
	> 60	1.00 (0.00)	1.00 (0.00)	2.00 (0.81)
	Annual	1.09 (0.42)	1.45 (0.66)	1.95 (0.72)

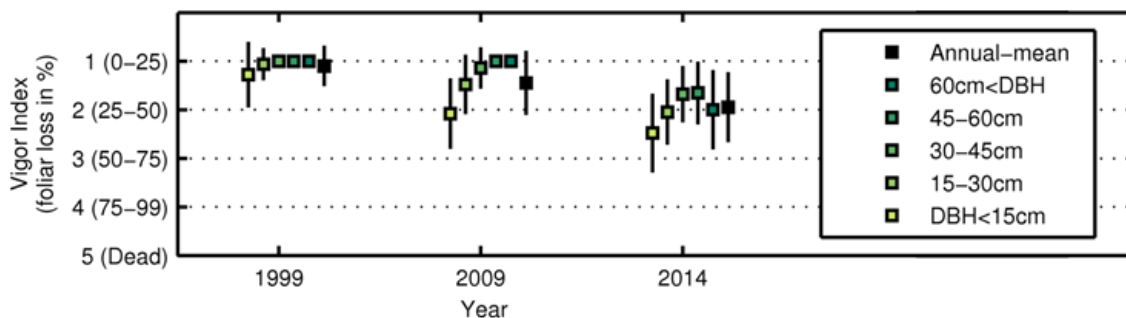


Figure 4.3. Stand vigor index mean (square) and standard deviation (vertical bar) of each DBH class (indicated by the colors) and overall class (black-filled square)

The overall average annual mortality rate for all species from 1993 to 2014 was steady, ranging from 1.49% to 1.99% (Table 4.2). Small stands had the highest mortality compared to other size stands, and the mortality was increased between 2009 and 2014 by 2.2%. The overall average annual mortality rate of eastern hemlock from 1993 to 2014 was similar to the all species, 1.85-1.99%. Mortality of small stands of eastern hemlock was higher than the all species usually by 1%, and it was also increased between 2009 and 2014 by 1.6%.

Table 4.2. Population (N) and average annual mortality rates of eastern hemlock and all species

Species	DBH (cm)	N				Annual Mortality (% year ⁻¹)		
		1993	1999	2009	2014	93-99	99-09	09-14
Eastern Hemlock	< 15	126	97	63	46	3.94	4.07	5.69
	15 - 30	184	161	119	105	1.80	2.04	1.74
	30 - 45	94	96	102	106	0.36	0.10	0.39
	45 - 60	12	15	21	23	0.00	0.00	0.00
	> 60	4	4	4	4	0.00	0.00	0.00
	Overall	423	376	312	284	1.99	1.85	1.86
All Species	< 15	209	169	119	87	3.19	2.97	5.22
	15 - 30	248	222	177	162	1.46	1.70	1.63
	30 - 45	134	135	140	136	0.50	0.15	0.87
	45 - 60	36	38	44	49	0.00	0.00	0.00
	> 60	10	13	16	18	0.00	0.00	0.00
	Overall	641	581	500	452	1.68	1.49	1.99

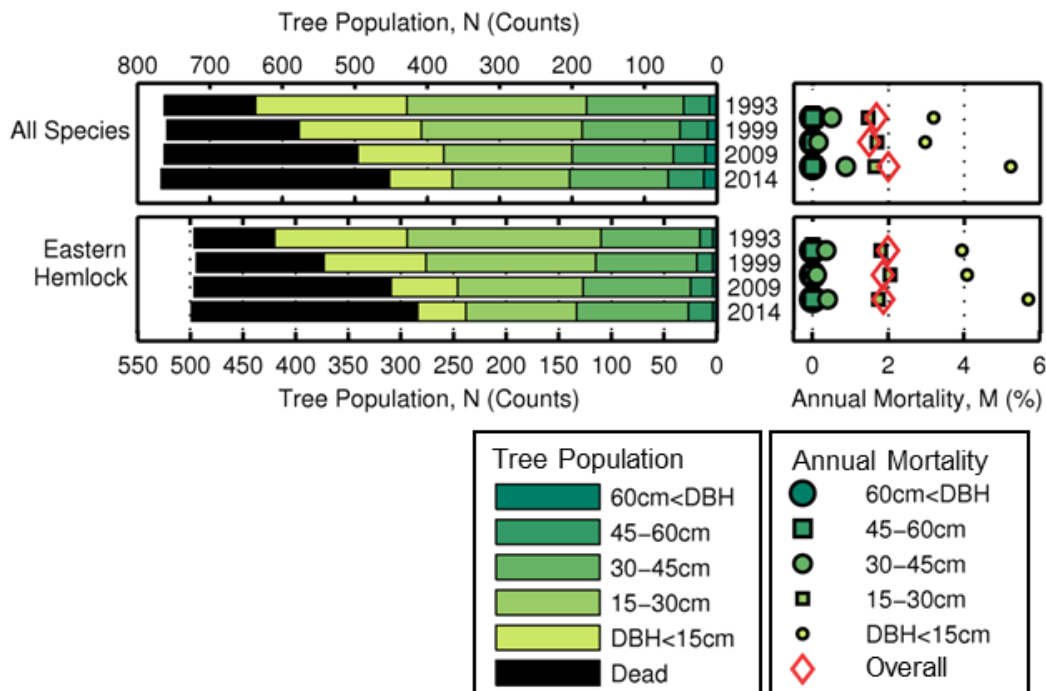


Figure 4.4. Population histogram (left) and average annual mortality rates plot (right) of eastern hemlock (bottom) and all species (top). Numbers are summarized in Table 4.2

4.3.2. Stand-level LAI and canopy-level ET

As LC increased over the study period, the responses at the stand level (LAI), canopy level (ET), and catchment level (streamflow) became noticeable. Model estimates with the simplified representation of the LC created by embedding the $f_{LC}(t)$ in the g_s showed changes after the HWA infestation that had good agreements with the field measurements.

Observed LAI in August was 4.3 ($\sigma=0.4$) in 2008, 4.8 ($\sigma=0.5$) in 2009, 4.4 ($\sigma=0.5$) in 2012, then 4.1 ($\sigma=0.4$) in 2013 (Figure 4.5a). LAI in April was 4.1 ($\sigma=0.3$) in 2013, and 3.4 ($\sigma=0.3$) in 2014. The relatively large increment of August LAI from 2008 to 2009 of course might be not a real signal of rapid growth considering the age of the hemlock stands, 100-230 years old (Hadley et al., 2008), but a measurement error. However,

Hadley & Schedlbauer (2002) had reported mean LAI of 3.5 during the non-growing season and 4.4 during the growing season in 1997. Therefore, a decrease of LAI after 2012 seems to have occurred. The LAI in April 2014, 3.4, was in fact lower than the LAI in January 2002, 3.6 (Hadley et al., 2008).

Simulated LAI in the LC-scenario (LAI_{LC} : 95% confidence boundary colored in red in Figure 4.5a) depicted the decrement with high agreement ($residual < 0.2$). There was no noticeable change until 2011 (mean LAI from 2008 to 2011 was 4.2 in April, and 4.6 in August), and LAI_{LC} started to decline rapidly in 2012, down to 3.7 in August 2014, 20% reduction compared to the mean between 2008 and 2011. In the scenario without having LC (LAI_{NO-LC} : 95% confidence boundary colored in blue in Figure 4.5a), LAI_{NO-LC} continued to increase, reaching 4.72 in 2014, 1.6% of increment compared to the mean from 2008 to 2011. Therefore, the net impact of LC by the HWA infestation equals to 22.6% reduction in LAI.

The observed summertime ET_{day} also showed significant reduction after the HWA infestation (Figure 4.5b). A one-way ANOVA indicated that at least one year differs from the other year ($F=3.62$, $df=8$, $p<0.001$). From Fisher's LSD test, we confirmed that the summertime ET_{day} values in 2012 and 2013 were significantly different (independent) from 2009 ($p=0.015$ in 2012; $p=0.011$ in 2013; in Figure 4.6). The summertime-mean ET_{day} was reduced by 21% in 2012 and by 28% in 2013 compared to the mean from 2005 to 2011. Wintertime ET_{day} was barely observed in the deep winter at Harvard Forest, unlike eastern hemlocks in the southern Appalachian Mountains that transpire about half of their annual flux in the winter and spring (Ford et al., 2007).

Simulated annual total ET in LC-scenario (ET_{LC}) between 2005 and 2011 was about 605 mm in average ($\sigma = 30$ mm), 77% by transpiration. From the summertime-mean ET_{LC} between 2005 and 2011, ET_{LC} increased in 2012 by 1.4%, and then started to decrease by 13% in 2013, and 29% in 2014. Compared to the scenario without having a LC effect (ET_{NO-LC} , 95% confidence boundary colored in blue in Figure 4.5b), the reduction of ET_{LC} started in 2012 by 10% (66 mm), and continued to decrease by 18% in 2013 (119 mm), and by 32.5% in 2014 (211 mm). The Transpiration was decreased by 38% (194 mm) and evaporation by 13% (17 mm) compared to ET_{NO-LC} in 2014 (Figure 4.5c).

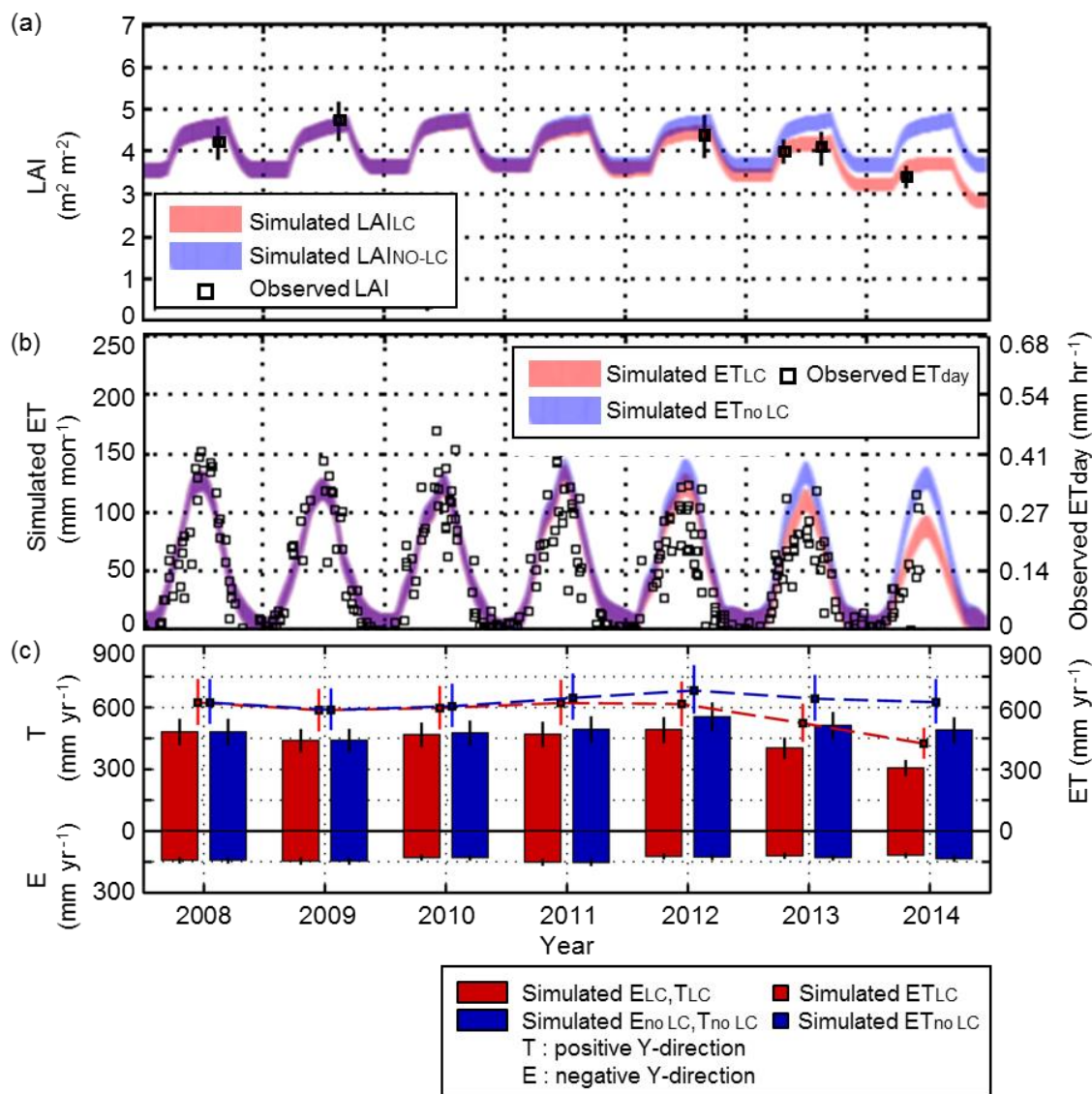


Figure 4.5. Field estimates (black squares with vertical bar of standard deviation) and model simulates (red boundary is 95% confidence interval of loss of conductivity (LC)-scenario and blue boundary is 95% confidence interval of the scenario without having LC) of (a) LAI, (b) ET (model simulates is monthly flux, field estimates is daytime hourly, and (c) simulated annual total transpiration (T, positive-direction bar), evaporation (E, negative-direction bar), and evapotranspiration (ET, square dots) with LC (red color) and without having LC (blue color)

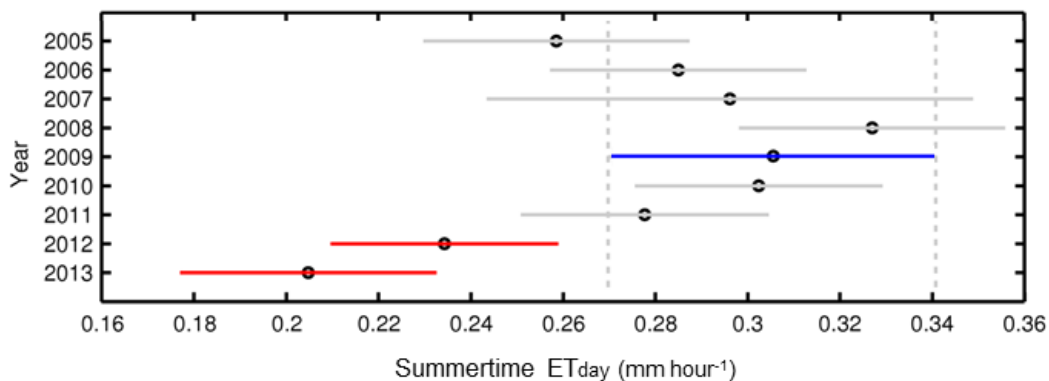


Figure 4.6. Fisher's LSD test on the observed summertime ET_{day} from 2005 to 2013. Vertical dotted lines are 95% confidence interval of ET_{day} in 2009 (blue bar). ET_{day} in 2012 and 2013 (red bars) was significantly different from 2009.

4.3.3. Catchment-level streamflow response

The hydrograph of the study site (Figure 4.7a,b) shows that the vegetation plays an important role in the hydrological processes in this catchment. Streamflow is very dependent and responsive to precipitation during the non-growing seasons, whereas large streamflow is only generated by very heavy rainfall events during growing-season (>180 mm month⁻¹). Mean annual precipitation from 2008 to 2014 was 1272 mm ($\sigma = 258$ mm). The year 2012 was very dry with annual precipitation of 883 mm, and 2010 and 2013 were also drier than the mean by 170 mm and 130 mm, respectively. There were three wet years, 2008, 2011, and 2014, and the reference year 2009 had an annual precipitation of 1277 mm, very close to the mean from 2008 to 2014.

Simulated streamflow with the LC function $f_{LC}(Q_{BB}(LC))$, the red boundary in Figure 4.7b) generally agreed with the observed streamflow ($r^2 = 0.77$ for the entire period; $r^2 = 0.89$ between May and October). Uncertainties in the snowpack and

snowmelt timings resulted in overestimated peak flows with broad confidence boundaries in March 2008 and 2009 and underestimated streamflow in January 2008, December 2008, April 2013, and April 2015. Snowmelt peak flows in 2010, 2011, and 2014 were adequately captured although with less uncertainty.

Although stand-level LC of the hemlock-dominated coniferous forests was empirically estimated as the model runs started in 2008 (Figure 4.1, lowest MSE when $t_0=2008$), the impact of the LC on the $Q_{BB}(LC)$ was not noticeable until 2010 ($< 1 \text{ mm month}^{-1}$) (Figure 4.8b). As the simulated ET_{LC} decreased because of the LC (Figure 4.5b,c), the $Q_{BB}(LC)$ started to show an increase signal compared to the simulated streamflow without LC ($Q_{BB}(no LC)$; blue boundary in Figure 4.8b) in 2011. The $Q_{BB}(LC)$ had a higher streamflow by 2.5-3 mm month^{-1} in August and September when there were heavy rainfalls ($>180 \text{ mm month}^{-1}$). In 2012, the dry year, there was hardly any change in the $Q_{BB}(LC)$ compared to the $Q_{BB}(no LC)$ ($< 1 \text{ mm month}^{-1}$) until September, the end of the growing season in these deciduous forests. From October to December in 2012, the deviations became evident with the $Q_{BB}(LC)$ was higher than the $Q_{BB}(no LC)$ by 4.5-6 mm month^{-1} for the three months. The $Q_{BB}(LC)$ in 2013 was consistently higher than the $Q_{BB}(no LC)$ by 2.5-7 mm month^{-1} throughout the year. The increase was noticeably higher in June, by 10 mm month^{-1} , when heavy rainfalls occurred. This pattern repeated in 2014 with the $Q_{BB}(LC)$ was steadily higher (2.5-8 mm month^{-1}) than the $Q_{BB}(no LC)$ throughout the year with significant increases occurring in time with heavy rainfalls events. The magnitude of the streamflow increase in 2014, however, was substantially higher than in 2013 with 22-23 mm month^{-1} in July and October.

The residual plots of the annual simulated streamflow (observed Q_{BB} -simulated Q_{BB}) and the changes in the simulated annual streamflow caused by the LC ($\Delta LC = Q_{BB}(LC) - Q_{BB}(no LC)$) in the vegetation year scale (prefix “v”) showed the impact of HWA-induced LC on the streamflow more clearly (Figure 4.7c). The $Q_{BB}(LC)$ had higher agreement with the observed flow (lower residual) compared to the $Q_{BB}(no LC)$. The residual of $Q_{BB}(no LC)$ in v2014 when the snowmelt in April 2014 and the snowpack in November and December 2014 were relatively well simulated, was as high as the residuals in v2008 and in v2009 when most of the residuals were from the uncertainties in the snowpack and snowmelt timing and amount. The ΔLC from v2008 to v2010 was less than 5 mm. The ΔLC was gradually increased from 10 mm in v2011 to 81 mm in v2014, indicating that annual streamflow increased by 16% because of the HWA-induced LC.

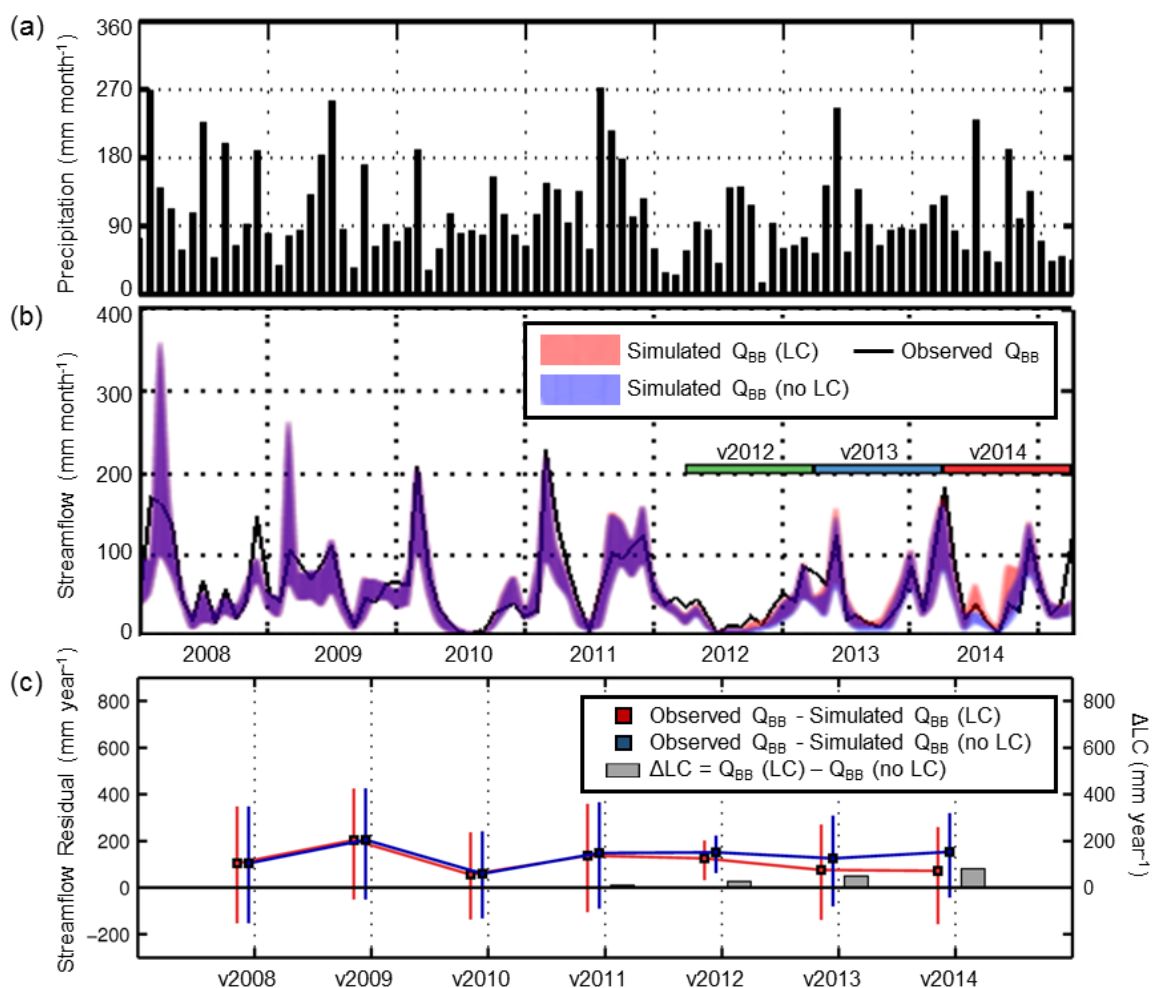


Figure 4.7. Hydrograph (a) monthly total precipitation from 2008 to 2014 (b) monthly total observed streamflow (black solid-line) and model simulates (red boundary is 95% confidence interval of loss of conductivity (LC)-scenario and blue boundary is 95% confidence interval of the scenario without having LC) (c) residual plots of the simulated streamflow (observed streamflow minus simulated streamflow). Squares are the mean residual of the 95% confidence interval and the vertical bars are the ranges of residuals of the 95% confidence interval. Gray bars (ΔLC) are the changes in the simulated annual streamflow by HWA-induced LC ($f_{LC}(t; t_0 = 2008)$ in Eq.4.2).

In the paired-catchment approach, the calibration period was designated as from v2008 to v2011 as the observed summertime ET_{day} had not yet started to significantly decline (Figure 4.6). The calibration relationship between the monthly streamflow of the study catchment (Q_{BB}) and the monthly streamflow of the reference catchment (Q_{NB}) was highly significant ($n=48$; $r^2=0.98$; $p<0.01$, Figure 4.8a). The fitted linear relationship (calibration equation: $y = 1.22x + 2.35$) was capable of characterizing low flows during the growing season as well as snowmelt peak flows in early springs ($Q_{BB}>120$ mm month⁻¹). The study catchment consistently yielded higher monthly streamflows than the reference catchment because of the differences in the hydrological conditions between the two catchments such as soil type, topographical variation and groundwater movement as well as vegetation in the catchments. Points that are above the higher limit of the 95% confidence boundary indicate that the observed streamflow was over the estimation (positively deviated), and points that are below the lower limit of the 95% confidence boundary mean that the observed streamflow was short of the expected streamflow (negatively deviated). It is noticeable that snow-melt peak flow in March 2014 (in vegetation year 2013, 'v2013' in Figure 4.8a) deviated highly from the expected streamflow.

The magnitude of the HWA-induced annual streamflow change (ΔQ_{BB}) gradually increased over the LC period (Figure 4.8b). The year v2012 had an observed annual Q_{BB} (424 mm) that was 30 mm lower than the expected streamflow. For the following two years, v2013 and v2014 the observed streamflow was higher than the expected streamflow by 17 mm and 61 mm, respectively. The study catchment and the reference

catchment experienced identical climate conditions, such as temperature, precipitation, and wind, and the relative characteristics between the two catchments were removed in the calibration procedure, therefore ΔQ_{BB} must result from the changes in the study catchment, i.e. changing forest activity.

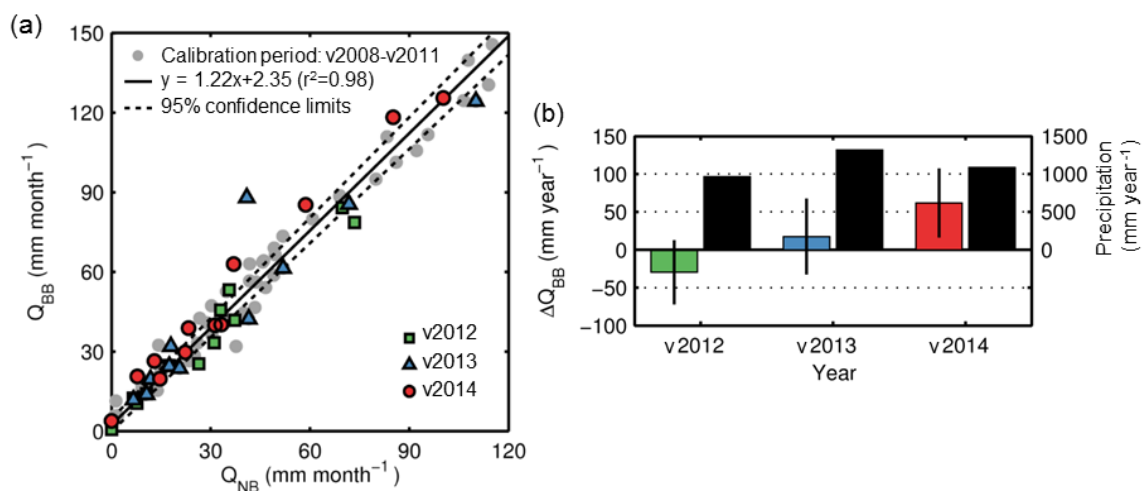


Figure 4.8. Scatter plots for the paired-catchment approach. (a) Gray-filled circles are the monthly streamflow during calibration period (2008-2011) and LC period (2012-2014). Each year in LC period was plotted in different colored symbol: 2012 in green rectangle, 2013 in blue triangle, and 2014 in red circle (b) HWA-induced annual streamflow change in Q_{BB} (ΔQ_{BB}) in vegetation years in colored bars with the confidence interval vertical bars. Black bars are annual precipitation in the vegetation year.

4.4. Discussion and conclusion

From the infestation growth rate, $15.86\% \text{ year}^{-1}$ in average from 2009 to 2014, the initial instant of the HWA infestation at the study site can be estimated as between 2007 and 2008, which is also estimated as the start of the loss of xylem conductivity in a hemlock stand based on the summertime-mean ET_{day} flux ($t_0=2008$ in Figure 4.1). The average annual mortality rate after the infestation (2009-2014), $1.86\% \text{ year}^{-1}$, was close to the mortality, $2\% \text{ year}^{-1}$, reported from another long-term (1993-2012) HWA monitoring site along the Delaware River in between Pennsylvania and New Jersey, where HWA was first reported in 1989 (Eschtruth et al., 2013). There was no noticeable overall hemlock mortality attributed to the HWA infestation, although small stands ($DBH < 15\text{cm}$) started to show a small mortality increase from pre-HWA rate at $4\% \text{ year}^{-1}$ to post-HWA rate at $5.69\% \text{ year}^{-1}$. Still, mortality after the HWA infestation in Harvard Forest was much lower than other eastern hemlock mortality studies (stand die-off within 4 years in Connecticut (McClure, 1991) or $20\% \text{ year}^{-1}$ across southern New England (D. A. Orwig, Foster, & Mausel, 2002)). Since mortality varied significantly by year because of the interannual variations in the environmental conditions such as winter temperature and summer drought, more frequent periodic mortality monitoring needs to be followed. Eschtruth et al. (2013), for example, reported the greatest mortality ($5\% \text{ year}^{-1}$) in 2003-04 and the least mortality ($0\% \text{ year}^{-1}$) in 2006-07.

LAI was not measured in August 2014, but it can be retrieved by combining LAI measurement in August 2008 and 2009 with vigor index data in 2009 and 2014. Overall stand annual-mean vigor index was 1.45 in 2009 and 1.95 in 2014 (Table 4.1), meaning

that foliar loss was about 12.5-25% in 2009 and 25-50% in 2014. This indicates that foliar loss from 2009 to 2014 was between 0-43%. Therefore, LAI in August 2014 can be estimated as 2.4-4.3 (mean as 3.4) based on 2008 LAI data, and 2.7-4.8 (mean as 3.75) based on 2009 LAI. These were very rough estimates, but very close to the simulated LAI_{LC} in 2014, 3.73.

The annual streamflow changes by the HWA infestation in v2014 (model estimates of 81 mm as well as the paired-catchment approach of 62 mm) were comparable with the previous studies that every 10% change (decrease) of coniferous cover in a catchment would cause 40 mm change (increase) of annual streamflow (Bosch et al., 1982; Brown et al., 2005). Assuming that the vigor condition of the sampled hemlocks represent the overall condition of the hemlock-dominated coniferous forests in the BB catchment, the hemlock-dominated coniferous forests which takes 44% of the BB catchment area having the vigor index of 1.95 in 2014 which indicates that the foliar area loss was between 25-50% give us a rough estimation that 11-22% of the coniferous forests in the BB catchment were lost. This cover loss is equivalent to 44-88 mm of streamflow increase, which encompass both estimates from the model and the paired-catchment approach.

The amount of precipitation in early 2011 and 2014 was very close, but the high snowmelt peak flow only in March 2014 might result from the loss of canopy cover (Bearup et al., 2014). The loss of canopy cover might result in snow intercepted on the canopy decreased while snowpack on the ground increased. Since snowpack on the ground has lower sublimation rates than the snowpack intercepted by the canopy, more

snowmelt flow might be generated from the increased snowpack on the ground (Adams et al., 2012). However, it is also possible that the solar radiation increased on the ground through the canopy gap might promote the snowpack to sublimate rather than gradually melt, yet there was no noticeable change in the observed ET_{day} in early 2014 (Figure 4.5b). The simulated LAI in March decreased from 3.8 in 2011 to 3.3 in 2014, which would result in the transmitted solar radiation increased by 5%, estimated using Beer's law with the light extinction coefficient as 0.5.

Future research should continue to integrate additional representations of the key processes into the process-based RHESSys model including additional climate-dependent HWA dynamics, the loss of carbohydrate transport in phloem and decrease of non-structural carbon by HWA, and the resultant mortality (Dietze et al., 2014; Tague et al., 2013). The simulated estimates have to be extensively evaluated against field measurements to further improve the representations of the processes. This study represents the first step in modeling and estimating streamflow variability in response to future climate change and insect infestation, and provides initial quantitative references for water resource management in hemlock-dominating catchments.

Chapter 5. Conclusion

“All vegetated land surfaces are heterogeneous at some scale.” - Lloyd (1995)

Mixed forests are composed of multiple plant types (e.g. deciduous forests, coniferous forests, and woody wetlands) that have profoundly different physiological behaviors. Each individual plant continuously competes with others for the energy (solar radiation) and nutrients (water, carbon, and nitrogen) available in the given climate (e.g. temperature and atmospheric vapor pressure deficit) to order to minimize any growth-stress at short time-scales (Kerkhoff et al., 2004; Mackay, 2001), and to optimize plant structure at the plot scale (Hwang et al., 2009; Nemani et al., 1989). At the catchment scale or larger spatial scales, plant composition and distribution are adjusted to maximize biomass productivity (Arris et al., 1994; Caylor et al., 2004; Mackay, 2001). Therefore, the current plant types and their spatial distribution in a mixed forest are the optimized equilibrium state of the ecosystem which as undergone climatic changes and additional disturbances (e.g. fire, harvest, invasive insect infestations) in the past.

After the overwhelming climate changes of the past few decades (e.g. increase of atmospheric CO₂ level by 30 ppm and increase of temperature by 1.3°F; NOAA, 2013; Walsh et al., 2014), mixed forests are predicted to face even more significant climate changes in the upcoming years (a further increase of temperature by 3-10°F, and two times more frequent heavy rainfall events; Walsh et al., 2014) as well as more frequent regional invasive insect outbreaks (Dale et al., 2001). In the process of achieving

“another optimized state” under these changing conditions, the exchange of carbon and water between the mixed forests and the atmosphere is expected to change dynamically, which would influence our daily lives both directly (e.g. fresh water yield from mixed forested catchments) and indirectly (e.g. positive and/or negative feedbacks to the atmospheric CO₂ level and the atmospheric water vapor that strongly drive climate changes).

In order to predict future behavior of a mixed forest, we first have to fully understand the current characteristics of the mixed forest at different spatio-temporal scales. Three related studies have been undertaken during this dissertation research to address the dynamics in carbon and water cycling in a mixed forest, using the Harvard Forest in the northeastern United States, which is experiencing both long-term gradual climate change and an invasive insect outbreak, as a study area.

5.1. Dissertation results

In chapter two, we first analyzed whether eddy-flux data (focusing on gross primary productivity (GPP) estimates) from the EMS-tower (US-Ha1) in the Harvard Forest fully represents the plant density and distribution at the spatial scales of ecosystem models and of remote sensing estimates with the moderate resolutions of 1 km and 1.5 km. Seasonal footprints of the EMS tower for 17 years (1992-2008) were estimated using a footprint climatology. There were found to be profound interannual as well as seasonal variations in the extents and shapes of the tower footprints from SW and NW directions where most of ground samples have traditionally been collected, especially during the

spring green-up period (April-May) which can experience strong winds from the north and the east. Based on a semivariogram analysis and window analysis using the EVI (enhanced vegetation index) retrieved from all the available fine resolution (30 m) Landsat TM/ETM+ data from 1992 to 2008, it was found that the plant density within the tower footprints can appropriately represent the mean magnitude and variation of plant density at the scale of 1 km throughout all periods (green-up, mature, and senescence), but does not represent plant density distribution at the 1.5 km scale during the mature period. However, we found that the GPP estimates at the EMS-tower during the mature period cannot be explained by the EVI values at either the 1 km scale or at the footprint scale ($r^2=0.00-0.02$). By calculating plant type compositions within the footprints from 1999 to 2008 using National Land Cover Dataset (NLCD) 2001 and 2006, we found that about 50% of the interannual anomalies in the mature period GPP estimates from 1999 to 2008 can be explained by the proportion of the surrounding evergreen coniferous forest (ENF) stands contributed to the flux measured at the tower ($r^2=0.48$, $p<0.05$). Every 1% decrease of ENF in the footprint resulted in the increase of the GPP estimates by 20 gC m^{-2} .

In chapter three, a spatially-distributed process-based ecohydrological model (RHESSys) was implemented to simulate carbon and water cycles in the two headwater catchments of this mixed forest from 1992 to 2008. The simulated estimates of carbon and water cycles of the two dominant forest types in the study site, deciduous forest and coniferous forest, were evaluated at two different spatial scales: plot scale and catchment

scale. The model simulated estimates had a good correlation with the observations: soil respiration ($r=0.75-0.79$), LAI ($r=0.93$), daily GPP ($r=0.89-0.93$), monthly GPP ($r=0.98$), annual GPP ($r=0.76$), daily ET ($0.88-0.9$), monthly streamflow ($r=0.84-0.9$), and annual streamflow ($r=0.89-0.93$). The GPP increase of the deciduous forest for the seventeen years was well captured in the simulated GPP, but interannual variations, especially significant reductions in 1998 and 2005, were not well simulated. The annual GPP of the deciduous forest has increased significantly ($\sim 30 \text{ gC m}^{-2}$ per year), six times more than that of the coniferous forest even though both forests had experienced identical climate change for the past two decades. On the other hand, the annual ET of both forests was very conservative for the same period, not varying as much as the annual GPP, and only increasing at a significant but small rates (4-7 mm per year).

In chapter four, we assessed the impact of the Hemlock Woolly Adelgid (HWA) infestation on the streamflow of the catchment where the hemlock-dominated coniferous forests cover half the area. Based on tree inventory data in 2009 and 2014, we confirmed that the HWA infestation increased by 80% in the study catchment within the five years and the foliar area was lost up to 43%. There was still no sign of significant mortality of the overall hemlock stands, although the small stands ($\text{DBH} < 15 \text{ cm}$) had started to show mortality attributed to the HWA infestation. We represented the loss of water conductivity (LC) in the xylem of infested hemlocks using a probability function (Weibull function) that was calibrated using the evapotranspiration (ET) flux measured at the hemlock-tower (US-Ha2), and implemented the LC function as a stress factor of

controlling stomata conductance. The simulated LAI and ET from RHESSys model with the LC function adequately captured the observed reductions in the field-measured leaf area index (LAI) and the ET flux. We found that annual streamflow from the catchment that is covered by the hemlock-dominated forests by 44% of its area has increased by 81 mm in 2014 compared to the simulated streamflow in the scenario of not having the HWA infestation, and also by 61 mm compared to the annual streamflow from the catchment that contains less hemlock-dominated forests (25%). Thus, we concluded that the HWA infestation has resulted in a gradual increase of annual streamflow (especially significant increase during heavy precipitation events), which is consistent with the previous studies about the impact of land cover change on the streamflow reporting that increase of annual streamflow by 40 mm for the loss of coniferous forest cover by 10 %.

These three related studies have greatly expanded our understanding of the role of conifer trees in mixed forest ecosystems and the dynamic changes that can occur when the proportion of evergreen needle-leaf forest is diminished due to climate change and invasive insect attacks. By successfully parameterizing the spatial-temporal ecohydrologic model RHESSYS for Harvard Forest (the LTER with the longest tower and field records and currently experiencing the initial stages of an insect infestation), we have been able to establish a framework to investigate the impact of these changes on mixed forest composition into the future.

5.2. Future Research

Thus the implementation of RHESSYS at Harvard Forest and the results of this dissertation research have raised additional questions and identified fruitful areas of investigation for the future. The correlation between plant type proportions within the tower footprints and the interannual flux anomalies observed at other flux towers located in mixed forests needs to be addressed, especially for those flux towers located in very heterogeneous landscapes and providing long-term flux records. Only after fully understanding how the mix of plant types actually contributes to the measured flux, should we use such flux measurements to calibrate and validate plant type functions in both ecosystem models and climate models.

The HWA infestation in the Harvard Forest has just began and will bring profound changes in the forest composition. Continuous and consistent monitoring of hemlock mortality and tree vigor condition will improve our understanding of temporal dynamics caused by the HWA infestation. Additional observations of the hydrological processes and of micro-environmental conditions such as soil moisture, snowpack amount, and understory light level in the HWA study plots will continue to be necessary to refine the underlying processes in ecosystem models. If possible, installation of a second streamflow gauge at a catchment near to Harvard Forest, one which does not have eastern hemlocks within its area, would provide further opportunities to explicitly explore the impact of the HWA on the streamflow by comparing the data from the hemlock-free gauge with the one in the Harvard Forest.

Our research results for Harvard Forest (and the northeastern mixed forests it typifies) are of particular interest as one of the core towers of domain 1 of the National Ecological Observatory Network (NEON) has recently been installed in the Harvard Forest, very close to the EMS tower (42.5369°N, 72.17266°W). The NEON program will strive to collect data at all of their core locations for a climatologically significant 30 year period. The data from this Harvard Forest NEON domain are just becoming available and it is highly likely that the flux measurements collected by the NEON tower will be similarly dependent on the landscape around the tower and impacted by the changes to the landscape as the HWA infestation increases hemlock mortality over the entire forest.

BIBLIOGRAPHY

- Adams, H. D., Luce, C. H., Breshears, D. D., Allen, C. D., Weiler, M., Hale, V. C., ... Huxman, T. E. (2012). Ecohydrological consequences of drought- and infestation-triggered tree die-off: insights and hypotheses. *Ecohydrology*, 5(2), 145–159. <http://doi.org/10.1002/eco.233>
- Amiro, B. D. (1998). Footprint climatologies for evapotranspiration in a boreal catchment. *Agricultural and Forest Meteorology*, 90(3), 195–201. [http://doi.org/10.1016/S0168-1923\(97\)00096-8](http://doi.org/10.1016/S0168-1923(97)00096-8)
- Arnold, J. G., Srinivasan, R., Muttiah, R. S., & Williams, J. R. (1998). Large Area Hydrologic Modeling and Assessment Part I: Model Development. *Journal of the American Water Resources Association*, 34(1), 73–89. <http://doi.org/10.1111/j.1752-1688.1998.tb05961.x>
- Arris, L. L., & Eagleson, P. S. (1994). A water use model for locating the boreal/deciduous forest ecotone in eastern North America. *Water Resources Research*, 30(1), 1–9. <http://doi.org/10.1029/93WR02746>
- Baldocchi, D. D. (2003). Assessing the eddy covariance technique for evaluating carbon dioxide exchange rates of ecosystems: past, present and future. *Global Change Biology*, 9(4), 479–492. <http://doi.org/10.1046/j.1365-2486.2003.00629.x>
- Baldocchi, D. D., Hincks, B. B., & Meyers, T. P. (1988). Measuring Biosphere-Atmosphere Exchanges of Biologically Related Gases with Micrometeorological Methods. *Ecology*, 69(5), 1331. <http://doi.org/10.2307/1941631>
- Band, L. E., Hwang, T., Hales, T. C., Vose, J., & Ford, C. R. (2012). Ecosystem processes at the watershed scale: Mapping and modeling ecohydrological controls of landslides. *Geomorphology*, 137(1), 159–167. <http://doi.org/10.1016/j.geomorph.2011.06.025>
- Band, L. E., Patterson, P., Nemani, R. R., & Running, S. W. (1993). Forest ecosystem processes at the watershed scale: incorporating hillslope hydrology. *Agricultural and Forest Meteorology*, 63(1-2), 93–126. [http://doi.org/10.1016/0168-1923\(93\)90024-C](http://doi.org/10.1016/0168-1923(93)90024-C)
- Barford, C. C., Wofsy, S. C., Goulden, M. L., Munger, W. J., Pyle, E. H., Urbanski, S., ... Moore, K. (2001). Factors controlling long- and short-term sequestration of atmospheric CO₂ in a mid-latitude forest. *Science (New York, N.Y.)*, 294(5547), 1688–91. <http://doi.org/10.1126/science.1062962>

- Baron, J. S., Hartman, M. D., Band, L. E., & Lammers, R. B. (2000). Sensitivity of a high-elevation rocky mountain watershed to altered climate and CO₂. *Water Resources Research*, 36(1), 89–99. <http://doi.org/10.1029/1999WR900263>
- Bartlett, M. K., Ollinger, S. V., Hollinger, D. Y., Wicklein, H. F., & Richardson, A. D. (2011). Canopy-scale relationships between foliar nitrogen and albedo are not observed in leaf reflectance and transmittance within temperate deciduous tree species. *Botany*, 89(7), 491–497. <http://doi.org/10.1139/b11-037>
- Bates, C. G., & Henry, A. J. (1928). Second Phase of Streamflow Experiment at Wagon Wheel Gap, Colo. *Monthly Weather Review*, 56(3), 79–80. [http://doi.org/10.1175/1520-0493\(1928\)56<79:SPOSEA>2.0.CO;2](http://doi.org/10.1175/1520-0493(1928)56<79:SPOSEA>2.0.CO;2)
- Battles, J. J., Robards, T., Das, A., Waring, K., Gilles, J. K., Biging, G., & Schurr, F. (2007). Climate change impacts on forest growth and tree mortality: A data-driven modeling study in the mixed-conifer forest of the Sierra Nevada, California. *Climatic Change*, 87(1 SUPPL). <http://doi.org/10.1007/s10584-007-9358-9>
- Bearup, L. A., Maxwell, R. M., Clow, D. W., & McCray, J. E. (2014). Hydrological effects of forest transpiration loss in bark beetle-impacted watersheds. *Nature Climate Change*, 4(6), 481–486. <http://doi.org/10.1038/nclimate2198>
- Bechtold, W. A., Patterson, P. L., & Editors. (2005). *The enhanced Forest Inventory and Analysis program - national sampling design and estimation procedures. Gen. Tech. Rep. SRS-80. Asheville, NC: U.S. Department of Agriculture, Forest Service, Southern Research Station* (Vol. 080). Retrieved from <http://www.treesearch.fs.fed.us/pubs/20371>
- Belmecheri, S., Maxwell, R. S., Taylor, A. H., Davis, K. J., Freeman, K. H., & Munger, W. J. (2014). Tree-ring $\delta^{13}\text{C}$ tracks flux tower ecosystem productivity estimates in a NE temperate forest. *Environmental Research Letters*, 9(7), 074011. <http://doi.org/10.1088/1748-9326/9/7/074011>
- Bethlahmy, N. (1974). More streamflow after a bark beetle epidemic. *Journal of Hydrology*, 23(3-4), 185–189. [http://doi.org/10.1016/0022-1694\(74\)90001-8](http://doi.org/10.1016/0022-1694(74)90001-8)
- Beven, K. J., & Binley, A. (1992). The future of distributed models: Model calibration and uncertainty prediction. *Hydrological Processes*, 6(3), 279–298. <http://doi.org/10.1002/hyp.3360060305>
- Beven, K. J., & Freer, J. (2001). Equifinality, data assimilation, and uncertainty estimation in mechanistic modelling of complex environmental systems using the GLUE methodology. *Journal of Hydrology*, 249(1-4), 11–29. [http://doi.org/10.1016/S0022-1694\(01\)00421-8](http://doi.org/10.1016/S0022-1694(01)00421-8)

- Boon, S. (2012). Snow accumulation following forest disturbance. *Ecohydrology*, 5(3), 279–285. <http://doi.org/10.1002/eco.212>
- Boose, E. (2001). Fisher Meteorological Station at Harvard Forest since 2001. Harvard Forest Data Archive: HF001. Retrieved October 9, 2014, from <http://harvardforest.fas.harvard.edu:8080/exist/xquery/data.xq?id=hf001>
- Boose, E. (2007). Prospect Hill Hydrological Stations at Harvard Forest since 2005. Harvard Forest Data Archive: HF070. Retrieved October 10, 2014, from <http://harvardforest.fas.harvard.edu:8080/exist/xquery/data.xq?id=hf070>
- Boose, E., & Gould, E. (1999). Shaler Meteorological Station at Harvard Forest 1964-2002. Harvard Forest Data Archive: HF000. Retrieved October 9, 2014, from <http://harvardforest.fas.harvard.edu:8080/exist/xquery/data.xq?id=hf000>
- Bosch, J. M., & Hewlett, J. D. (1982). A review of catchment experiments to determine the effect of vegetation changes on water yield and evapotranspiration. *Journal of Hydrology*, 55(1-4), 3–23. [http://doi.org/10.1016/0022-1694\(82\)90117-2](http://doi.org/10.1016/0022-1694(82)90117-2)
- Brantley, S. T., Ford, C. R., & Vose, J. M. (2013). Future species composition will affect forest water use after loss of eastern hemlock from southern Appalachian forests. *Ecological Applications*, 23(4), 777–790. <http://doi.org/10.1890/12-0616.1>
- Brantley, S. T., Miniati, C. F., Elliott, K. J., Laseter, S. H., & Vose, J. M. (2014). Changes to southern Appalachian water yield and stormflow after loss of a foundation species. *Ecohydrology*, 8, 518–528. <http://doi.org/10.1002/eco.1521>
- Brown, A. E., Zhang, L., McMahon, T. A., Western, A. W., & Vertessy, R. A. (2005). A review of paired catchment studies for determining changes in water yield resulting from alterations in vegetation. *Journal of Hydrology*, 310(1-4), 28–61. <http://doi.org/10.1016/j.jhydrol.2004.12.010>
- Cao, M., & Woodward, F. I. (1998). Dynamic responses of terrestrial ecosystem carbon cycling to global climate change. *Nature*, 393(6682), 249–252. <http://doi.org/10.1038/30460>
- Carroll, S. S., & Cressie, N. (1996). A comparison of geostatistical methodologies used to estimate snow water equivalent. *Journal of the American Water Resources Association*, 32(2), 267–278. <http://doi.org/10.1111/j.1752-1688.1996.tb03450.x>
- Caylor, K. K., Scanlon, T. M., & Rodriguez-Iturbe, I. (2004). Feasible optimality of vegetation patterns in river basins. *Geophysical Research Letters*, 31(13), 4–7. <http://doi.org/10.1029/2004GL020260>

- Chasmer, L., Kljun, N., Hopkinson, C., Brown, S., Milne, T., Giroux, K., ... Petrone, R. (2011). Characterizing vegetation structural and topographic characteristics sampled by eddy covariance within two mature aspen stands using lidar and a flux footprint model: Scaling to MODIS. *Journal of Geophysical Research: Biogeosciences*, *116*, 1–19. <http://doi.org/10.1029/2010JG001567>
- Chen, B., Black, T. A., Coops, N. C., Hilker, T., Trofymow, J. a., & Morgenstern, K. (2009). Assessing tower flux footprint climatology and scaling between remotely sensed and eddy covariance measurements. *Boundary-Layer Meteorology*, *130*, 137–167. <http://doi.org/10.1007/s10546-008-9339-1>
- Chen, B., Coops, N. C., Fu, D., Margolis, H. A., Amiro, B. D., Black, T. A., ... Wofsy, S. C. (2012). Characterizing spatial representativeness of flux tower eddy-covariance measurements across the Canadian Carbon Program Network using remote sensing and footprint analysis. *Remote Sensing of Environment*, *124*, 742–755. <http://doi.org/10.1016/j.rse.2012.06.007>
- Chen, B., Zhang, H., Coops, N. C., Fu, D., Worthy, D. E. J., Xu, G., & Black, T. A. (2013). Assessing scalar concentration footprint climatology and land surface impacts on tall-tower CO₂ concentration measurements in the boreal forest of central Saskatchewan, Canada. *Theoretical and Applied Climatology*, *118*, 115–132. <http://doi.org/10.1007/s00704-013-1038-2>
- Chen, H., Harmon, M. E., Griffiths, R. P., & Hicks, W. (2000). Effects of temperature and moisture on carbon respired from decomposing woody roots. *Forest Ecology and Management*, *138*(1-3), 51–64. [http://doi.org/10.1016/S0378-1127\(00\)00411-4](http://doi.org/10.1016/S0378-1127(00)00411-4)
- Chen, J. ., Liu, J., Cihlar, J., & Goulden, M. . (1999). Daily canopy photosynthesis model through temporal and spatial scaling for remote sensing applications. *Ecological Modelling*. [http://doi.org/10.1016/S0304-3800\(99\)00156-8](http://doi.org/10.1016/S0304-3800(99)00156-8)
- Christensen, L., Tague, C. L., & Baron, J. S. (2008). Spatial patterns of simulated transpiration response to climate variability in a snow dominated mountain ecosystem. *Hydrological Processes*, *22*(18), 3576–3588. <http://doi.org/10.1002/hyp.6961>
- Cohen, W. B., Turner, D. P., Gower, S. T., & Running, S. W. (2006). BigFoot Land Cover Surfaces for North and South American Sites, 2000–2003. Data set. Available on-line [<http://www.daac.ornl.gov>] from Oak Ridge National Laboratory Distributed Active Archive Center, Oak Ridge, Tennessee, U.S.A.
- Costa, S., & Onken, B. (2006). *Standardizing Sampling for Detection and Monitoring of Hemlock Woolly Adelgid in Eastern Hemlock Forests*. FHTET-2006-16. USDA Forest Service, Morgantown, West Virginia.

- Cramer, W., Bondeau, A., Woodward, F. I., Prentice, I. C., Betts, R. a., Brovkin, V., ... Young-Molling, C. (2001). Global response of terrestrial ecosystem structure and function to CO₂ and climate change: Results from six dynamic global vegetation models. *Global Change Biology*, 7(4), 357–373. <http://doi.org/10.1046/j.1365-2486.2001.00383.x>
- Curran, P. (1988). The semi-variogram in remote sensing: an introduction. *Remote Sensing of Environment*, 507(24), 493–507. [http://doi.org/10.1016/0034-4257\(88\)90021-1](http://doi.org/10.1016/0034-4257(88)90021-1)
- Currie, W. S., Aber, J. D., McDowell, W. H., Boone, R. D., & Magill, A. H. (1996). Vertical transport of dissolved organic C and N under long-term N amendments in pine and hardwood forests. *Biogeochemistry*, 35(3), 471–505. <http://doi.org/10.1007/BF02183037>
- Dale, V. H., Joyce, L. A., McNulty, S., Neilson, R. P., Ayres, M. P., Flannigan, M. D., ... Wotton, B. M. (2001). Climate Change and Forest Disturbances. *BioScience*, 51(9), 723. [http://doi.org/10.1641/0006-3568\(2001\)051\[0723:CCAFD\]2.0.CO;2](http://doi.org/10.1641/0006-3568(2001)051[0723:CCAFD]2.0.CO;2)
- Davidson, E. A., Janssens, I. A., & Luo, Y. (2006). On the variability of respiration in terrestrial ecosystems: moving beyond Q₁₀. *Global Change Biology*, 12(2), 154–164. <http://doi.org/10.1111/j.1365-2486.2005.01065.x>
- Davidson, E. A., Richardson, A. D., Savage, K. E., & Hollinger, D. Y. (2006). A distinct seasonal pattern of the ratio of soil respiration to total ecosystem respiration in a spruce-dominated forest. *Global Change Biology*, 12(2), 230–239. <http://doi.org/10.1111/j.1365-2486.2005.01062.x>
- Davidson, E. A., & Savage, K. E. (1999). Soil Respiration, Temperature and Moisture at Harvard Forest EMS Tower since 1995. Harvard Forest Data Archive: HF006. Retrieved October 25, 2014, from <http://harvardforest.fas.harvard.edu:8080/exist/xquery/data.xq?id=hf006>
- Davis, J. C. (1986). *Statistics and Data Analysis in Geology* (2nd ed.). New York: Wiley. Retrieved from http://books.google.com/books/about/Statistics_and_Data_Analysis_in_Geology.html?id=jexrOI90RXUC&pgis=1
- Detto, M., Montaldo, N., Albertson, J. D., Mancini, M., & Katul, G. (2006). Soil moisture and vegetation controls on evapotranspiration in a heterogeneous Mediterranean ecosystem on Sardinia, Italy. *Water Resources Research*, 42, 1–16. <http://doi.org/10.1029/2005WR004693>

- Dietze, M. C., & Matthes, J. H. (2014). A general ecophysiological framework for modeling the impact of pests and pathogens on forest ecosystems. *Ecology Letters*, 17(11), 1418–1426. <http://doi.org/10.1111/ele.12345>
- Dillen, S. Y., de Beeck, M. O., Hufkens, K., Buonanduci, M., & Phillips, N. G. (2012). Seasonal patterns of foliar reflectance in relation to photosynthetic capacity and color index in two co-occurring tree species, *Quercus rubra* and *Betula papyrifera*. *Agricultural and Forest Meteorology*, 160, 60–68. <http://doi.org/10.1016/j.agrformet.2012.03.001>
- Dingman, S. L. (2009). *Physical Hydrology* (2nd ed.). Long Grove, Illinois: Waveland Press, Inc.
- Domec, J.-C., Rivera, L. N., King, J. S., Peszlen, I., Hain, F., Smith, B., & Frampton, J. (2013). Hemlock woolly adelgid (*Adelges tsugae*) infestation affects water and carbon relations of eastern hemlock (*Tsuga canadensis*) and Carolina hemlock (*Tsuga caroliniana*). *The New Phytologist*, 199(2), 452–63. <http://doi.org/10.1111/nph.12263>
- Eakins, B. W., & Sharman, G. F. (2010). Volumes of the World's Oceans from ETOPO1, NOAA National Geophysical Data Center, Boulder, CO. Retrieved January 12, 2015, from http://www.ngdc.noaa.gov/mgg/global/etopo1_ocean_volumes.html
- Eckman, R. M. (1994). Re-examination of empirically derived formulas for horizontal diffusion from surface sources. *Atmospheric Environment*, 28(2), 265–272. [http://doi.org/10.1016/1352-2310\(94\)90101-5](http://doi.org/10.1016/1352-2310(94)90101-5)
- Ellison, A. M., Plotkin, A. B., Foster, D. R., & Orwig, D. A. (2010). Experimentally testing the role of foundation species in forests: the Harvard Forest Hemlock Removal Experiment. *Methods in Ecology and Evolution*, 1(2), 168–179. <http://doi.org/10.1111/j.2041-210X.2010.00025.x>
- Enquist, B. J., West, G. B., Charnov, E. L., & Brown, J. H. (1999). Allometric scaling of production and life-history variation in vascular plants. *Nature*, 401(6756), 907–911. <http://doi.org/10.1038/44819>
- Eschtruth, A. K., Evans, R. A., & Battles, J. J. (2013). Patterns and predictors of survival in *Tsuga canadensis* populations infested by the exotic pest *Adelges tsugae*: 20 years of monitoring. *Forest Ecology and Management*, 305, 195–203. <http://doi.org/10.1016/j.foreco.2013.05.047>
- Etheridge, D. M., Steele, L. P., Langenfelds, R. L., Francey, R. J., Barnola, J.-M., & Morgan, V. I. (1996). Natural and anthropogenic changes in atmospheric CO₂ over

- the last 1000 years from air in Antarctic ice and firn. *Journal of Geophysical Research*, 101(D2), 4115–4128. <http://doi.org/10.1029/95JD03410>
- Evans, A. M., & Gregoire, T. G. (2007). A geographically variable model of hemlock woolly adelgid spread. *Biological Invasions*, 9(4), 369–382. <http://doi.org/10.1007/s10530-006-9039-z>
- Evans, R. A. (2004). Hemlock woolly adelgid and the disintegration of eastern hemlock ecosystems. *Park Science*, 22(2), 53–56. Retrieved from <http://www.nature.nps.gov/ParkScience/index.cfm?ArticleID=122&Page=1>
- Falge, E., Baldocchi, D. D., Olson, R., Anthoni, P., Aubinet, M., Bernhofer, C., ... Wofsy, S. C. (2001). Gap filling strategies for defensible annual sums of net ecosystem exchange. *Agricultural and Forest Meteorology*, 107(1), 43–69. [http://doi.org/10.1016/S0168-1923\(00\)00225-2](http://doi.org/10.1016/S0168-1923(00)00225-2)
- Farquhar, G. D., & Caemmerer, S. von. (1982). *Modelling of Photosynthetic Response to Environmental Conditions in Physiological Plant Ecology II*. (O. L. Lange, P. S. Nobel, C. B. Osmond, & H. Ziegler, Eds.). Berlin, Heidelberg: Springer Berlin Heidelberg. <http://doi.org/10.1007/978-3-642-68150-9>
- Farquhar, G. D., von Caemmerer, S., & Berry, J. A. (1980). A biochemical model of photosynthetic CO₂ assimilation in leaves of C₃ species. *Planta*, 149(1), 78–90. <http://doi.org/10.1007/BF00386231>
- Field, C., Berry, J. A., & Mooney, H. A. (1982). A portable system for measuring carbon dioxide and water vapour exchange of leaves. *Plant, Cell & Environment*, 5(2), 179–186. <http://doi.org/10.1111/1365-3040.ep11571607>
- Finzi, A. C., Raymer, P. C. L., Giasson, M.-A., & Orwig, D. A. (2014). Net primary production and soil respiration in New England hemlock forests affected by the hemlock woolly adelgid. *Ecosphere*, 5(8), art98. <http://doi.org/10.1890/ES14-00102.1>
- Forbrich, I., Kutzbach, L., Wille, C., Becker, T., Wu, J., & Wilmking, M. (2011). Cross-evaluation of measurements of peatland methane emissions on microform and ecosystem scales using high-resolution landcover classification and source weight modelling. *Agricultural and Forest Meteorology*, 151(7), 864–874. <http://doi.org/10.1016/j.agrformet.2011.02.006>
- Ford, C. R., & Vose, J. M. (2007). TSUGA CANADENSIS (L.) CARR. Mortality Will Impact Hydrologic Processes In Southern Appalachian Forest Ecosystems. *Ecological Applications*, 17(4), 1156–1167. <http://doi.org/10.1890/06-0027>

- Foster, D., & Plotkin, A. B. (1999). Hemlock Mapped Tree Plot at Harvard Forest since 1990. Harvard Forest Data Archive: HF031. Retrieved from <http://harvardforest.fas.harvard.edu:8080/exist/apps/datasets/showData.html?id=hf031>
- Foster, D. R., & Plotkin, A. B. (1999). Hemlock Mapped Tree Plot at Harvard Forest since 1990. Harvard Forest Data Archive: HF031. Retrieved from <http://harvardforest.fas.harvard.edu:8080/exist/apps/datasets/showData.html?id=hf031>
- Gao, Y., Yu, G., Yan, H., Zhu, X., Li, S., Wang, Q., ... Shi, P. (2014). A MODIS-based Photosynthetic Capacity Model to estimate gross primary production in Northern China and the Tibetan Plateau. *Remote Sensing of Environment*, *148*, 108–118. <http://doi.org/10.1016/j.rse.2014.03.006>
- Gonda-King, L., Gómez, S., Martin, J. L., Orians, C. M., & Preisser, E. L. (2014). Tree responses to an invasive sap-feeding insect. *Plant Ecology*, *215*(3), 297–304. <http://doi.org/10.1007/s11258-014-0298-y>
- Gonda-King, L., Radville, L., & Preisser, E. L. (2012). False Ring Formation in Eastern Hemlock Branches: Impacts of Hemlock Woolly Adelgid and Elongate Hemlock Scale. *Environmental Entomology*, *41*(3), 523–531. <http://doi.org/10.1603/EN11227>
- Goulden, M. L., Munger, W. J., Fan, S.-M., Daube, B. C., & Wofsy, S. C. (1996). Measurements of carbon sequestration by long-term eddy covariance: Methods and a critical evaluation of accuracy. *Global Change Biology*, *2*, 169–182. <http://doi.org/10.1111/j.1365-2486.1996.tb00070.x>
- GRASS Development Team. (2012). Geographic Resources Analysis Support System (GRASS) Software. Open Source Geospatial Foundation Project. Retrieved from <http://grass.osgeo.org>
- Gryning, S. E., Holtslag, A. A. M., Irwin, J. S., & Sivertsen, B. (1987). Applied dispersion modelling based on meteorological scaling parameters. *Atmospheric Environment* (1967). [http://doi.org/10.1016/0004-6981\(87\)90273-3](http://doi.org/10.1016/0004-6981(87)90273-3)
- Guardiola-Claramonte, M., Troch, P. a., Breshears, D. D., Huxman, T. E., Switanek, M. B., Durcik, M., & Cobb, N. S. (2011). Decreased streamflow in semi-arid basins following drought-induced tree die-off: A counter-intuitive and indirect climate impact on hydrology. *Journal of Hydrology*, *406*(3-4), 225–233. <http://doi.org/10.1016/j.jhydrol.2011.06.017>

- Hadley, J. L. (2003). Net Carbon Exchange of an Old-Growth Hemlock Forest at Harvard Forest HEM Tower since 2000. Harvard Forest Data Archive: HF103. Retrieved from <http://harvardforest.fas.harvard.edu:8080/exist/xquery/data.xq?id=hf103>
- Hadley, J. L. (2009a). Leaf Area Index at Harvard Forest HEM and LPH Towers since 1998. Harvard Forest Data Archive: HF150. Retrieved from <http://harvardforest.fas.harvard.edu:8080/exist/xquery/data.xq?id=hf150>
- Hadley, J. L. (2009b). Soil Respiration at Harvard Forest HEM and LPH Towers 1996-2007. Harvard Forest Data Archive: HF148. Retrieved November 4, 2014, from <http://harvardforest.fas.harvard.edu:8080/exist/xquery/data.xq?id=hf148>
- Hadley, J. L. (2009c). Soil Water Content at Harvard Forest HEM and LPH Towers 1998-2007. Harvard Forest Data Archive: HF153. Retrieved October 27, 2014, from <http://harvardforest.fas.harvard.edu:8080/exist/xquery/data.xq?id=hf153>
- Hadley, J. L., Kuzeja, P. S., Daley, M. J., Phillips, N. G., Mulcahy, T., & Singh, S. (2008). Water use and carbon exchange of red oak- and eastern hemlock-dominated forests in the northeastern USA: implications for ecosystem-level effects of hemlock woolly adelgid. *Tree Physiology*, 28(4), 615–627. <http://doi.org/10.1093/treephys/28.4.615>
- Hadley, J. L., & Schedlbauer, J. L. (2002). Carbon exchange of an old-growth eastern hemlock (*Tsuga canadensis*) forest in central New England. *Tree Physiology*, 22(15-16), 1079–1092. <http://doi.org/10.1093/treephys/22.15-16.1079>
- Harmel, R. D., Cooper, R. J., Slade, R. M., Haney, R. L., & Arnold, J. G. (2006). Cumulative uncertainty in measured streamflow and water quality data for small watersheds. *Transactions of the ASABE*, 49(3), 689–701. Retrieved from http://www.nrcs.usda.gov/Internet/FSE_DOCUMENTS/stelprdb1041618.pdf
- Hartmann, D. L., Tank, A. M. G. K., Rusticucci, M., Alexander, L. V., Brönnimann, S., Charabi, Y., ... Zhai, P. M. (2013). *Observations: Atmosphere and Surface*. In: *Climate Change 2013: The Physical Science Basis. Contribution of Working Group I to the Fifth Assessment Report of the Intergovernmental Panel on Climate Change* [Stocker, T.F., D. Qin, G.-K. Plattner, M. Tignor, S. Cambridge, United Kingdom and New York, NY, USA. Retrieved from http://www.climatechange2013.org/images/report/WG1AR5_Chapter02_FINAL.pdf
- Havill, N. P., Vieira, L. C., & Salom, S. M. (2014). Biology and Control of Hemlock Woolly Adelgid. USDA Forest Service Publication FHTET-2014-05. *USDA Forest Service Publication FHTET-2014-05*.
- Haylock, M. R., Hofstra, N., Klein Tank, a. M. G., Klok, E. J., Jones, P. D., & New, M. (2008). A European daily high-resolution gridded data set of surface temperature

- and precipitation for 1950-2006. *Journal of Geophysical Research: Atmospheres*, 113. <http://doi.org/10.1029/2008JD010201>
- Heinsch, F. A., Running, S. W., Kimball, J. S., Nemani, R. R., Davis, K. J., Bolstad, P. V., ... Flanagan, L. B. (2006). Evaluation of remote sensing based terrestrial productivity from MODIS using regional tower eddy flux network observations. *IEEE Transactions on Geoscience and Remote Sensing*, 44(7), 1908–1925. <http://doi.org/10.1109/TGRS.2005.853936>
- Hornbeck, J. W., Adams, M. B., Corbett, E. S., Verry, E. S., & Lynch, J. a. (1993). Long-term impacts of forest treatments on water yield: a summary for northeastern USA. *Journal of Hydrology*, 150(2-4), 323–344. [http://doi.org/10.1016/0022-1694\(93\)90115-P](http://doi.org/10.1016/0022-1694(93)90115-P)
- Huete, A. R., Didan, K., Miura, T., Rodriguez, E. ., Gao, X., & Ferreira, L. . (2002). Overview of the radiometric and biophysical performance of the MODIS vegetation indices. *Remote Sensing of Environment*, 83(1-2), 195–213. [http://doi.org/10.1016/S0034-4257\(02\)00096-2](http://doi.org/10.1016/S0034-4257(02)00096-2)
- Hwang, T. (2010). *Integration of Spatio-Temporal Vegetation Dynamics into a Distributed Ecohydrological Model: Application to Optimality Theory and Real-Time Watershed Simulations*. Ph.D dissertation, University of North Carolina at Chapel Hill.
- Hwang, T., Band, L. E., & Hales, T. C. (2009). Ecosystem processes at the watershed scale: Extending optimality theory from plot to catchment. *Water Resources Research*, 45(11), n/a–n/a. <http://doi.org/10.1029/2009WR007775>
- Hwang, T., Band, L. E., Hales, T. C., Miniati, C. F., Vose, J. M., Bolstad, P. V., ... Price, K. (2015). Simulating vegetation controls on hurricane-induced shallow landslides with a distributed ecohydrological model. *Journal of Geophysical Research: Biogeosciences*, 120(2), 361–378. <http://doi.org/10.1002/2014JG002824>
- Jahan, N., & Gan, T. Y. (2009). Modeling gross primary production of deciduous forest using remotely sensed radiation and ecosystem variables. *Journal of Geophysical Research*, 114, G04026. <http://doi.org/10.1029/2008JG000919>
- Jarvis, P. G. (1976). The Interpretation of the Variations in Leaf Water Potential and Stomatal Conductance Found in Canopies in the Field. *Philosophical Transactions of the Royal Society B: Biological Sciences*. <http://doi.org/10.1098/rstb.1976.0035>
- Jorgensen, R. N., & Lecznar, S. L. (1964). *Anatomy of hemlock ring shake associated with sapsucker injury. Res. Pap. NE-21. Upper Darby, PA: U. S. Department of*

Agriculture, Forest Service, Northeastern Forest Experiment Station. Retrieved from <http://www.treesearch.fs.fed.us/pubs/3838>

- Keenan, T. F., Davidson, E. A., Moffat, A. M., Munger, W., & Richardson, A. D. (2012). Using model-data fusion to interpret past trends, and quantify uncertainties in future projections, of terrestrial ecosystem carbon cycling. *Global Change Biology*, *18*(8), 2555–2569. <http://doi.org/10.1111/j.1365-2486.2012.02684.x>
- Keenan, T. F., Gray, J., Friedl, M. A., Toomey, M., Bohrer, G., Hollinger, D. Y., ... Richardson, A. D. (2014). Net carbon uptake has increased through warming-induced changes in temperate forest phenology. *Nature Climate Change*, *4*(7), 598–604. <http://doi.org/10.1038/nclimate2253>
- Keenan, T. F., Hollinger, D. Y., Bohrer, G., Dragoni, D., Munger, J. W., Schmid, H. P., & Richardson, A. D. (2013). Increase in forest water-use efficiency as atmospheric carbon dioxide concentrations rise. *Nature*, *499*(7458), 324–7. <http://doi.org/10.1038/nature12291>
- Kelly, A. E., & Goulden, M. L. (2008). Rapid shifts in plant distribution with recent climate change. *Proceedings of the National Academy of Sciences of the United States of America*, *105*(33), 11823–11826. <http://doi.org/10.1073/pnas.0802891105>
- Kerkhoff, A. J., Martens, S. N., & Milne, B. T. (2004). An ecological evaluation of Eagleson's optimality. *Water Resources Research*, *18*(3), 404–413. <http://doi.org/10.1111/j.0269-8463.2004.00844.x>
- Kerr, J. T., & Ostrovsky, M. (2003). From space to species: ecological applications for remote sensing. *Trends in Ecology & Evolution*, *18*(6), 299–305. [http://doi.org/10.1016/S0169-5347\(03\)00071-5](http://doi.org/10.1016/S0169-5347(03)00071-5)
- Kim, J., Guo, Q., Baldocchi, D. D., Leclerc, M., Xu, L., & Schmid, H. P. (2006). Upscaling fluxes from tower to landscape: Overlaying flux footprints on high-resolution (IKONOS) images of vegetation cover. *Agricultural and Forest Meteorology*, *136*(3-4), 132–146. <http://doi.org/10.1016/j.agrformet.2004.11.015>
- Klemes, V. (1986). Operational testing of hydrological simulation models. *Hydrological Sciences Journal*, *31*(1), 13–24. <http://doi.org/10.1080/02626668609491024>
- Kljun, N., Calanca, P., Rotach, M. W., & Schmid, H. P. (2004). A simple parameterisation for flux footprint predictions. *Boundary-Layer Meteorology*, *112*, 503–523. <http://doi.org/10.1023/B:BOUN.0000030653.71031.96>
- Kljun, N., Rotach, M. W., & Schmid, H. P. (2002). A Three-Dimensional Backward Lagrangian Footprint Model For A Wide Range Of Boundary-Layer Stratifications.

- Boundary-Layer Meteorology*, 103(2), 205–226.
<http://doi.org/10.1023/A:1014556300021>
- Koehler, A. (1933). A new hypothesis as to the cause of shakes and rift cracks in green timber. *Journal of Forestry*, 31(5), 551–556.
- Körner, C. (1994). *Ecophysiology of Photosynthesis*. (E.-D. Schulze & M. M. Caldwell, Eds.). Berlin, Heidelberg: Springer Berlin Heidelberg. <http://doi.org/10.1007/978-3-642-79354-7>
- Körner, C. (1995). Leaf Diffusive Conductances in the Major Vegetation Types of the Globe. In E.-D. Schulze & M. Caldwell (Eds.), *Ecophysiology of Photosynthesis SE - 22* (Vol. 100, pp. 463–490). Springer Berlin Heidelberg.
http://doi.org/10.1007/978-3-642-79354-7_22
- Kucharik, C. J., Barford, C. C., Maayar, M. El, Wofsy, S. C., Monson, R. K., & Baldocchi, D. D. (2006). A multiyear evaluation of a Dynamic Global Vegetation Model at three AmeriFlux forest sites: Vegetation structure, phenology, soil temperature, and CO₂ and H₂O vapor exchange. *Ecological Modelling*, 196(1-2), 1–31. <http://doi.org/10.1016/j.ecolmodel.2005.11.031>
- Kulkarni, M. V., Groffman, P. M., Yavitt, J. B., & Goodale, C. L. (2014). Complex controls of denitrification at ecosystem, landscape and regional scales in northern hardwood forests. *Ecological Modelling*, 298, 39–52.
<http://doi.org/10.1016/j.ecolmodel.2014.03.010>
- LeBauer, D. S., & Treseder, K. K. (2008). Nitrogen limitation of net primary productivity in terrestrial ecosystems is globally disturbed. *Ecology*, 89(2), 371–379.
<http://doi.org/10.1890/06-2057.1>
- Lévesque, J., & King, D. J. (1999). Airborne digital camera image semivariance for evaluation of forest structural damage at an acid mine site. *Remote Sensing of Environment*, 68(December 1997), 112–124. [http://doi.org/10.1016/S0034-4257\(98\)00104-7](http://doi.org/10.1016/S0034-4257(98)00104-7)
- Lindroth, a., & Cienciala, E. (1995). Measuring water use efficiency of Eucalypt tress with chambers and micrometeorological techniques — comment. *Journal of Hydrology*, 169(1-4), 281–283. [http://doi.org/10.1016/0022-1694\(94\)02665-X](http://doi.org/10.1016/0022-1694(94)02665-X)
- Livneh, B., Deems, J. S., Buma, B., Barsugli, J. J., Schneider, D., Molotch, N. P., ... Wessman, C. a. (2015). Catchment response to bark beetle outbreak and dust-on-snow in the Colorado Rocky Mountains. *Journal of Hydrology*, 523, 196–210.
<http://doi.org/10.1016/j.jhydrol.2015.01.039>

- Lloyd, C. R. (1995). The effect of heterogeneous terrain on micrometeorological flux measurements: a case study from HAPEX-Sahel. *Agricultural and Forest Meteorology*, 73(3-4), 209–216. [http://doi.org/10.1016/0168-1923\(94\)05075-H](http://doi.org/10.1016/0168-1923(94)05075-H)
- Lloyd, J., & Taylor, J. A. (1994). On the Temperature Dependence of Soil Respiration. *Functional Ecology*, 8(3), 315. <http://doi.org/10.2307/2389824>
- Loescher, H. W., Gholz, H. L., Jacobs, J. M., & Oberbauer, S. F. (2005). Energy dynamics and modeled evapotranspiration from a wet tropical forest in Costa Rica. *Journal of Hydrology*, 315(1-4), 274–294. <http://doi.org/10.1016/j.jhydrol.2005.03.040>
- Mackay, D. S. (2001). Evaluation of hydrologic equilibrium in a mountainous watershed: incorporating forest canopy spatial adjustment to soil biogeochemical processes. *Advances in Water Resources*, 24(9), 1211–1227. [http://doi.org/doi:10.1016/S0309-1708\(01\)00040-9](http://doi.org/doi:10.1016/S0309-1708(01)00040-9)
- Mackay, D. S., & Band, L. E. (1997). Forest ecosystem processes at the watershed scale: dynamic coupling of distributed hydrology and canopy growth. *Hydrological Processes*, 11(9), 1197–1217. [http://doi.org/10.1002/\(SICI\)1099-1085\(199707\)11:9<1197::AID-HYP552>3.0.CO;2-W](http://doi.org/10.1002/(SICI)1099-1085(199707)11:9<1197::AID-HYP552>3.0.CO;2-W)
- Masek, J. G., Vermote, E. F., Saleous, N. E., Wolfe, R., Hall, F. G., Huemmrich, K. F., ... Lim, T. (2006). A Landsat Surface Reflectance Dataset. *IEEE Geoscience and Remote Sensing Letters*, 3(1), 68–72. <http://doi.org/10.1109/LGRS.2005.857030>
- Matheron, G. (1963). Principles of geostatistics. *Economic Geology*, 58(8), 1246–1266. <http://doi.org/10.2113/gsecongeo.58.8.1246>
- McClure, M. S. (1991). Density-dependent feedback and population cycles in *Adelges tsugae* (Homoptera: Adelgidae) on *Tsuga canadensis*. *Environmental Entomology*, 20(1), 258–264. <http://doi.org/10.1093/ee/20.1.258>
- McDowell, N. G., Fisher, R. a., Xu, C., Domec, J. C., Hölttä, T., Mackay, D. S., ... Pockman, W. T. (2013). Evaluating theories of drought-induced vegetation mortality using a multimodel-experiment framework. *New Phytologist*, 200(2), 304–321. <http://doi.org/10.1111/nph.12465>
- McManus, K. A., Shields, K. S., & Souto, D. R. (1999). Proceedings: Symposium on Sustainable Management of Hemlock Ecosystems in Eastern North America. United States Forest Service General Technical Report NE-267.

- McNaughton, K. G., & Jarvis, P. G. (1983). *Predicting effects of vegetation changes on transpiration and evaporation in [Water deficits and plant growth]*. (T. T. Kozlowski, Ed.). London: Academic Press.
- Medvigy, D., Wofsy, S. C., Munger, J. W., Hollinger, D. Y., & Moorcroft, P. R. (2009). Mechanistic scaling of ecosystem function and dynamics in space and time: Ecosystem Demography model version 2. *Journal of Geophysical Research: Biogeosciences*, *114*, G01002. <http://doi.org/10.1029/2008JG000812>
- Meentemeyer, R. K., & Moody, A. (2002). Distribution of Plant Life History Types in California Chaparral: The Role of Topographically-Determined Drought Severity. *Journal of Vegetation Science*, *13*(1), 67–78. <http://doi.org/10.2307/3236654>
- Menzel, A., Sparks, T. H., Estrella, N., Koch, E., Aaasa, A., Ahas, R., ... Zust, A. (2006). European phenological response to climate change matches the warming pattern. *Global Change Biology*, *12*(10), 1969–1976. <http://doi.org/10.1111/j.1365-2486.2006.01193.x>
- Mikkelsen, K. M., Bearup, L. a., Maxwell, R. M., Stednick, J. D., McCray, J. E., & Sharp, J. O. (2013). Bark beetle infestation impacts on nutrient cycling, water quality and interdependent hydrological effects. *Biogeochemistry*, *115*(1-3), 1–21. <http://doi.org/10.1007/s10533-013-9875-8>
- Mikkelsen, K. M., Maxwell, R. M., Ferguson, I., Stednick, J. D., Mccray, J. E., & Sharp, J. O. (2013). Mountain pine beetle infestation impacts: Modeling water and energy budgets at the hill-slope scale. *Ecohydrology*, *6*(1), 64–72. <http://doi.org/10.1002/eco.278>
- Mittman, T., Band, L. E., Hwang, T., & Smith, M. L. (2012). Distributed Hydrologic Modeling in the Suburban Landscape: Assessing Parameter Transferability from Gauged Reference Catchments. *Journal of the American Water Resources Association*, *48*(3), 546–557. <http://doi.org/10.1111/j.1752-1688.2011.00636.x>
- Monserud, R. A., & Sterba, H. (1999). Modeling individual tree mortality for Austrian forest species. *Forest Ecology and Management*, *113*(2-3), 109–123. [http://doi.org/10.1016/S0378-1127\(98\)00419-8](http://doi.org/10.1016/S0378-1127(98)00419-8)
- Munger, J. W., & Wofsy, S. C. (1999). Canopy-Atmosphere Exchange of Carbon, Water and Energy at Harvard Forest EMS Tower since 1991. Harvard Forest Data Archive: HF004. Retrieved from <http://harvardforest.fas.harvard.edu:8080/exist/xquery/data.xq?id=hf004>

- Munger, W. J., & Wofsy, S. C. (1999). Biomass Inventories at Harvard Forest EMS Tower since 1993. Harvard Forest Data Archive: HF069. Retrieved October 16, 2014, from <http://harvardforest.fas.harvard.edu:8080/exist/xquery/data.xq?id=hf069>
- Nemani, R. R., Keeling, C. D., Hashimoto, H., Jolly, W. M., Piper, S. C., Tucker, C. J., ... Running, S. W. (2003). Climate-driven increases in global terrestrial net primary production from 1982 to 1999. *Science (New York, N.Y.)*, *300*(5625), 1560–1563. <http://doi.org/10.1126/science.1082750>
- Nemani, R. R., Pierce, L., Running, S. W., & Band, L. E. (1993). Forest ecosystem processes at the watershed scale: sensitivity to remotely-sensed Leaf Area Index estimates. *International Journal of Remote Sensing*, *14*(13), 2519–2534. <http://doi.org/10.1080/01431169308904290>
- Nemani, R. R., & Running, S. W. (1989). Testing a theoretical climate-soil-leaf area hydrologic equilibrium of forests using satellite data and ecosystem simulation. *Agricultural and Forest Meteorology*, *44*(3-4), 245–260. [http://doi.org/10.1016/0168-1923\(89\)90020-8](http://doi.org/10.1016/0168-1923(89)90020-8)
- NOAA. (2013). CO₂ at NOAA's Mauna Loa Observatory reaches new milestone: Tops 400 ppm. Retrieved from <http://www.esrl.noaa.gov/gmd/news/7074.html>
- Norby, R. J., & Jackson, R. B. (2000). Root dynamics and global change: seeking an ecosystem perspective. *New Phytologist*, *147*(1), 3–12. <http://doi.org/10.1046/j.1469-8137.2000.00676.x>
- Noréus, J. P., Nyborg, M. R., & Hayling, K. L. (1997). The gravity anomaly field in the Gulf of Bothnia spatially characterized from satellite altimetry and in situ measurements. *Journal of Applied Geophysics*, *37*(2), 67–84. [http://doi.org/10.1016/S0926-9851\(97\)00007-4](http://doi.org/10.1016/S0926-9851(97)00007-4)
- Novick, K. A., Brantley, S. T., Miniati, C. F., Walker, J., & Vose, J. M. (2014). Inferring the contribution of advection to total ecosystem scalar fluxes over a tall forest in complex terrain. *Agricultural and Forest Meteorology*, *185*, 1–13. <http://doi.org/10.1016/j.agrformet.2013.10.010>
- NRCS. (2009). Soil Survey Geographic (SSURGO) Database. USDA NRCS [National Resources Conservation Service]. Available online at <http://sdmdataaccess.nrcs.usda.gov/>. Accessed Mar/30/2012.
- O'Keefe, J. (2000). Phenology of Woody Species at Harvard Forest since 1990. Harvard Forest Data Archive: HF003. Retrieved October 17, 2014, from <http://harvardforest.fas.harvard.edu:8080/exist/xquery/data.xq?id=hf003>

- Oishi, C. A., Oren, R., Novick, K. A., Palmroth, S., & Katul, G. G. (2010). Interannual Invariability of Forest Evapotranspiration and Its Consequence to Water Flow Downstream. *Ecosystems*, 13(3), 421–436. <http://doi.org/10.1007/s10021-010-9328-3>
- Orwig, D. A., Cobb, R. C., D'Amato, A. W., Kizlinski, M. L., & Foster, D. R. (2008). Multi-year ecosystem response to hemlock woolly adelgid infestation in southern New England forests. *Canadian Journal of Forest Research*, 38(4), 834–843. <http://doi.org/10.1139/X07-196>
- Orwig, D. A., & Foster, D. (1998). Forest response to the introduced hemlock woolly adelgid in southern New England, USA. *Journal of the Torrey Botanical Society*, 125(1), 60–73. <http://doi.org/10.2307/2997232>
- Orwig, D. a., Foster, D. R., & Mausel, D. L. (2002). Landscape patterns of hemlock decline in New England due to the introduced hemlock woolly adelgid. *Journal of Biogeography*, 29(10-11), 1475–1487. <http://doi.org/10.1046/j.1365-2699.2002.00765.x>
- Orwig, D. A., & Povak, N. (2004). Landscape-level analyses of Hemlock Woolly Adelgid in Massachusetts. In *the 15th Annual Harvard Forest Ecology Symposium* (p. 98).
- Parton, W. J., Mosier, A. R., Ojima, D. S., Valentine, D. W., Schimel, D. S., Weier, K., & Kulmala, A. E. (1996). Generalized model for N₂ and N₂O production from nitrification and denitrification. *Global Biogeochemical Cycles*, 10(3), 401–412. <http://doi.org/10.1029/96GB01455>
- Parton, W. J., Scurlock, J. M. O., Ojima, D. S., Gilmanov, T. G., Scholes, R. J., Schimel, D. S., ... Kinyamario, J. I. (1993). Observations and modeling of biomass and soil organic matter dynamics for the grassland biome worldwide. *Global Biogeochemical Cycles*, 7(4), 785–809. <http://doi.org/10.1029/93GB02042>
- Pasquill, F. (1974). *Atmospheric diffusion: the dispersion of windborne material from industrial and other sources* (2nd ed.). New York: Wiley.
- Pontius, J., Hallett, R., & Martin, M. (2005a). Assessing hemlock decline using visible and near-infrared spectroscopy: Indices comparison and algorithm development. *Applied Spectroscopy*, 59(6), 836–843. <http://doi.org/10.1366/0003702054280595>
- Pontius, J., Hallett, R., & Martin, M. (2005b). Using AVIRIS to assess hemlock abundance and early decline in the Catskills, New York. *Remote Sensing of Environment*, 97(2), 163–173. <http://doi.org/10.1016/j.rse.2005.04.011>

- Raich, J. W., & Tufekciogul, A. (n.d.). Vegetation and soil respiration: Correlations and controls. *Biogeochemistry*, 48(1), 71–90. <http://doi.org/10.1023/A:1006112000616>
- Richardson, A. D., Hollinger, D. Y., Aber, J. D., Ollinger, S. V., & Braswell, B. H. (2007). Environmental variation is directly responsible for short- but not long-term variation in forest-atmosphere carbon exchange. *Global Change Biology*, 13(4), 788–803. <http://doi.org/10.1111/j.1365-2486.2007.01330.x>
- Román, M. O., Schaaf, C. B., Woodcock, C. E., Strahler, A. H., Yang, X., Braswell, R. H., ... Goulden, M. L. (2009). The MODIS (Collection V005) BRDF/albedo product: Assessment of spatial representativeness over forested landscapes. *Remote Sensing of Environment*, 113(11), 2476–2498. <http://doi.org/10.1016/j.rse.2009.07.009>
- Royer, P. D., Breshears, D. D., Zou, C. B., Cobb, N. S., & Kurc, S. a. (2010). Ecohydrological energy inputs in semiarid coniferous gradients: Responses to management- and drought-induced tree reductions. *Forest Ecology and Management*, 260(10), 1646–1655. <http://doi.org/10.1016/j.foreco.2010.07.036>
- Royer, P. D., Cobb, N. S., Clifford, M. J., Huang, C. Y., Breshears, D. D., Adams, H. D., & Villegas, J. C. (2011). Extreme climatic event-triggered overstorey vegetation loss increases understorey solar input regionally: Primary and secondary ecological implications. *Journal of Ecology*, 99(3), 714–723. <http://doi.org/10.1111/j.1365-2745.2011.01804.x>
- Running, S. W., & Hunt Jr., E. R. (1993). Generalization of a Forest Ecosystem Process Model for Other Biomes, BIOME-BCG, and an Application for Global-Scale Models. In *Academic Press, Inc.* (pp. 141–158). Retrieved from <http://secure.nts.g.umt.edu/publications/1993/RH93/>
- Running, S. W., Nemani, R. R., & Hungerford, R. D. (1987). Extrapolation of synoptic meteorological data in mountainous terrain and its use for simulating forest evapotranspiration and photosynthesis. *Canadian Journal of Forest Research*, 17(6), 472–483. <http://doi.org/10.1139/x87-081>
- Ryan, M. G., Binkley, D., & Fownes, J. H. (1997). Age-Related Decline in Forest Productivity: Pattern and Process. In *Adv. Ecol. Res.* (Vol. 27, pp. 213–262). [http://doi.org/10.1016/S0065-2504\(08\)60009-4](http://doi.org/10.1016/S0065-2504(08)60009-4)
- Savage, K. E., & Davidson, E. A. (2001). Interannual variation of soil respiration in two New England forests. *Global Biogeochemical Cycles*, 15(2), 337–350. <http://doi.org/10.1029/1999GB001248>

- Schimel, D. S., House, J. I., Hibbard, K. a, Bousquet, P., Ciais, P., Peylin, P., ... Wirth, C. (2001). Recent patterns and mechanisms of carbon exchange by terrestrial ecosystems. *Nature*, *414*(6860), 169–172. <http://doi.org/10.1038/35102500>
- Schlesinger, W. H., & Andrews, J. A. (2000). Soil respiration and the global carbon cycle. *Biogeochemistry*, *48*(1), 7–20. <http://doi.org/10.1023/A:1006247623877>
- Schmid, H. P. (1994). Source areas for scalars and scalar fluxes. *Boundary-Layer Meteorology*, *67*, 293–318. <http://doi.org/10.1007/BF00713146>
- Schwalm, C. R., Williams, C. a., Schaefer, K., Anderson, R. S., Arain, M. A., Baker, I., ... Verma, S. B. (2010). A model-data intercomparison of CO₂ exchange across North America: Results from the North American Carbon Program site synthesis. *Journal of Geophysical Research: Biogeosciences*, *115*(4). <http://doi.org/10.1029/2009JG001229>
- Sheil, D., Burslem, D. F. R. P., & Alder, D. (1995). The Interpretation and misinterpretation of mortality rate measures. *Journal of Ecology*, *83*(2), 331–333. <http://doi.org/10.2307/2261571>
- Shields, C. A., & Tague, C. L. (2012). Assessing the Role of Parameter and Input Uncertainty in Ecohydrologic Modeling: Implications for a Semi-arid and Urbanizing Coastal California Catchment. *Ecosystems*, *15*(5), 775–791. <http://doi.org/10.1007/s10021-012-9545-z>
- Shigo, A. L. (1963). Ring shake associated with Sapsucker injury. *U. S. Department of Agriculture, Forest Service Research Paper NE-8*.
- Somers, G. L., Oderwald, R. G., Harms, W. R., & Langdon, O. G. (1980). Predicting Mortality with a Weibull Distribution. *Forest Science*, *26*(2), 291–300.
- Sperry, J. S., Adler, F. R., Campbell, G. S., & Comstock, J. P. (1998). Limitation of plant water use by rhizosphere and xylem conductance: results from a model. *Plant, Cell and Environment*, *21*(4), 347–359. <http://doi.org/10.1046/j.1365-3040.1998.00287.x>
- Stadler, B., Müller, T., Orwig, D. A., & Cobb, R. (2005). Hemlock woolly adelgid in New England forests: Canopy impacts transforming ecosystem processes and landscapes. *Ecosystems*, *8*(3), 233–247. <http://doi.org/10.1007/s10021-003-0092-5>
- Stephenson, N. L., Das, A. J., Condit, R., Russo, S. E., Baker, P. J., Beckman, N. G., ... Zavala, M. A. (2014). Rate of tree carbon accumulation increases continuously with tree size. *Nature*, *507*(7490), 90–3. <http://doi.org/10.1038/nature12914>

- Stoy, P. C., Katul, G. G., Siqueira, M. B. S., Juang, J. Y., Novick, K. A., Uebelherr, J. M., & Oren, R. (2006). An evaluation of models for partitioning eddy covariance-measured net ecosystem exchange into photosynthesis and respiration. *Agricultural and Forest Meteorology*, *141*(1), 2–18. <http://doi.org/10.1016/j.agrformet.2006.09.001>
- Stoy, P. C., Katul, G. G., Siqueira, M. B. S., Juang, J.-Y., Novick, K. A., McCarthy, H. R., ... Oren, R. (2006). Separating the effects of climate and vegetation on evapotranspiration along a successional chronosequence in the southeastern US. *Global Change Biology*, *12*(11), 2115–2135. <http://doi.org/10.1111/j.1365-2486.2006.01244.x>
- Stoyan, H., De-Polli, H., Böhm, S., Robertson, G. P., & Paul, E. A. (2000). Spatial heterogeneity of soil respiration and related properties at the plant scale. *Plant and Soil*, *222*, 203–214. <http://doi.org/10.1023/A:1004757405147>
- Susaki, J., Yasuoka, Y., Kajiwar, K., Honda, Y., & Hara, K. (2007). Validation of MODIS albedo products of paddy fields in Japan. *IEEE Transactions on Geoscience and Remote Sensing*, *45*(1), 206–217. <http://doi.org/10.1109/TGRS.2006.882266>
- Tague, C. L., & Band, L. E. (2004). RHESSys: Regional Hydro-Ecologic Simulation System—An Object-Oriented Approach to Spatially Distributed Modeling of Carbon, Water, and Nutrient Cycling. *Earth Interactions*, *8*(19), 1–42. Retrieved from [http://dx.doi.org/10.1175/1087-3562\(2004\)8<1:RRHSSO>2.0.CO;2](http://dx.doi.org/10.1175/1087-3562(2004)8<1:RRHSSO>2.0.CO;2)
- Tague, C. L., Heyn, K., & Christensen, L. (2009). Topographic controls on spatial patterns of conifer transpiration and net primary productivity under climate warming in mountain ecosystems. *Ecohydrology*, *2*(4), 541–554. <http://doi.org/10.1002/eco>
- Tague, C. L., McDowell, N. G., & Allen, C. D. (2013). An integrated model of environmental effects on growth, carbohydrate balance, and mortality of *Pinus ponderosa* forests in the southern Rocky Mountains. *PLoS ONE*, *8*(11). <http://doi.org/10.1371/journal.pone.0080286>
- Tague, C. L., & Pohl-Costello, M. (2008). The Potential Utility of Physically Based Hydrologic Modeling in Ungauged Urban Streams. *Annals of the Association of American Geographers*, *98*(4), 818–833. <http://doi.org/10.1080/00045600802099055>
- Tague, C. L., Seaby, L., & Hope, A. (2009). Modeling the eco-hydrologic response of a Mediterranean type ecosystem to the combined impacts of projected climate change and altered fire frequencies. *Climatic Change*, *93*(1-2), 137–155. <http://doi.org/10.1007/s10584-008-9497-7>

- Tang, X., Wang, Z., Liu, D., Song, K., Jia, M., Dong, Z., ... Liu, X. (2012). Estimating the net ecosystem exchange for the major forests in the northern United States by integrating MODIS and AmeriFlux data. *Agricultural and Forest Meteorology*, 156, 75–84. <http://doi.org/10.1016/j.agrformet.2012.01.003>
- Temesgen, H., & Mitchell, S. J. (2005). An individual-tree mortality model for complex stands of southeastern British Columbia. *Western Journal of Applied Forestry*, 20(2), 101–109.
- The MathWorks, I. (2000). MATLAB 8.1 and Statistics Toolbox 8.1. Natick, MA.
- Tian, Y., Woodcock, C., Wang, Y., Privette, J., Shabanov, N., Zhou, L., ... Veikkanen, B. (2002). Multiscale analysis and validation of the MODIS LAI productII. Sampling strategy. *Remote Sensing of Environment*, 83, 431–441. [http://doi.org/10.1016/S0034-4257\(02\)00058-5](http://doi.org/10.1016/S0034-4257(02)00058-5)
- Urbanski, S., Barford, C. C., Wofsy, S. C., Kucharik, C. J., Pyle, E., Budney, J., ... Munger, J. W. (2007). Factors controlling CO₂ exchange on timescales from hourly to decadal at Harvard Forest. *Journal of Geophysical Research*, 112(G2), G02020. <http://doi.org/10.1029/2006JG000293>
- Van Ulden, A. P. (1978). Simple estimates for vertical diffusion from sources near the ground. *Atmospheric Environment (1967)*, 12(11), 2125–2129. [http://doi.org/10.1016/0004-6981\(78\)90167-1](http://doi.org/10.1016/0004-6981(78)90167-1)
- Vicente-Serrano, S. M., Camarero, J. J., Zabalza, J., Sangüesa-Barreda, G., López-Moreno, J. I., & Tague, C. L. (2015). Evapotranspiration deficit controls net primary production and growth of silver fir: Implications for Circum-Mediterranean forests under forecasted warmer and drier conditions. *Agricultural and Forest Meteorology*, 206, 45–54. <http://doi.org/10.1016/j.agrformet.2015.02.017>
- Vose, J. M., Sun, G., Ford, C. R., Bredemeier, M., Otsuki, K., Wei, X., ... Zhang, L. (2011). Forest ecohydrological research in the 21st century: What are the critical needs? *Ecohydrology*, 4(2), 146–158. <http://doi.org/10.1002/eco.193>
- Walsh, J., Wuebbles, D., Hayhoe, K., Kossin, J., Kunkel, K., Stephens, G., ... Somerville, R. (2014). Chapter 2: our changing climate. In *Climate Change Impacts in the United States: The Third National Climate Assessment* (pp. 19–67). <http://doi.org/10.7930/J0KW5CXT>
- Walther, G.-R., Beißner, S., & Burga, C. a. (2005). Trends in the upward shift of alpine plants. *Journal of Vegetation Science*, 16(5), 541–548. <http://doi.org/10.1111/j.1654-1103.2005.tb02394.x>

- Waring, R. H., Law, B. E., Goulden, M. L., Bassow, S. L., McCreight, R. W., Wofsy, S. C., & Bazzaz, F. A. (1995). Scaling gross ecosystem production at Harvard Forest with remote sensing: a comparison of estimates from a constrained quantum-use efficiency model and eddy correlation. *Plant, Cell & Environment*, *18*(10), 1201–1213. <http://doi.org/10.1111/j.1365-3040.1995.tb00629.x>
- Webster, J. R., Morkeski, K., Wojculewski, C. A., Niederlehner, B. R., Benfield, E. F., & Elliott, K. J. (2012). Effects of hemlock mortality on streams in the Southern Appalachian Mountains. *The American Midland Naturalist*, *168*(1), 112–131. <http://doi.org/10.1674/0003-0031-168.1.112>
- Welp, L. R., Randerson, J. T., & Liu, H. P. (2007). The sensitivity of carbon fluxes to spring warming and summer drought depends on plant functional type in boreal forest ecosystems. *Agricultural and Forest Meteorology*, *147*(3-4), 172–185. <http://doi.org/10.1016/j.agrformet.2007.07.010>
- White, M. A., Thornton, P. E., Running, S. W., & Nemani, R. R. (2000). Parameterization and Sensitivity Analysis of the BIOME–BGC Terrestrial Ecosystem Model: Net Primary Production Controls. *Earth Interactions*, *4*(3), 1–85. [http://doi.org/10.1175/1087-3562\(2000\)004<0003:PASAOT>2.0.CO;2](http://doi.org/10.1175/1087-3562(2000)004<0003:PASAOT>2.0.CO;2)
- Wickham, J. D., Stehman, S. V., Fry, J. a., Smith, J. H., & Homer, C. G. (2010). Thematic accuracy of the NLCD 2001 land cover for the conterminous United States. *Remote Sensing of Environment*, *114*(6), 1286–1296. <http://doi.org/10.1016/j.rse.2010.01.018>
- Wickham, J. D., Stehman, S. V., Gass, L., Dewitz, J., Fry, J. A., & Wade, T. G. (2013). Accuracy assessment of NLCD 2006 land cover and impervious surface. *Remote Sensing of Environment*, *130*(0), 294–304. <http://doi.org/http://dx.doi.org/10.1016/j.rse.2012.12.001>
- Wigmosta, M. S., Vail, L. W., & Lettenmaier, D. P. (1994). A distributed hydrology-vegetation model for complex terrain. *Water Resources Research*, *30*(6), 1665–1679. <http://doi.org/10.1029/94WR00436>
- Wu, Z. Y., Zhang, L., Wang, X. M., & Munger, J. W. (2015). A modified micrometeorological gradient method for estimating O₃ dry deposition over a forest canopy. *Atmospheric Chemistry and Physics Discussions*, *15*(1), 779–806. <http://doi.org/10.5194/acpd-15-779-2015>
- Wythers, K. R., Reich, P. B., & Bradford, J. B. (2013). Incorporating temperature-sensitive Q₁₀ and foliar respiration acclimation algorithms modifies modeled ecosystem responses to global change. *Journal of Geophysical Research: Biogeosciences*, *118*(1), 77–90. <http://doi.org/10.1029/2011JG001897>

- Xiao, X., Zhang, Q., Braswell, B. H., Urbanski, S., Boles, S., Wofsy, S., ... Ojima, D. (2004). Modeling gross primary production of temperate deciduous broadleaf forest using satellite images and climate data. *Remote Sensing of Environment*, 91(2), 256–270. <http://doi.org/10.1016/j.rse.2004.03.010>
- Xu, N., & Saiers, J. E. (2010). Temperature and Hydrologic Controls on Dissolved Organic Matter Mobilization and Transport within a Forest Topsoil. *Environmental Science & Technology*, 44(14), 5423–5429. <http://doi.org/10.1021/es1002296>
- Xu, N., Saiers, J. E., Wilson, H. F., & Raymond, P. A. (2012). Simulating streamflow and dissolved organic matter export from a forested watershed. *Water Resources Research*, 48(5), W05519. <http://doi.org/10.1029/2011WR011423>
- Yang, D., Goodison, B. E., Ishida, S., & Benson, C. S. (1998). Adjustment of daily precipitation data at 10 climate stations in Alaska: Application of World Meteorological Organization intercomparison results. *Water Resources Research*, 34(2), 241–256. <http://doi.org/10.1029/97WR02681>
- Zhang, X., Friedl, M. A., Schaaf, C. B., Strahler, A. H., Hodges, J. C. F., Gao, F., ... Huete, A. R. (2003). Monitoring vegetation phenology using MODIS. *Remote Sensing of Environment*, 84(3), 471–475. [http://doi.org/http://dx.doi.org/10.1016/S0034-4257\(02\)00135-9](http://doi.org/http://dx.doi.org/10.1016/S0034-4257(02)00135-9)
- Zhao, M., & Running, S. W. (2010). Drought-Induced Reduction in Global. *Science*, 329(5994), 940–943. <http://doi.org/10.1126/science.1192666>

CURRICULUM VITAE

